APPLIED PHYSICS

4` 25



Applied Physics 2025, No. 4

The journal was founded in 1994

The scientific and technical peer-reviewed journal is intended for the publication of articles on the latest achievements in the field of physics with prospects for advancements (technical and scientific) applications.

The periodicity is 6 issues per year.

Founder and publisher

Research, Development and Production Center ORION, Joint-Stock Company – Russian Federation State Science Center

(RD&P Center ORION, JSC) 9, Kosinskaya st., Moscow, 111538 Russia

The journal is included into the List of peer-reviewed science press of the State Commission for Academic Degrees and Titles of Russian Federation. The Journal is included in Scientific Electronic Library eLIBRARY.RU, SCOPUS, Chemical Abstracts (CA), Russian Science Citation Index (RSCI), Directory of Open Access Journals (DOAJ), Directory of Open Access Scholarly Resources (ROAD), Google Scholar.

Editor-in-Chief

Igor Burlakov,

Dr. Sci. (Eng.), Professor,
Research, Development and Production Center ORION, Joint-Stock Company –
Russian Federation State Science Center

Editorial office address

9, Kosinskaya st., Moscow, 111538, Russia, RD&P Center ORION, JSC.
Phone: 8(499) 374-82-40
E-mail: advance@orion-ir.ru
Internet: applphys.orion-ir.ru

The registration PI No. FS 77-73641
was issued in September 21, 2018
by the Federal Service for Supervision
of Communications, Information Technology, and Mass Media of Russia

Editorial Board

Andreev Stepan Dr. Sci. (Phys.-Math.), Prokhorov General Physics Institute of the

Russian Academy of Sciences, Moscow, Russia

Boltar Konstantin Dr. Sci. (Phys.-Math.), Professor, RD&P Center ORION, JSC, Moscow,

Russia

Gusein-zade Namik Dr. Sci. (Phys.-Math.), Professor, Prokhorov General Physics Institute of

the Russian Academy of Sciences, Moscow, Russia

Ivanov Victor Dr. Sci. (Phys.-Math.), Professor, Corresponding Member of the Russian

Academy of Sciences, Moscow Institute of Physics and Technology,

Dolgoprudny, Moscow Region, Russian

Ivanov Vyacheslav PhD (Phys.-Math.), Associate Professor, Prokhorov General Physics

Institute of the Russian Academy of Sciences, Moscow, Russia

Kholodnov Vyacheslav Dr. Sci. (Phys.-Math.), Professor, Kotelnikov Institute of

RadioEngineering and Electronics of Russian Academy of Sciences,

Moscow, Russia

Khomich Vladislav Dr. Sci. (Phys.-Math.), Academician of the Russian Academy of

Sciences, Branch of Federal State Budgetary Scientific Institution for Electrophysics and Electric Power of Russian Academy of Sciences,

Moscow, Russia

Klimanov Evgeniy Dr. Sci. (Eng.), Professor, RD&P Center ORION, JSC, Moscow, Russia

Konov Vitaly Dr. Sci. (Phys.-Math.), Academician of the Russian Academy of

Sciences, Prokhorov General Physics Institute of the Russian Academy

of Sciences, Moscow, Russia

Lebedev Yuri Dr. Sci. (Phys.-Math.), A. V. Topchiev Institute of Petrochemical

Synthesis of the Russian Academy of Sciences, Moscow, Russia

Lyamshev Michael PhD (Phys.-Math.), Prokhorov General Physics Institute of the Russian

Academy of Sciences, Moscow, Russia

Mayorov Sergei Dr. Sci. (Phys.-Math.), Joint Institute for High Temperatures of Russian

Academy of Sciences, Moscow, Russia

Nikitov Sergei Dr. Sci. (Phys.-Math.), Professor, Academician of the Russian Academy

of Sciences, Kotelnikov Institute of RadioEngineering and Electronics of

Russian Academy of Sciences, Moscow, Russia

Ponomarenko Vladimir Dr. Sci. (Phys.-Math.), Professor, RD&P Center ORION, JSC, Moscow,

Russia

Popov Sergev Dr. Sci. (Eng.), Shyabe Holding, Moscow, Russia

Vasilyak Leonid Dr. Sci. (Phys.-Math.), Professor (Deputy Editor-in-Chief), Joint

Institute for High Temperatures of Russian Academy of Sciences,

Moscow, Russia

Yakovleva Natalia Dr. Sci. (Eng.), RD&P Center ORION, JSC, Moscow, Russia

Yamshchikov Vladimir Dr. Sci. (Eng.), Corresponding Member of the Russian Academy of

Sciences, Branch of Federal State Budgetary Scientific Institution for Electrophysics and Electric Power of Russian Academy of Sciences,

Moscow, Russia

APPLIED PHYSICS [in Russian]

THE SCIENTIFIC AND TECHNICAL JOURNAL

2025, No. 4	Founded in 1994	Moscow
	CONTENTS	
	GENERAL PHYSICS	
Calculation of the spectral of Sviridov A. N., Saginov L. D.	lensity of radiation for black (gray) bodies and subvand Khafizov R. Z.	wavelength particles 5
	PHOTOELECTRONICS	
_	ess control method for optical elements o. N. A., Zaripov Sh. I. and Mashoshin D. A.	16
ZnO/CH ₃ NH ₃ PbI ₃ /NiO pero	the rate of generation and recombination of ovskite solar cell designs N., Agoev A. Z., Molokanov O. A. and Karmokova R. Y	
	PLASMA PHYSICS AND PLASMA METHODS	
Electric field strength meas Panov V. A., Saveliev A. S. ar	urements in transformer oil using microdroplets of ad Kulikov Yu. M.	water 30
Accumulation of ions in an electric discharge Polyakov D. N., Shumova V.	electrostatic plasma trap within a cloud of charged V. and Vasilyak L. M.	microparticles in an
Influence of electrolyte ten discharge with a liquid cath Tazmeev G. K. and Tazmeev		pulsations in a gas
	e positive column of a glow discharge at low pressur ., Dzlieva E. S. and Karasev V. Yu.	re of an inert gas
	PHYSICAL SCIENCE OF MATERIALS	
Metrological support of dig	cital measurements of images of etch pit inhomogen	neity in GaAs single
<u> </u>	zev S. N., Sokolovskaya E. A., Kudrya A. V., va E. V.	Sukhanova A. S., 59
_	rosion and biofouling of stainless steel samples in a t E. A., Vasilyak L. M. and Fialkina C. V.	tropical climate 68

74
81
87
94
101
107
_

INFORMATION

Rules for authors 119

GENERAL PHYSICS :

UDC 536.3 PACS: 44.40.+a, 42.68Ay, 42.72.g

EDN: AGJQQE

Calculation of the spectral density of radiation for black (gray) bodies and subwavelength particles

© A. N. Sviridov^{1,*}, L. D. Saginov¹ and R. Z. Khafizov²

¹ FSAC VIM, Moscow, 109428 Russia * E-mail: sviridtoly@yandex.ru ² ODB «ASTROHN» JSC, Lytkarino, Moscow Region, 140080 Russia

Received 25.04.2025; revised 20.05.2025; accepted 11.08.2025 Scientific specialty code: 1.3.14

A new method for calculating the spectral radiation powers of subwavelength particles is proposed, in which calculations are performed using the dependence of the quality factor of electric small radio antennas (ESA) on their relative (relative to the wavelength of the emitted wave) dimensions. A formula is obtained for calculating the spectral radiation density of black (gray) bodies and subwavelength particles, as well as a ratio for calculating the power emitted in one spatially-spectral mode of black (gray) bodies and subwavelength particles. New versions of the Planck and Stefan-Boltzmann spectral dependences are presented.

Keywords: Planck's law; spatial-spectral mode; subwavelength particle; electrically small antenna (ESA); Normal mode; Radian sphere; Radian mode; Radian Emitter; Q-factor; near field; far field.

DOI: 10.51368/1996-0948-2025-4-5-15

Introduction

It is known [1–8] that the Planck's law and Stefan-Boltzmann law, which describe the body heat well, cannot be applied in cases when the body size becomes smaller than λ_{max}^{-1} . Such bodies (hereinafter referred to as the subwavelength particles – SP) cannot be considered black or gray radiators. Their radiating capacity and spectral composition of radiation depend not only on the material of the bodies but on their size and shape. There are several known methods for calculating

thermal radiation of SP [1–8]. However, despite the existence of various methods of particles radiation calculation, it cannot be assumed that this problem has sufficiently solved. In this regard, the problem of developing new methods of particles radiation calculation remains relevant. Similar problems arise in the [9-16] radiofrequency range when considering the nature and mathematical formulation of radiation processes of objects with sizes smaller than the radiated (received) wavelength. Developers of transmit-receive modules for mobile communications, Navstar receivers and other microelectronic devices aim to reduce their sizes not only in absolute

 $^{^{1}}$ λ_{max} — wavelengths corresponding to the maximum radiation intensity of the black (gray) body heated to the *T* temperature.

expression but in relation to wavelengths they radiate or receive. Therefore, the issue of reducing the size of objects relative to the radiated or received wavelengths is of great scientific and practical importance.

Calculation methodology justification

In the sphere of radio engineering, attempts to solve this problem were made back in the 40s of the last century. In 1947 and 1959, H. A. Wheeler published articles [9, 10] in which he defined *Electric Small Antenna*, *ESA*. *ESA* are antennas for which the following ratio is valid:

$$K \times \alpha \le 1$$
 (1)

where $2\pi/\lambda$ is a magnitude of propagation vector, α – radius *of Antenna Sphere*, covering the maximum size of the dipolar antenna (or radius of the corresponding hemisphere in the monopole case). In this case, the following ratio is true for *ESA* $(D = 2\alpha)$:

$$(\pi \times D)/\lambda < 1. \tag{2}$$

In [10], the concept of the Radian Sphere, RS, was introduced which is widely used in antenna theory. The surface of this sphere is often interpreted as the reference boundary between near-fields and far-fields created by radiating ESA. Fig. 1 schematically shows a dipolar ESA [10, 11] enclosed in imaginary RS with a diameter of $D_r = \lambda/\pi$, inside which there is an imaginary AS with a diameter of $D = 2\alpha$, covering the maximum size of the actual dipolar antenna. RS surface is the boundary of the near-filed created by ESA. The volume between the spheres contains vibrational energy of electrical and (or) magnetic fields actuated by ESA, i.e. reactive energy that does not propagate into the far-field. Non-propagating fields²

waves in which one component of the wavenumber vector is imaginary. There are no such near-filed components in the far-field zone. At the same time, the *TEM* waves (transverse electromagnetic) actuated in the volume between spheres propagate freely in the far-field beyond the *RS* and form an electromagnetic flux radiated by the antenna.

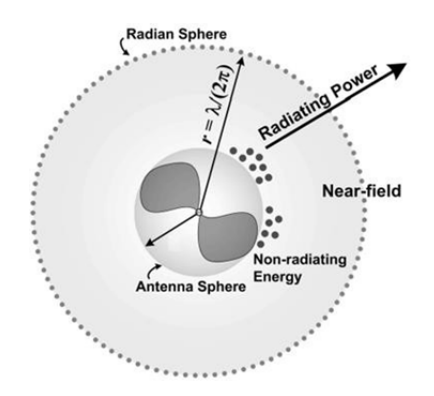


Fig. 1. Dipolar ESA enclosed into imaginary radian sphere

Therefore, we can consider that AS itself does not radiate EM energy to the far-filed (free space). The antenna is needed to create electrical and magnetic fields in its close proximity. And these fields serve as radiation sources, they generate TEM electromagnetic which then propagate waves environment. Indeed. high-frequency potentials of the opposite polarity created by ESA in the dipole arms lead to alternating electric and magnetic fields being actuated in the environment surrounding the dipole. Their intensity (strength) decreases rapidly as the distance from AS boundaries and beyond RS³ of these fields, these fields no longer exist. The space around AS limited by RS is called

² In optics, EM waves of thermal-radiation that do not propagate to the far-field are called evanescent waves.

Developing these considerations, we can imagine *RS* as matching device between the oscillating source and the environment. Its input resistance is equal to antenna equal resistance at the power supply point from oscillating source, and the output resistance is equal to wave impedance of the medium (for vacuum it is 377 Ohm). For electrical dipoles of very small sizes (for example, atoms), the output resistance can be greater than the vacuum wave impedance by many orders of magnitude [17]. As the result, quantum energy at the excited level is radiated "slowly", i.e. in many oscillation periods.

"near-filed". The oscillations of electrical and magnetic fields of the near-filed are shifted in phase relative to each other by an angle close to 90°. Thus, for the source powering the antenna, the near-field is a predominantly a reactive load equivalent by its properties to high-quality LC oscillating circuit. We shall note once again that near-fields created by the ESA radiate into free space. With the help of an antenna, oscillating source pumps energy into the near-field, replenishing its losses, including radiation losses. The near-filed fields are limited by RS. Size of this sphere is an effective size of the radiating virtual antenna. Let us call such a radiator a Radian Emitter, RE and modes radiated by it -Radian Modes, RM.

Radio and optical radiation propagating in free space are TEM waves that differ only in frequency ranges. Considering the above, it can be assumed that for all RE, radiating antennas are not the objects themselves but energy created by them and magnetic fields inside RS. Dimensions of RS equal to $D_R = \lambda/\pi$, are always larger than geometrical dimensions of RE and do not depend in any way on physical dimensions of RE and are determined only by the length of the studied wave.

For example, for hydrogen atom, with a diameter of $D_{\rm H} = 1.58 \times 10^{-10}$ m, radiating one RM on the wavelength of 0.6562×10^{-6} m (transition 3-2 of the Balmer series), the size of the virtual radiating antenna, (i.e. *RS* size) $D_R = \lambda/\pi = 2.089 \times 10^{-7}$ m, and the ratio $D_R/D_{\rm H} = 1.974 \times 10^3$. Thus, the effective size of the radiating antenna of a hydrogen atom is almost 2000 times larger than the atom itself and is commensurate with the radiated wavelength. Then it becomes clear why even an object as small as atom (compared to wavelength) can radiate *TEM* waves to free space.

It follows from (7) (see below) that for all RE (regardless of their size) $M_{\lambda R}$ – is a number of spatiospectral RM radiated by RS in the spatial angle 4π with a wavelength of λ is always equal to one (3).

$$M_{\lambda R} = \left(4\pi \times \frac{\pi D_r^2}{4}\right) / \lambda^2 = 1 \tag{3}$$

Next, let us consider (using the example factors determining of ESA) the dependence of RM energy on the ratio of wavelength to RE size. In 1948 Chu L. J. formulated the fundamentals of O-factor of merit limits for ESA with linear and circular polarization fitted in AS [12]. The Q-factor was characterized by the ratio of the electromagnetic energy W, accumulated inside RS, surrounding ESA, multiplied by ω , to the power P_{rad} , radiated beyond it into the far-field.

$$Q = \omega \times W/P_{rad}, \tag{4}$$

where W is non-radiated energy accumulated either by electric or magnetic (depending on the dipole type), ω means frequency cyclic of electromagnetic oscillations. Chu L. J. obtained approximate expressions for ESA Q-factor in case of vertical linear and circular interpolation at $K \times \alpha \rightarrow 0$. Further, R. F. Harrington [13] specified the theory of Chu L. J. in terms of antenna size influence on the Q value. In the further years, the theory and technique of ESA radio antennas were actively developed: R. E. Collin and S. Rothschild R. C. Hansen [15]McLean J. S. [16] proposed different updated variants mathematical expressions describing dependence of the Q-factor $(K \times \alpha)$ of ESA radio antennas on their relative (compared to the radiated wavelength) dimensions. All dependencies almost coincide these $K \times \alpha < 0.3$.

Development of the mathematical model for calculating power and spectral radiation density of black (gray) bodies and subwave particles

It was noted above that optical, infrared and radio radiations propagating in free space

are *TEM* waves that differ only in frequency ranges so the nature of the fundamental limitations showing the increase in proportion of energy not radiated to far field (relative to the radiated energy) with a decrease of relative dimensions of radiators is the same for both *ESA* radio antennas and for SP and *RE*.

Based on these considerations, in [18] we suggested using the following expressions to develop the new calculation methodology of thermal radiation of SP for *Q* describing dependence of the *ESA* radio antennas Q-factor on their relative geometrical dimensions [13]:

$$Q = \frac{1}{2K^3\alpha^3} + \frac{1}{K\alpha} + \sqrt{\frac{1}{4K^6\alpha^6} + \frac{1}{K^2\alpha^2}}$$
 (5)

$$Q_1 = \frac{1}{K^3 \alpha^3} + \frac{1}{K\alpha} \tag{6}$$

Results of Q calculations according to expression (5) differ little from calculation results according to the simplified expression which is often cited in many works (for example, [11, 14]). Therefore, in the future we will use expression (6).

It is worth noting that ESA antennas do not fully ensure reciprocity between radiation and reception modes. Results obtained for ESA transmitting antennas cannot be fully extended to similar ESA receiving antenna, since the assumption on sphericity⁴ of the radiated waves is not fair for received waves as the front of electromagnetic waves received from the far field region is practically flat. This does not allow to strictly use the reciprocity theorem between radiation and reception modes. Therefore, the dependencies $Q(K, \alpha)$, derived to describe

the radiation processes of ESA radio antennas, we will further use to build a mathematical model describing only the radiation of SP and RE. The processes of thermal-radiation absorption of SP will be calculated using modal theory [5–7, 19]. Based on the idea that thermal radiation propagating in free space in the spatial angle Ω in the form of a polychromatic beam with cross-section S_{csa} at its base can be represented by a set of monochromic rays (spatiospectral modes) [18], the number of which M_{λ} for any wavelength λ of this beam is equal to [6, 20, 21]

$$M_{\lambda} = S_{csa} \times \Omega / \lambda^2 \tag{7}$$

where M_{λ} is a number of spatiospectral modes⁵ of this beam with a wavelength λ .

We will call these modes (unlike RM) normal modes (NM). Let us note that the energy of each NM is defined only by particle temperature and length of the radiated wave while the energy of each RM is defined not only by the temperature and length of the radiated wave but particle size. Subwave particle with D diameter at any $\lambda < 2.221 \times D$ radiates into free space (in the spatial angle $\Omega = 2\pi$) M_{λ} spatiospectral mode, energy of which is determined only by particle temperature T and length of the radiated wave and does not depend on particle size [6, 20, 21]. At $\lambda = 2.221 \times D$ only one mode $(M_{\lambda} = 1)$ with wavelength λ and energy $W_{NM}(v,T)$ will radiate to the far-field. Let us denote this wave as $\lambda_{cutoff} = 2.221 \times D$. At $\lambda > \lambda_{cutoff}$ (according to (7)), the number of freely radiated modes becomes less than one $M_{\lambda} < 1$ and, consequently, SP should not radiate to far-field modes with the wavelengths exceeding λ_{cutoff} .

⁴ In spheric waves radiated by *ESA*, electromagnetic is mainly focused near the radiator's surface in near-fields (reactive fields), which make a small contribution to the far fields which respectively leads to a decrease in radiation factor.

⁵ A spatiospectral mode (oscillation type) is understood as *TEM* wave with specified frequency v, wave-number vector K and polarization ρ_e , where ρ_e is a single polarization vector; e is an index that takes only two values: e = 1, 2 [20, 21].

However, in reality (as will be shown below) SP, in which $M_{\lambda} < 1$, still radiate to the far field at each wavelength $\lambda > \lambda_{cutoff}$ but only one spatiospectral mode. Above we designated these modes as $M_{\lambda R}$ and called them Radian Modes. RM are unusual modes, their energy depends on the ratio of the wavelength to the geometrical size of the radiation source and decreases very rapidly (see fig. 5) as the size of SP decreases relative to the length of radiated waves. Except for SP, for which the inequation $M_{\lambda} < 1$ is only partially fulfilled (only for modes with wavelengths exceeding λ_{cutoff}), it is always fulfilled for such objects as atoms, molecules, clusters and quantum dots. In the radiofrequency range, objects in which the inequation $M_{\lambda} < 1$ is also always fulfilled, are represented by electric small antennas – ESA. All objects radiate these transverse electromagnetic waves that differ only in frequency to the far-field. According to the mechanism of radiation to the far-field, that can be classified as dipolar electrically small antenna.

Subwave particles absorbing or radiating thermal energy can also be considered as dipolar antennas. Indeed, SP which absorb the energy of electromagnetic waves can also be represented as dipole, the dimensions of which are smaller than the absorbed wavelengths.

Under the influence of electric and magnetic fields of incident radiation, oscillations of conductive and (or) bias occur in SP. first approximation, these oscillations are similar to the natural oscillations of an electrical dipole [17]. For waves with $\lambda > \lambda_{cutoff}$ subwave particle (with $M_{\lambda} < 1$) can be considered as ESA. SP together with normal modes (NM), the energy of which is determined only by temperature and length of the radiated wave and does not depend on particle size, can radiate (at $\lambda > \lambda_{cutoff}$) and RM.

In atoms and molecules, electrons make periodic movements around a positively charged nucleus which in the plane of an electronic orbit corresponds to periodic current (charge) oscillations in the dipolar ESA antenna. Since inequation $\lambda \gg \lambda_{cutoff}$ is always fulfilled for wavelengths radiated by atoms, molecules, clusters, quantum dots and ESA, these objects can radiate only RM. Therefore, we will refer the above mentioned objects to RE.

Let us calculate the radiated power for graphite ball the temperature of which is equal to T depending on the frequencies of radiated waves and diameter. Here are the basic relations used in further calculation, in which we use the following designations (dimensions in SI): h, k, c - respectively, Planck's constant, Boltzmann's constant and speed of light, D – ball diameter, S_{csa} – area of ball cross-section, $S_{csa} = \pi D^2/4$, Ω – spatial angle in which hemisphere of the ball surface radiates (absorbs), ε_i – factor of material radiation from which the ball is made. Let us designate $W_{NM}(v,T)$ of one spatiospectral mode NM with frequency v, radiated by black body with temperature T [20, 21]:

$$W_{NM}(v,T) = \frac{hv}{\exp(\frac{hv}{kT}) - 1}$$
 (8)

If $\Psi_{abc}(v,T,D)$ – is the sum of energy radiated into free space and non-radiated energy accumulated in RS^6 , at a frequency v for a time equal to $1/2\pi v$, its value can be calculated by multiplying the number of modes M(v,D), radiated by SP hemisphere in the spatial angle $\Omega = 2\pi$ (in the form of beam with cross-section area S_{csa}), by the energy of each mode $W_{NM}(v,T)$. This product must be multiplied by 4 to consider radiation by two

⁶ Non-radiated energy forms *RS* and accumulates in it at frequencies $v < s/\lambda_{cutoff}$.

hemispheres of the ball surface and two possible polarizations of radiated modes:

$$\Psi_{abc}(v,T,D) = 4\varepsilon_i W_{NM}(v,T) \times M(v,D),$$

where
$$M(v,D) = \frac{S_{csa}\Omega v^2}{c^2}$$
 (9)

It is worth noting that $\Psi_{abc}(v,T,D)$ can also be calculated using Planck's formula according to the following expression:

$$\Psi_{abc}(v, T, D) = \varepsilon_i \pi D^2 \times P_{Plank}(v, T), \qquad (10)$$

here
$$P_{Plank}(v,T) = \frac{2\pi h v^3}{c^2 \exp\left(\frac{hv}{kT}\right) - 1}$$
 (11)

Formulas (8) and (9) are only true for frequencies $v \ge c/\lambda_{cutoff}$, at which the lengths of radiated waves will be less than or equal to λ_{cutoff} . Modes with these frequencies (we designated them as NM) are freely radiated to the far-filed, as in these cases $M_\lambda \ge 1$ and output resistance of the radiator is equal to wave impedance of the medium. For frequencies $v < s/\lambda_{cutoff}$ $M_\lambda < 1$ and virtual radiating antenna becomes not the particle surface but electric and magnetic fields inside RS. In these cases the particles radiate only RM modes.

Let us assume that

$$P_{abc}(v,T,D) = \omega \times \Psi_{abc}(v,T,D) =$$

$$= 2\pi v \times \Psi_{abc}(v,T,D)$$
(12)

where $P_{abc}(v,T,D)$ is the sum of the power radiated by the particle into free space and non-radiated reactive power of electrical and (or) magnetic oscillations at the v frequency inside RS. Let us designate $\Psi_R(v,T,D)$ non-radiated into free space energy (reactive energy) of electrical and (or) magnetic oscillations at the v frequency accumulated for $1/2\pi v$ time inside RS and $P_R(v,T,D)$ non-

radiated into free space power (reactive power) of electrical and (or) magnetic oscillations at the v frequency inside RS, then

$$P_{R}(v,T,D) = \omega \times \Psi_{R}(v,T,D) =$$

$$= 2\pi v \times \Psi_{R}(v,T,D)$$
(13)

If $P_{rad}(v,T,D)$ is power radiated by the particle into free space at frequency v, the expression for Q(v,D) will be written down according to (4) and (6) as follows:

$$Q_{1}(v,D) = \frac{\omega \times \Psi_{R}(v,T,D)}{P_{rad}(v,T,D)} =$$

$$= \frac{c^{3}}{\pi^{3}D^{3}v^{3}} + \frac{c}{\pi Dv}$$
(14)

We will assume that

$$P_{abc}(v,T,D) = P_R(v,T,D) + P_{rad}(v,T,D), \quad (15)$$

then
$$P_{rad}(v,T,D) = \frac{P_{abc}(v,T,D)}{Q_1(v,D)+1}$$
 (16)

and, accordingly,

$$P_{R}(v,T,D) = Q_{1}(v,D) \times P_{rad}(v,T,D) \quad (17)$$

For comparison, let us present the following expression for the calculation of spectral powers using Planck's formula:

$$P_{Pabc}(v,T,D) = 2\pi v \varepsilon_i \pi D^2 P_{Plank}(v,T), \qquad (18)$$

$$P_{Prad}\left(\mathbf{v},T,D\right) = \frac{P_{Pabc}\left(\mathbf{v},T,D\right)}{Q_{1}\left(\mathbf{v},D\right)+1},$$
(19)

where $P_{Pabc}(v,T,D)$ is the sum of power radiated by the particle into free space and non-radiated power (reactive power) of electrical and (or) magnetic oscillations at the v frequency inside the radian sphere, calculated using Planck's formula and

 $P_{Prad}(v,T,D)$ – power radiated by the particle into free space at the v frequency calculated using Planck's formula. Let us note that the above expressions are only fair for single-frequency operation both for *ESA* radio antennas and SP.

Discussion of the calculation results

Fig. 3 shows the dependences of radiated and non-radiated power from v frequency calculated for graphite ball with a diameter of 3×10^{-6} m heated up to temperature T = 1273 K.

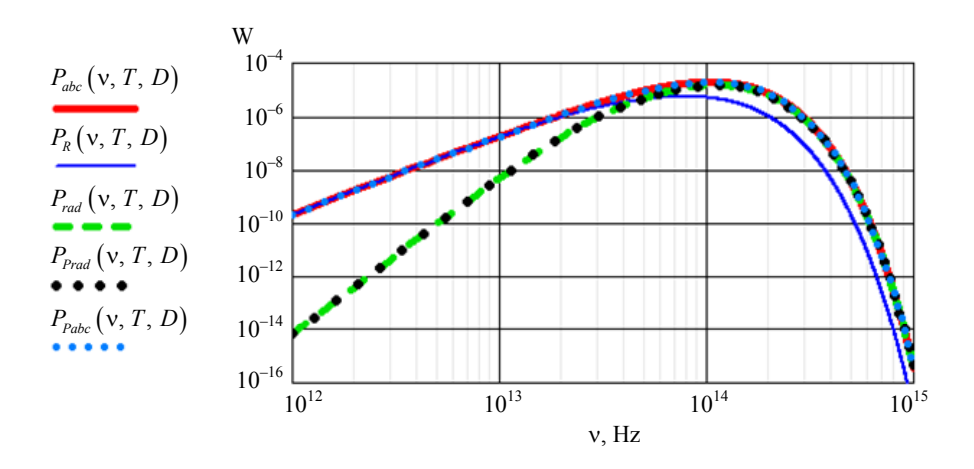


Fig. 2. Dependencies $P_{abc}(v,T,D)$, $P_{R}(v,T,D)$, $P_{rad}(v,T,D)$ on frequencies v are calculated using the representation of the radiated energy flow by a set of spatiospectral modes. The dependencies $P_{Prad}(v,T,D)$, $P_{Pabc}(v,T,D)$, are calculated (for comparison) using Planck's formula. All dependencies are calculated at $D=3\times10^6$ m, $\varepsilon_i=0.7$ and T=1273 K

Calculation results show that $P_{abc}(v,T,D)$ is a dependence based on the representation of heat flow as in the form of set of powers of monochromic rays (spatial modes), completely coincides with $P_{Pabc}(v,T,D)$ – dependence based on the Planck's formula⁷. At the same time for $v \ge 1 \times 10^{14} \text{ Hz}$ (i.e at ν dependencies $P_{abc}(v,T,D)$ and $P_{Pabc}(v,T,D)$ practically coincide with the dependence of radiated power $P_{rad}(v,T,D)$. $v \le 5 \times 10^{13} \text{ Hz (i.e at } v < \text{s/}\lambda_{cutoff}) P_{rad}(v, T, D)$

is a power radiated into free space becomes less than $P_R(v,T,D)$ – non-radiated power and decreases faster with the decrease of v, than shown by the dependencies $P_{abc}(v,T,D)$ and $P_{Pabc}(v,T,D)$. This proves that at M < 1 the Planck's formula is not suitable for calculation of spectral powers of the radiation of objects which we called RE above.

Expression $P_{Prad}(v,T,D)$ fully identical to the expression $P_{rad}(v,T,D)$, obtained using the representation of the energy flow a radiated with of spatiospectral modes. Thus, for the calculation of spectral powers of radiation of SP of any size and at any temperatures we can use any of these dependences: $P_{Prad}(v,T,D)$ or $P_{rad}(v,T,D)$. The curve $P_{rad}(v,T,D)$ shows that the decrease v (i.e the decrease of particle

⁷ This shows full identity of the formula obtained by us (using the representation of the radiated energy flow with a set of spatiospectral modes) $\Psi_{abc}(v,T,D) = 4\varepsilon_i W_0(v,T) \times M(v,D)$ with the Planck's formula Thus $\Psi_{abc}(v,T,D)$ this is another variant of writing Planck's spectral dependence.

size according to λ) leads to the decrease (compared to $P_{Pabc}(v,T,D)$ calculated using the Planck's formula) of radiation powers at wavelengths and, consequently, to the increase of relative share of short waves. Thus, the color of the radiating particle becomes "bluer" than it follows from the Planck's formula.

The identity of expressions (16) and (19) was shown above (see fig. 2) and consequently, the suitability of expression (19) for the calculation of radiation powers not only for "large" bodies but subwave particles. Formula (19) can be represented as follows: $P_{\text{Pr}ad}(v,T,D) = 2\varepsilon_i \pi v S_s \times \chi(v,T,D)$ (20), where $S_s = \pi D^2$ is the surface area of spherical particle

$$\chi(v,T,D) = \left[1 + \frac{c}{\pi v D} + \left(\frac{c}{\pi v D}\right)^{3}\right]^{-1} \times \left(\frac{2\pi h v^{3}}{c^{2}}\right) \times \frac{1}{\exp\left(\frac{h v}{kT}\right) - 1}$$
(21)

Here $\chi(\lambda, T, D)$ – radiating capacity of the particle at frequency ν (i.e spectral density of the radiation power per area unit). Expression (21) is a modification of the Planck's formula for calculating radiating capacities not only for large bodies but for SP.

Thus, we obtained a universal formula which is suitable for calculating radiating capacities both for large bodies and SP. In wavelengths, this formula is expressed as follows

$$\chi(\lambda, T, D) = \left[1 + \frac{\lambda}{\pi D} + \left(\frac{\lambda}{\pi D}\right)^{3}\right]^{-1} \times \left(\frac{2\pi hc^{2}}{\lambda^{5}}\right) \times \frac{1}{\exp\left(\frac{hc}{\lambda kT}\right) - 1}$$
(22)

or

$$\chi(\lambda, T, D) = \left[1 + \frac{D_r}{D} + \left(\frac{D_r}{D}\right)^3\right]^{-1} \times \left(\frac{2\pi hc^2}{\lambda^5}\right) \times \frac{1}{\exp\left(\frac{hc}{\lambda kT}\right) - 1}$$
(23)

Fig.-3 shows dependence of spectral radiating capacities (spectral densities of radiation flows) of spherical particles from λ :

- $-P_{Plank}(\lambda,T)$ spectral radiating capacity of the "large" body calculated according to the classical Planck's formula;
- $-\chi(\lambda, T, D)$ spectral radiating capacities of SP calculated according to formula (22), i.e modified Planck's formula for different D values.

It can be seen that the dependencies $P_{Plank}(\lambda,T)$ and $\chi_1(\lambda,T,D)$ almost coincide at all $\lambda < 3 \times 10^{-4}$ m. Consequently, particles with a diameter $D \ge 2 \times 10^{-4}$ m in the entire spectral range under consideration radiate only NM (as "large" body). At the particle size decreases, transition from NM to RM radiation is carried out. For example, for dependence $\chi_2(\lambda,T,D_2)$ – at $\lambda > 4.2 \times 10^{-5}$ m; for dependence $\chi_3(\lambda,T,D_3)$ – at $\lambda > 4.2 \times 10^{-6}$ m; for dependence $\chi_4(\lambda,T,D_3)$ – at $\lambda > 4.2 \times 10^{-7}$ m. Particles with $D < 10^{-8}$ m (at T = 1273 K) radiate only RM and, consequently, as atoms, molecules, clusters and quantum dots are radian radiators.

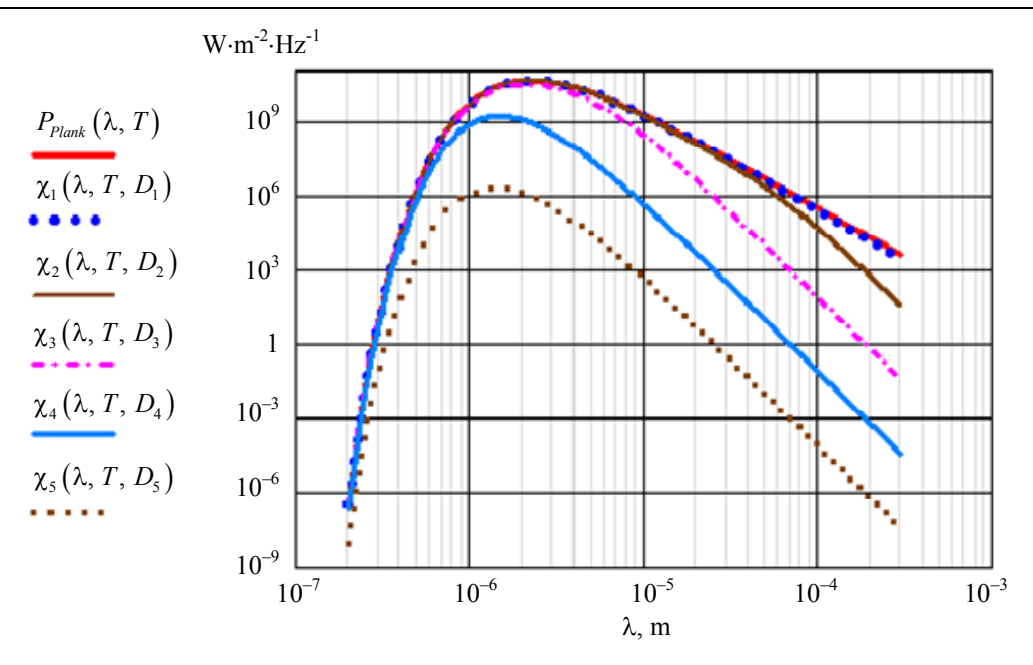


Fig. 3. Dependence of spectral radiating capacities of "large body" and SP on v. The calculations were carried out with the following parameter values: T = 1273 K and $D_1 = 2 \times 10^{-4} \text{ m}$; $D_2 = 2 \times 10^{-5} \text{ m}$; $D_3 = 2 \times 10^{-6} \text{ m}$; $D_4 = 2 \times 10^{-7} \text{ m}$; $D_5 = 2 \times 10^{-8} \text{ m}$

The above dependencies show the limits of the Planck's formula applicability. At T = 1273 K, the Planck's formula is only suitable for calculating radiation of particles with $D > 2 \times 10^{-4}$ m. At the same time, the modified formula (21) or (22) obtained as a result of this work is suitable for calculating radiation of both "large bodies" and subwave particles. The above dependencies $\chi(v, T, D)$

show that errors when using the Planck's formula for calculating spectral radiating capacities of SP can reach (in the considered example) several orders of magnitude.

Fig. 4 shows $\chi(\lambda, T, D)$ – dependencies of spectral radiating capacities of physical particles on their diameters, calculated at different λ values.

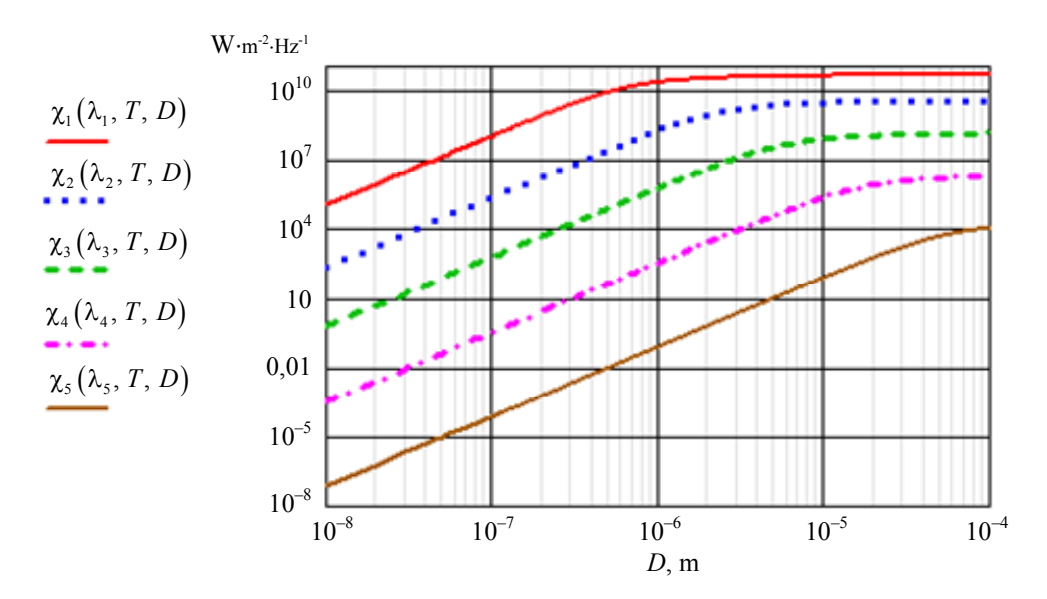


Fig. 4. $\chi(\lambda, T, D)$ – dependencies of spectral radiating capacities of physical particles on their diameters, calculated at T = 1273 K and the following λ values: $\lambda_1 = 2.28 \times 10^6$ m; $\lambda_2 = 8 \times 10^6$ m; $\lambda_3 = 2 \times 10^5$ m; $\lambda_4 = 6 \times 10^5$ m; $\lambda_5 = 2 \times 10^4$ m

At wavelength λ_1 all particles with $D < 1 \times 10^{-5}$ m radiate only RM, and particles with $D > 1 \times 10^{-5}$ m radiate NM (their spectral radiating capacity does not depend on D).

At wavelength λ_2 particles with $D < 3.5 \times 10^{-5}$ m radiate only RM, and particles with $D > 3.5 \times 10^{-5}$ m radiate NM (their spectral radiating capacity does not depend on D).

At wavelength λ_3 all particles with $D < 8 \times 10^{-5}$ m radiate only RM, and particles with $D > 8 \times 10^{-5}$ m radiate NM (their spectral radiating capacity does not depend on D).

At wavelengths λ_4 and λ_5 particles with $D < 4 \times 10^{-4}$ m radiate only *RM*.

The above dependencies show the change of radiation modes composition depending on the particles size and frequency (length) of the radiated wave. For example, particles with $D = 1 \times 10^{-4}$ m radiate NM on wavelengths λ_1 , λ_2 , λ_3 and at the same time radiate RM on wavelengths λ_4 , λ_5 .

Using expression (8) and (16) we can obtain $P_M(D, v, T)$ – single formula suitable for power calculation both for NM and RM:

$$P_{M}(v,T,D) =$$

$$= 2\pi v \times (Q_{1}(v,D) + 1)^{-1} \times W_{NM}(v,T)$$
(23)

In wavelengths formula (23) shall be written as follows:

$$P_{M}(\lambda, T, D) = \left(\frac{\lambda}{\pi D} + \frac{\lambda^{3}}{\pi^{3} D^{3}} + 1\right)^{-1} \times \frac{2\pi h c^{2}}{\lambda^{2} \left(\exp(\frac{hc}{\lambda kT}) - 1\right)}$$
(24)

Fig. 5 shows dependence of power radiated by black ($\varepsilon_I = 1$) ball in one spatiospectral mode on its diameter.

It can be seen that at $D > 8 \times 10^{-5}$ m, the mode power does not depend on D and, consequently, at $D > 8 \times 10^{-5}$ m, particles

radiate only NM. At $D < 8 \times 10^{-5}$ m, the power decreases as D decreases and, consequently, at $D < 8 \times 10^{-5}$ m, particles radiate only RM. Thus, using formula (24), we can calculate power radiated in one spatiospectral mode not only of "large" bodies but subwave particles also.

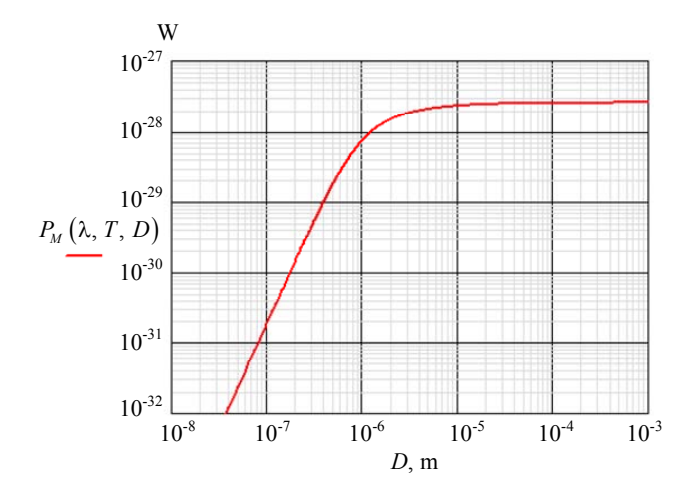


Fig. 5. Power dependence $P_M(\lambda, T, D)$ radiated by black ($\varepsilon_I = 1$) ball in one spatiospectral mode on its diameter. The calculation was conducted using formula (24) at T = 1273 K and $\lambda = 3.5 \times 10^{-6}$ m

Main results

A new method for calculating spectral powers and spectral radiant emissivity of SP, based on the ideas described above on the radiation mechanism of subwave particles, suggested, where calculations performed using the dependence of the Q-factor of small electric radio antennas (ESA) on their relative (relative to the length of the radiated wave) dimensions. obtained a formula for calculating spectral radiation density of black (gray) bodies and subwave particles. (The suggested formula is a modification of the Planck's formula for calculating radiating capacities not only for "large" bodies but for SP.) We deprived a ratio for calculating power radiated in one spatiospectral mode not only of "large" bodies but subwave particles. Introduced concepts: Normal mode (NM), radian mode (RM) and radian emitter (RE). New version of representation of spectral dependencies of Planck and Stefan-Boltzmann were introduced.

REFERENCES

- 1. Mie G., Annalen der Physik **25**, 377 (1908). https://doi.org/10.1002/andp.19083300302
- 2. Boren K. and Hafman D., Absorption and scattering of light by small particles, Moscow, Mir, 1986 [in Russian].
- 3. Martynenko Yu. V. and Ognev L. I., ZhTF (Technical Physics) **75** (11), 130–132 (2005) [in Russian]
- 4. Elzukal M., Jan Ch., Albert A., Lubner S. and Prasher R., Cell Reports Physical Science 1 (12), 100259 (2020).
- https://doi.org/10.1016/j.xcrp.2020.100259
- 5. Sviridov A. N. and Saginov L. D., Journal of Communications Technology and Electronics **67** (Suppl. 1), S83–S88 (2022).
- 6. Sviridov A. N. and Saginov L. D., Applied Physics, No. 2, 12–21 (2021) [in Russian].
- 7. Sviridov A. N. and Saginov L. D., Applied Physics, No. 3, 17–25 (2021) [in Russian].
- 8. Knyazev B. A. and Kuzmin A. V., Bulletin of the NSU. Series: Physics **2** (1), 108–122 (2007) [in Russian].
- 9. Wheeler H. A. Proc. of the IRE, December, 1479–1488 (1947).

- 10. Wheeler H. A., Proc. IRE **47** (Aug), 1325–1331 (1959).
- 11. Davis W. A., Yang T., Caswell E. D. and Stutzman W. L., IET Microwaves Antennas & Propagation **5** (11), 1297–1302 (2011). doi: 10.1049/iet-map.2010.0604
- 12. Chu L. J., Journal of Applied Physics **19** (December), 1163–1175 (1948).
- 13. Harrington R. F., J. Res. Nat. Bur. Stand. **64-D** (Jan/Feb), 1–12 (1960).
- 14. Collin R. E. and Rothschild S., IEEE Trans. Ant. Prop. **AP-12** (Jan.), 23–27 (1964).
- 15. Hansen R. C., Proceedings of the IEEE **69** (2), 170–182 (1981).
- 16. McLean J. S., IEEE Trans. Ant. Prop. **44** (5), 672–676 (1996).
- 17. Khlebtsov B. N., Mathematical modeling, computer and physical experiments in natural sciences, No. 2 (2016). URL: mathmod.esrae.ru/2-10 [in Russian].
- 18. Sviridov A. N. and Saginov L. D., Journal of Communications Technology and Electronics, **69** (4–6), 158–167. (2024).
- 19. Sviridov A. N. and Saginov L. D., Journal of Communications Technology and Electronics **68** (Suppl. 2), S176–S183 (2023).
- 20. Gagliardi R. M. and Karp Sh., Optical communication, New York, London, John Wiley & sons, 1976; Moscow, Svyaz, 1978.
- 21. Friedrichov S. A. and Movnin S. M., Physical foundations of electrical engineering. Moscow, Higher School, 1982. pp. 148, 608 [in Russian].

About authors

Anatolii Nikolaevich Sviridov, Senior Staff Scientist, Candidate of Physical and Mathematical Sciences, Федеральный научный агроинженерный центр ВИМ (109428, Russia, Moscow, 1st Institutsky Passage, 5). E-mail: sviridtoly@yandex.ru Author ID 171370

Leonid Dmitrievich Saginov, Doctor of Physical and Mathematical Sciences, Leading Research Associate, FSAC VIM (109428, Russia, Moscow, 1st Institutsky Passage, 5). E-mail: lsaginov@yandex.ru SPIN code 1677-3738, Author ID 171369

Renat Zakirovich Khafizov, Senior Staff Scientist, Candidate of Physical and Mathematical Sciences, head of research center, ODB «ASTROHN» JSC (140080, Russia, Moscow Region, Lytkarino, Parkovaya 1 st.) E-mail: imagelab@mail.ru SPIN code 3045-0138, Author ID 725980

PHOTOELECTRONICS =

UDC 535.24 PACS: 42.62.Eh EDN: MIHBWS

Integral transmittance express control method for optical elements

© A. V. Polesskiy*, N. A. Semenchenko, Sh. I. Zaripov and D. A. Mashoshin

RD&P Center ORION, JSC, Moscow, 111538 Russia *E-mail: polesskiyav@orion-ir.ru

Received 16.06.2025; revised 4.07.2025; accepted 11.08.2025 Scientific specialty code: 2.2.6

The article presents development and technical implementation results of express control method of the optical elements integral transmittance using a sample-satellite using FPA. Transmittance measurement is based on the differential radiation flux measurement. Small modifications of the method allow it to be used to measure the optic material integral internal transmittance (or absorption) and measurement the lens integral transmittance coefficient.

Keywords: integral transmittance; measurement; measurement error; optical element; matrix photodetector; differential radiation flux.

DOI: 10.51368/1996-0948-2025-4-16-23

Introduction

During the organization and massproduction of optical components it is necessary to control a number of parameters, among which one of the most important is transmission coefficient. The most popular control method is currently spectrum analysis method [1], which measures the dependence of the transmission coefficient on the wavelength and its further integration in a given wavelength. This method is popular and has proven itself but requires and expensive spectrophotometer for implementation. Disadvantages of this method include that in order to fully analyze the operation of the measured optical components as part of the optical-electronic device (OED) you have to consider spectral characteristics of background target environment in which the OED operates and spectral sensitivity of the OED detector.

Due to the need to measure optical components during the producing considering the spectral sensitivity of the target OED detector, as well as background target environment, an express-control method of the integral transmission coefficient of optical components which has no disadvantages was developed and proposed. The following tasks were solved when developing the method

- the method should allow simulating the background target environment which can be observed when operating the OED;
- the method should ensure spectral characteristics of the OED detector;
- the method should ensure high repeatability of measurements;
- the method must should be resistant to glares and re-reflections which can occur during measurements;
- the method should have high performance for fast measurements.

Initial data for the development of express-control method

The starting point for the method development the photoelectric was photometer method, which establishes the procedure for determining the transmission coefficient of a lens in a visible and nearinfrared region of the spectrum. The method is based on comparing the directed radiation flux falling on the lens and the flux passing through the lens using single-element radiation detector. This method has a high accuracy and ensures the determination of the transmission coefficient with an absolute error of ± 0.02 at $\tau > 0.1$ [2]. The test bench schematic diagram is shown in fig. 1.

Measurements in this method are carried out in two stages: with and without a controlled product – for determining the falling flux value. Technical implementation of the method is represented by the system consisting of a illuminator 1 and a collimator lens 2 which forms a parallel beam of the

radiation flux, then the diaphragm 3 form an identical in value radiation flux during measurement both with and without the controlled product. The radiation flux is detected by a single-element photodetector 4. the same time, the size photosensitive area is bigger than diaphragm size, which allows to detect the full flux value. Next, a controlled lens is installed behind the diaphragm 4, and part of the radiation flux is lost when passing through it, and then there is the photodetector that detects the radiation flux passing through the lens. At the same time, an defocused image is allowed on the photodetector but its size should not exceed the limits of the photodetector photosensitive element. At the second stage of measurement the controlled product is removed from the ray path and the radiation value corresponding to the radiation flux falling on the controlled product is detected. The ratio of the values of the signals on the measuring device will be an integral transmission coefficient.

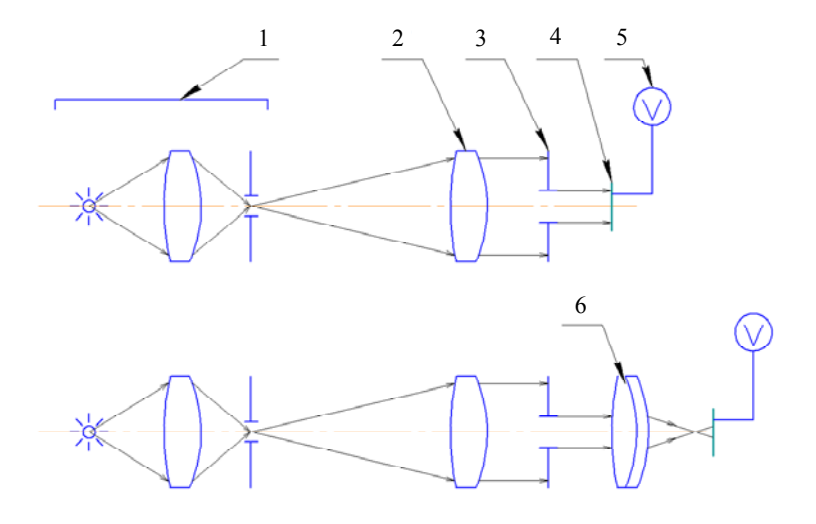


Fig. 1. Schematic diagram of the test bench for measuring the integral transmission coefficient of lenses by the photoelectric photometer method:
1 – illuminator; 2 – collimator lens;
3 – diaphragm; 4 – photodetector;
5 – measuring instrument; 6 – controlled lens

Technical implementation of this method is actually more complicated. It additionally includes optical filters to form a given background target environment, non-transparent screen between the diaphragm and the photodetector to eliminate the constant signal component in the absence of the falling radiation flux and check of the linearity of the photodetertor transmission characteristics.

Development of express-control method

The method has undergone several iterations and has gone from the initial concept to the final version through several development stages. The method was developed for two spectral ranges 0.4–1.7 μ m and 8–14 μ m, however, there are no photodetectors with a large photosensitive area for these spectral ranges.

The solution to this problem was the use of a matrix photodetector with the specified range of spectral sensitivity. Such replacement allowed to carry out measurements in the required spectral range of wavelengths and simplified the process of assembly and alignment, however, it caused a number of problems. The first problem was the dynamic range of matrix photodetectors is limited by the dynamic range of the LSI accumulation capacitance and significantly lower than in single-element dynamic range of photodetectors with readout LSI is about 5×10^3 times. While for one-element photodetectors it reaches 10⁶ times [3, 4]. Therefore, in the process of measurements in the range of $0.4-1.7 \mu m$, an "overexposure" of the matrix is often observed which has to be compensated either by defocusing of the controlled lens or by changing the integration time (taking this into account in further calculations). The second problem was that generation of a powerful energetic flux in the range from 8–14 µm is a quite tricky question which resulted in the fact that during measurements the flux falling on each pixel was commensurate with the threshold which in turn led to the need of additional system calibration. At the same time, the time drift of the signal on the microbolometric matrix during the measurement, including lens installation and focusing, as well as different variable background illuminations and rereflections led to large measurement errors (up to 500 %) in the range from $8-14 \mu m$.

Thus, it was necessary to further improve the method to find solutions to the above problems, in particular, to reduce the effect of time drift of the matrix signal, overflux elimination of the matrix accumulation cells and ensuring resistance to the variable background illuminations. These problems were eliminated by modifying the method, in particular, the improved method ensures the transmission coefficient measurement in single frame, does not use intermediate image focusing and works based

on measuring changes in the differential radiation flux while passing through the controlled sample.

Measuring diagram of the differential radiation flux is show in figure 2.

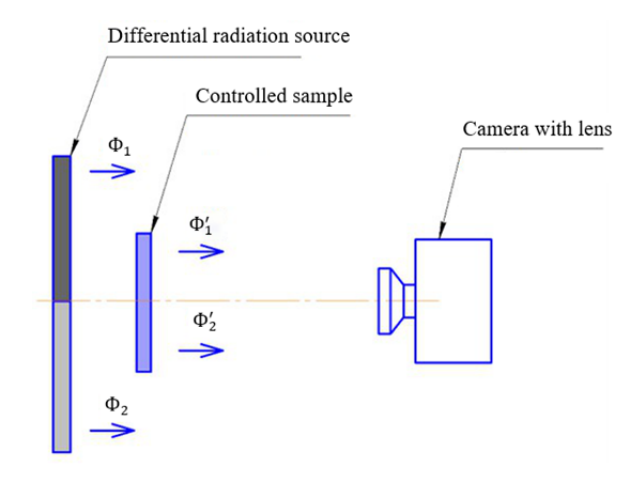


Fig. 2. Measurement diagram of the differential radiation flux during measurements

The differential radiation source form two fluxs Φ_1 and Φ_2 which pass through the controlled sample and decrease by the value of the integral transmission coefficient according to the dependencies:

$$\Phi_l' = \Phi_l \cdot \tau_{int}, \qquad (1)$$

$$\Phi_2' = \Phi_2 \cdot \tau_{\text{int}}, \tag{2}$$

where Φ_1 is the radiation flux from the bright (hot) part of the radiation source;

 Φ_2 is the radiation flux from the dark (cold) part of the radiation source;

 τ_{int} – integral transmission coefficient of the controlled sample;

 Φ_1 and Φ_2 – radiation fluxs corresponding to fluxs Φ_1 and Φ_2 , passing through the controlled sample.

For clarity, the integral transmission coefficient is the ratio of the transmitted radiation flux to the falling radiation flux value in the specified spectral range. In the developed method it is necessary to prove the validity of application of the differential radiation flux and identity of the obtained result to definition:

$$\frac{\Phi_{2}' - \Phi_{1}'}{\Phi_{2} - \Phi_{1}} = \frac{\Phi_{2} \cdot \tau_{int} - \Phi_{1} \cdot \tau_{int}}{\Phi_{2} - \Phi_{1}} = \tau_{int}.$$
 (3)

Thus, the measurement of the integral transmission coefficient using differential flux is possible. Additional advantage of using the differential radiation flux is the method's resistance to background illuminations and re-reflections. The patterns background illuminations and reflections for two typical cases are shown in fig. 3. In the first case (fig. 3a) there is an external source creating a background flux which falls on the controlled sample and reflects from it, at the same time, the sample protects the area of the differential radiation source from being impacted by a radiation flux from the external source. In this case,

the falling background flux is reflected from the differential source region not protected by the sample. This describes the case when the background radiation source is behind the matrix photodetector. The second case is characteristic for the side illumination when the background radiation flux is reflected from the entire differential source and controlled sample.

Expressions (4) and (5) confirm that the method is resistant to the uniform background illumination and re-reflections corresponding to figures and 3*b*. uniformity of the background illumination can be ensured due to the maximum convergence of the measurement areas of all four radiation fluxs or applying of light-diffusing screens.

$$\frac{\left(\Phi_{2}' + \Phi_{\text{ref},2}\right) - \left(\Phi_{1}' + \Phi_{\text{ref},2}\right)}{\left(\Phi_{2} + \Phi_{\text{ref},1}\right) - \left(\Phi_{1} + \Phi_{\text{ref},1}\right)} = \frac{\left(\Phi_{2} \cdot \tau_{\text{int}} + \Phi_{\text{ref},2}\right) - \left(\Phi_{1} \cdot \tau_{\text{int}} + \Phi_{\text{ref},2}\right)}{\Phi_{2} - \Phi_{1}} = \tau_{\text{int}}$$
(4)

$$\frac{\left(\Phi_{2}' + \Phi_{\text{ref},2}\right) - \left(\Phi_{1}' + \Phi_{\text{ref},2}\right)}{\left(\Phi_{2} + \Phi_{\text{ref},1}\right) - \left(\Phi_{1} + \Phi_{\text{ref},1}\right)} = \frac{\left(\left(\Phi_{2} + \Phi_{\text{ref},1}\right) \cdot \tau_{\text{int}} + \Phi_{\text{ref},2}\right) - \left(\left(\Phi_{1} + \Phi_{\text{ref},1}\right) \cdot \tau_{\text{int}} + \Phi_{\text{ref},2}\right)}{\Phi_{2} - \Phi_{1}} = \tau_{\text{int}}$$
(5)

where $\Phi_{ref.1}$ is a background radiation flux, reflected from a differential radiation source; $\Phi_{ref.2}$ is a background radiation source reflected from a controlled sample.

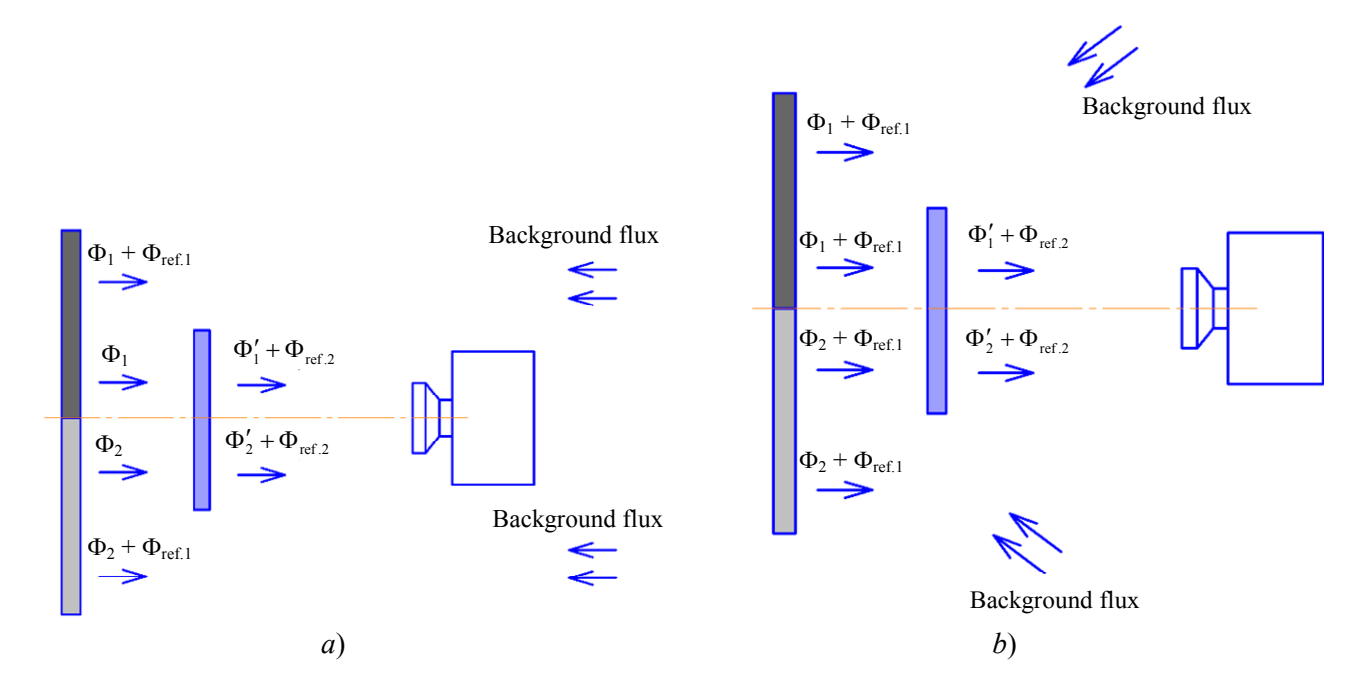


Fig. 3. Patterns of re-reflection and background illumination occurrence during measurements

The limitation of the developed method is that it allows to conduct express-control only of plane-parallel plates. At the same time, this method can be used as a basis for integral internal transmission (or absorption) coefficient of the material measurement: for this it is necessary to measure the integral transmission coefficient in accordance with it. calculate the Fresnel reflection component [5] at a known material refractive index and calculate the required value. It is also possible measure the integral transmission coefficient of the lens by measuring the integral transmission coefficient of samplesatellite of all lenses included in the lens.

Fig. 4 schematically shows an image on the matrix photodetector when measuring the integral transmission coefficient by the developed method in the spectral range of $8-14~\mu m$.

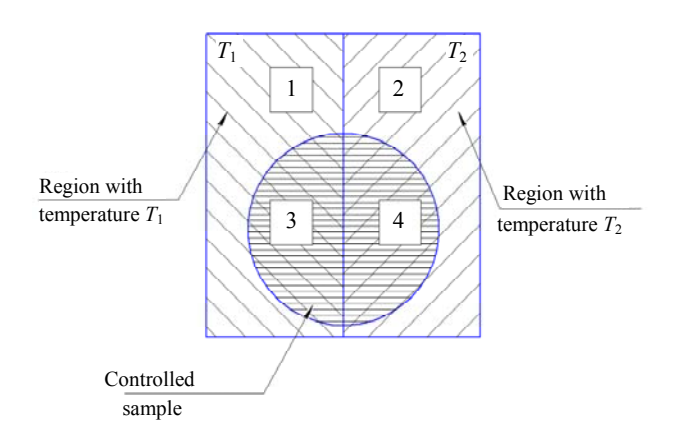


Fig. 4. Schematic view of the image during measurements using the differential radiation source

One of the important stages of the method development is estimation measurement error [6]. When calculating the error, it is necessary to consider that the matrix photodetector does not measure the radiation flux, it converts the flux in each pixel into an electrical signal, which is for the ideal photodetector is directly proportional to the falling flux. Then there is a series of transformations which should also be linear and at the output of each pixel we obtain ADC codes that are registered [7]. Since due

to a number of optical restrictions the size of the measured area should be at least 15×15 pixels, the average pixel value of the signal in the radiation flux measurement zone should be taken as the signal value, while edge effects should be excluded. Signal values measurement is carried out in regions 1–4 (fig. 4). Measurement error of the integral transmission coefficient is calculated according to the following formula

$$\Delta \tau_{\text{sample}} = \left(\frac{\Delta U_3}{U_1 - U_2} \right)^2 + \left(\frac{\Delta U_4}{U_1 - U_2} \right)^2 + \left(\frac{U_3 - U_4}{(U_1 - U_2)^2} \Delta U_1 \right)^2 + \left(\frac{U_3 - U_4}{(U_1 - U_2)^2} \Delta U_2 \right)^2, \tag{6}$$

where ΔU_1 , ΔU_2 , ΔU_3 , ΔU_4 is signal measurement error;

 U_1 , U_2 , U_3 , U_4 – signal or temperature values in regions 1–4.

Since in most cases the measurement signal error for thermal images are equal to each other, expression (6), considering the introduction of the confidential probability 0.95 can be written as follows

$$\Delta \tau_{\text{sample}} = 1.96 \cdot \frac{\Delta U}{U_1 - U_2} \sqrt{2 \cdot \left(1 + \left(\frac{U_3 - U_4}{U_1 - U_2}\right)^2\right)}, (7)$$

where ΔU is the signal (temperature) measurement error equal to the thermal sensitivity threshold of the IR camera with the matrix photodetector.

It can be seen from the expression (7), that the method is more accurate when the ratio between the differential flux and threshold device flux with which the measurements are made is greater. Simulation of the measurement processes showed that in most cases the measurement error of the integral transmission coefficient, including the methodological one, should not exceed ± 2.5 % at confidential probability 0.95.

Confirmation of metrological specifications of the express-control method

An example of the technical implementation of the express-control method for the integral transmission coefficient of the controlled sample in the spectral range of 8–14 µm is shown in figure 5.

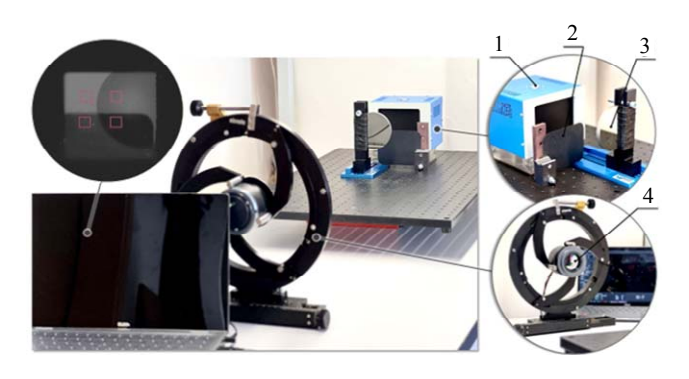


Fig. 5. Appearance of the test bench for measuring the integral transmission coefficient of the controlled sample

The "hot" part of the differential radiation source is the radiating cavity of the TBB (pos. 1 in fig. 5), the "cold" part – any body with the high radiation coefficient in the spectral range of $8-14~\mu m$ (for example, dense mat board) having a room temperature (pos. 2 in fig. 5). The controlled sample is fixed on the holder in front of TBB (pos. 3 in fig. 5). Mutual alignment of the differential radiation source and the controlled sample in the field of view of the thermal vision camera

(pos. 5 in fig. 5) must provide an image corresponding to fig. 4. Special software allows to obtain images from cameras based on matrix photodetectors operating in the spectral ranges of $0.4-1.7~\mu m$ and $8-14~\mu m$, to select areas for measuring radiation fluxs both directly from the differential radiation source and passing through the controlled sample.

To conduct the studies of metrological specifications of the method, multiple measurements of the same object were carried out at different values of the differential flux which was provided due to the temperature difference between the TBB and the "background" (object with room temperature). The method of the expresscontrol of the integral transmission coefficient was also compared with spectrum analysis method, while the spectral characteristics of the radiation receiver and spectral characteristics of the differential source were taken into account. The comparison was conducted qualitatively since the error of a number of parameters for the spectrum analysis method was not reliably known.

Fig. 6 shows the random error in measuring the integral transmission coefficient of the controlled sample by the developed method depending on the TBB temperature and temperature difference between the TBB and the "background".

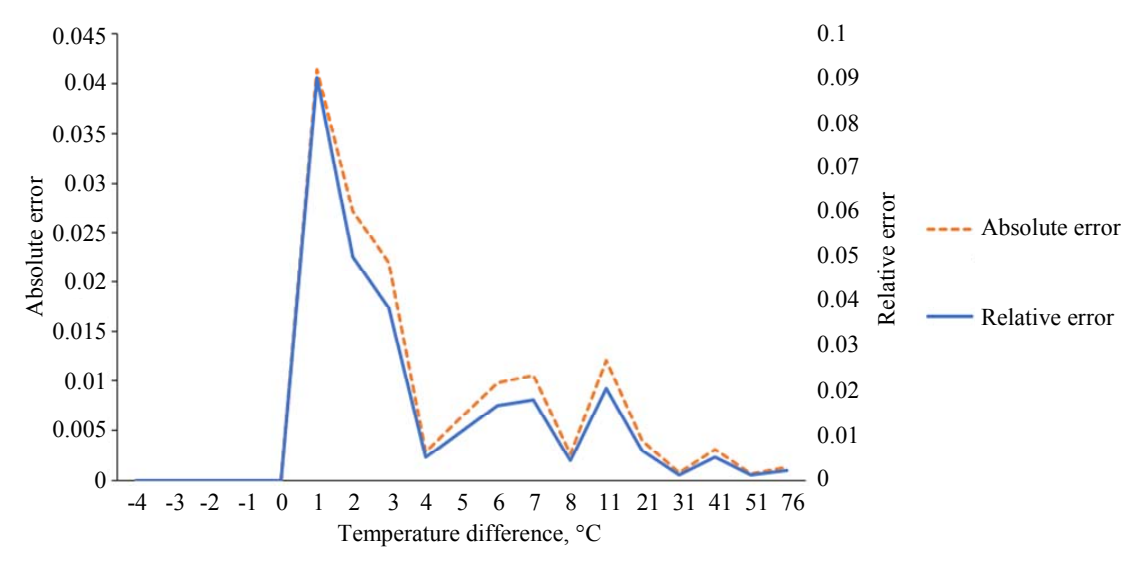


Fig. 6. Graphs of the random component of the absolute and relative measurement errors

As can be seen from the figure, with a difference of temperatures more than 10 °C, a random component of the measurement error at confidential probability of 0.95 does not exceed 2 %. If the temperature difference is smaller, the error increases up to 10 %, which corresponds to the dependence (7) and is explained by the fact the measurement error on the ratio of the depends signal (temperature) measurement error and the value of the measured signal (i.e on the signal/noise ratio value).

Fig. 7 shows diagrams used to conduct the qualitative comparison of the results of the developed express-method with the spectroscopy method. The red line shows the spectral transmission coefficient of the sample, the blue – spectral characteristic of the radiation detector, the green – spectral radiance of the TBB.

The conducted calculations showed that for the studied sample the integral transmission coefficient under the specified measurement conditions was 60.8 % and the actually measured was 59.5 %.

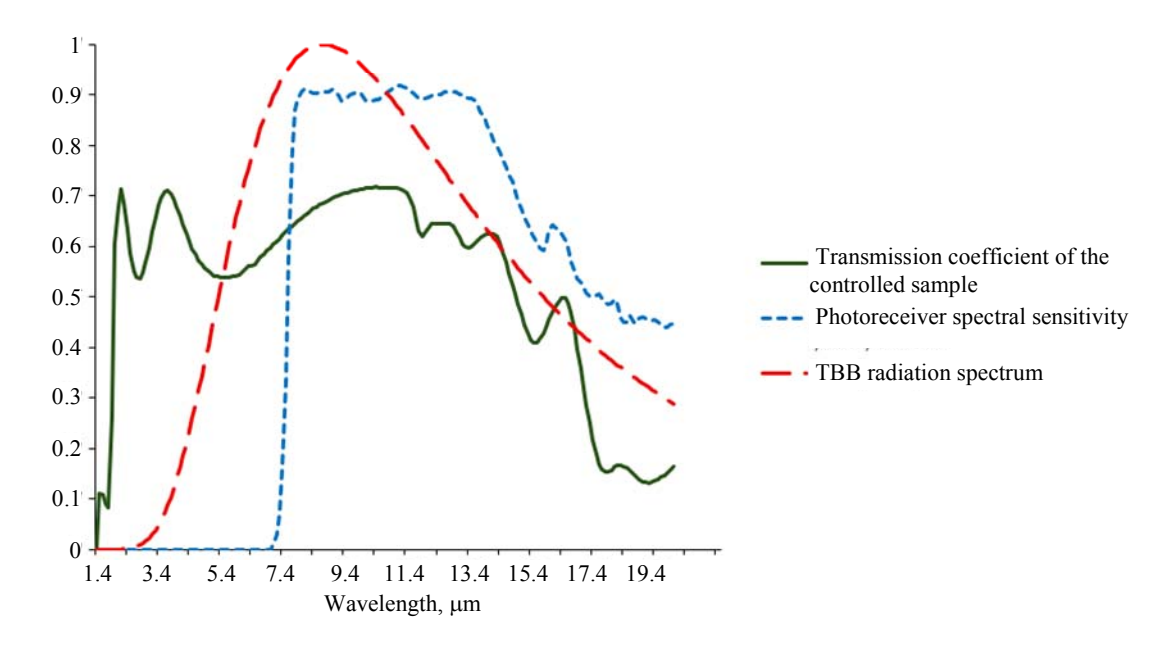


Fig. 7. Graphs of spectral characteristics

Conclusion

The developed method based on the measuring of the differential radiation flux change allows to control the integral transmission coefficient of optical components according to a sample-satellite under the conditions close to the actual ones.

Advantages of the developed method are the simplicity of its implementation, high resistance to the uniform background illuminations re-reflections. and developed method with minor modifications allows to use it for measurement of the integral coefficient internal of the transmittance (or absorption) of the material

and measurement of the integral lens transmittance coefficient by measuring the integral transmission coefficient of samplesatellite of all lenses included in the lens.

conducted analysis ofThe the metrological specifications of the method showed that the measurement error of the integral transmission coefficient temperature difference of more than 10 °C 3 % not exceed at confidential probability of 0.95. The conducted comparison of the measurement results according to the developed method and spectrum analysis showed the correspondence of measurement results, i.e. reliability of the developed method was proved.

The developed method was implemented in the measurement methodology certified by the FSBI "Main Scientific Metrology Center" of the Ministry of Defense of Russia.

REFERENCES

- 1. Vasilyeva V. I., Stoyanova O. F., Shkutina I. V. and Karpov S. I. Spectral Methods of Analysis. A Practical Guide: a tutorial / Ed. by Selemenev V. F., Semenov V. N. St. Petersburg, Lan, 2014. ISBN 978-5-8114-1638-7.
- 2. GOST 24604-81 Objectives. Method for Determining the Transmittance Coefficient. Moscow: USSR State Committee for Standards, 1981.

- 3. Filachev A. M., Taubkin I. I. and Trishenkov M. A. Solid-state photoelectronics. Photodiodes. Moscow, Fizmatkniga, 2011.
- 4. Drazhnikov B. N., Kozlov K. V., Kuznetsov P. A., Khamidullin K. A. and Deomidov A. D., Optical Journal **83** (9), 60–63 (2016).
- 5. Ledenev A. N. Physics. In 5 books. Book 4. Oscillations and Waves. Optics. Moscow, FIZMATLIT, 2005. ISBN 5-9221-0464-0.
- 6. Okrepilov V. V., Antokhina Yu. A., Ovodenko A. A. et al. Fundamentals of Metrology: A Textbook. 2nd ed., revised and enlarged. St. Petersburg, GUAP, 2019. ISBN 978-5-8088-1338-0
- 7. Gashnikov M. V. Methods of computer image processing / Ed by Soyfer V. A. 2nd ed., corrected. Moscow, FIZMATLIT, 2003. ISBN 5-9221-0270-2

About authors

Alexey Viktorovich Polessky, Doctor of Technical Sciences, Director for Research and Development, RD&P Center ORION, JSC (111538, Russia, Moscow, Kosinskaya st., 9). E-mail: polesskiyav@orion-ir.ru SPIN code 3992-4520, Author ID 571156

Natalia Alexandrovna Semenchenko, head of department, RD&P Center ORION, JSC (111538, Russia, Moscow, Kosinskaya st., 9). E-mail: nafara@mail.ru SPIN-code 8094-5126, Author ID 775858

Shamil Ilnurovich Zaripov, programmer engineer, RD&P Center ORION, JSC (111538, Russia, Moscow, Kosinskaya st., 9).

Denis Andreevich Mashoshin, second category engineer, RD&P Center ORION, JSC (111538, Russia, Moscow, Kosinskaya st., 9). E-mail: den_m01@mail.ru SPIN-code 7839-7538, Orcid 0009-0001-6339-8082

PHOTOELECTRONICS :

UDC 620.91:51.74 PACS: 84.60.Jt EDN: AUOORC

Model and calculation of the rate of generation and recombination of charge carriers for ZnO/CH₃NH₃PbI₃/NiO perovskite solar cell designs

© A. M. Karmokov¹, E. N. Kozyrev², A. Z. Agoev¹, O. A. Molokanov¹ and R. Yu. Karmokova^{1,*}

¹ Kabardino-Balkarian State University named after H. M. Berbekov, Nalchik, 360004 Russia * E-mail: karrit@mail.ru ² North Caucasus Mining-Metallurgical Institute (Technological University), Vladikavkaz, 362021 Russia

> Received 5.12.2024; revised 14.01.2025; accepted 11.08.2025 Scientific specialty code: 1.3.8.

A model is proposed for calculating the parameters of a perovskite solar cell of the ZnO/CH₃NH₃PbI₃/NiO structure with ITO and Ag contact layers, a zone diagram of the proposed structure was also constructed and its photoelectric parameters and energy efficiency were calculated. According to calculations, the quantum efficiency of the perovskite absorbing layer in the studied part of the solar radiation spectrum is on average about 90 %. It is shown that in the wavelength range from 0.38 µm to 0.76 µm, the absorption coefficient in perovskite is more than 2 times higher than the absorption in ITO and ZnO films. Profiles of the distribution of the rates of generation and recombination of electron-hole pairs in the functional layers of the structure have been constructed, from which it can be seen that the generation rate reaches a value of ~10²² cm⁻³·s⁻¹, which is several orders of magnitude higher than the capture rates of electrons and holes.

Keywords: perovskite; solar cell; zinc oxide; titanium oxide; charge carriers.

DOI: 10.51368/1996-0948-2025-4-24-29

Introduction

In recent years, the research has focused extensively on the development of new, low-cost perovskite solar cells, leading to the creation of mathematical models designed to predict and optimize their photoelectric properties. In numerical solar cell modeling, the rates of charge carrier generation and recombination are critical initial parameters. They determine the efficiency of photon-

induced charge carrier generation and determine the overall output characteristics of the solar cell. Reported generation efficiency coefficients vary significantly across studies. For example, references [1, 2] cite values ranging from 80 % to 100 %.

In this work, we evaluate the absorption coefficient, generation rates, and recombination rates of charge carriers within the thin layers of a new solar cell with an ITO/ZnO/CH₃NH₃PbI₃/NiO/Ag layers (ITO

is an electrically conductive layer of tin and indium oxides). The radiation falls perpendicular to the surface of the ITO element.

Study results

The radiation absorption coefficients, along with the rates of charge carrier generation and recombination, were assessed within the solar cell's primary active area [1–4].

This thin area comprises the ZnO. CH₃NH₃PbI₃ perovskite, and NiO layers, where these charge carrier dynamics primarily occur. The band diagram (Fig. 1) shows the energy level profiles across the constituent layers of the structure. The layer thicknesses are 100/400/100 nm, respectively. calculations were performed using MathCad and SCAPS-1D, a program widely used by researchers for modeling similar solar cell structures [5, 6].

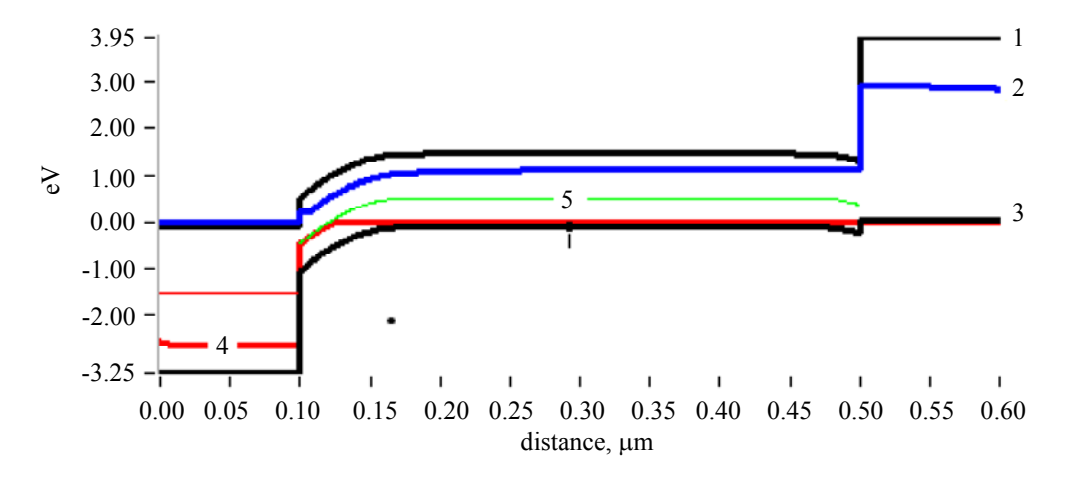


Fig. 1. Band diagram of the $ZnO/CH_3NH_3PBI_3/NiO$ structure: 1 - conduction band; 2 - Fermi level F_n in ZnO, $CH_3NH_3PbI_3$ layers; 3 - valence band; 4 - Fermi level F_p in NiO; 5 - Fermi level for intrinsic conductivity

Upon interaction of solar radiation with the functional layers of a solar cell, photons are absorbed, and their energy drives the formation and subsequent separation of excitons. Furthermore, as photons travel through a medium, the charge density diminishes due to absorption. The generation rate becomes a function of the depth x from the surface, as expressed by the equation [1]:

$$G(\lambda, x) = \int_0^{\lambda_0} \gamma(x) I(\lambda)(\alpha, x) e^{-\alpha(\lambda)x} d\lambda$$
 (1)

where λ is the wavelength, λ_0 is the absorption edge, $\gamma(\lambda)$ is the turnaround efficiency of the incoming photon into current, and $I(\lambda)$ is the effective density of the incident light, $\alpha(\lambda)$ is the absorption coefficient.

The curve representing the spectral range (from 380 to 760 nm) associated with the generation of charge carriers [7] is approximated by a polynomial, with a high reliability ($R^2 = 0.9851$).

$$I(\lambda) = -5.42 \times 10^{-10} \lambda^4 + 1.25 \times 10^{-6} \lambda^3 - -1.07 \times 10^{-3} \lambda^2 + 4.08 \times 10^{-1} \lambda - 56.2 \left[\text{W/(m}^2 \text{nm)} \right]^{(2)}$$

In the solar radiation spectrum, the peak value of the spectral intensity density is $1.5 \text{ W/(m}^2 \cdot \text{nm})$, occurring at a ~0.47 µm wavelength. For our calculations we used the maximum value of 1.5 from the AM1 spectrum [7]. The energy of a light quantum in the $\lambda = 0.38-0.76$ µm wavelength range varies from 3.35 eV to 1.63 eV. Thus, to create an electron-hole pair in the absorbing

layer of a solar cell, the band gap width shall be smaller than the minimum energy of a light quantum, which is 1.63 eV. The experimental values of the band gap in perovskites used in solar cells, as reported in the literature, vary and range from 1.45 to 1.70 eV.

Figure 2 shows the quantum efficiency of solar energy conversion into charge carriers as a wavelength function as we calculated. It aligns with the approximate equation we derived using the AM1 curve from [7] for the wavelength range $\lambda = 0.38-0.76 \ \mu m$.

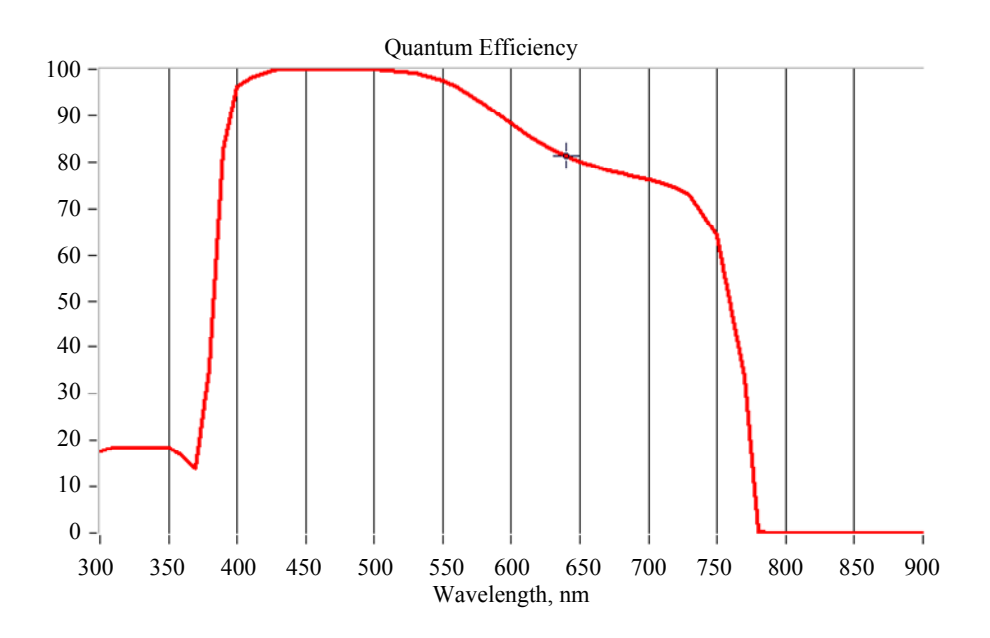


Fig. 2. The quantum efficiency of solar energy conversion into charge carriers as a wavelength function

As the figure shows, the quantum yield for perovskite closely matches the solar radiation intensity described by equation (2). When photon energies exceed the band gap width of the semiconductor by a factor of two or more, i.e. $E_g < 2hv$ (where h represents Planck's constant and v is the radiation frequency), the emission of charge carriers may increase by two or more times [8, 9]. For the most promising CH₃NH₃PbI₃ perovskite, widely used in research, $E_g = 1.55$ eV. Thus, to determine the efficiency of converting an incident photon into current $\gamma(\lambda)$ in equation (1) for the perovskite we used, it can be assumed to be equal to one, given that for perovskite, $E_g < hv$, and in the IR-area, $E_{g} < 2h\nu$.

The absorption coefficient $\alpha(\lambda)$ is influenced by the incident light energy quantum on the surface and the width of the semiconductor material's band gap, and is represented by the following equation [6, 8]:

$$\alpha(\lambda) = B_{\alpha} \sqrt{\frac{hc}{\lambda} - E_{g}}$$
(3)

where B_{α} is a non-contiguous constant defined as $10^5 \, \text{cm}^{-1} \cdot \text{eV}^{-0.5}$, and hc/λ represents the photon energy. Figure 3 shows the dependences between the absorption coefficient and radiation wavelength in the range from $\lambda = 0.38-0.76 \, \mu \text{m}$ for the functional layers of the element, calculated using (3).

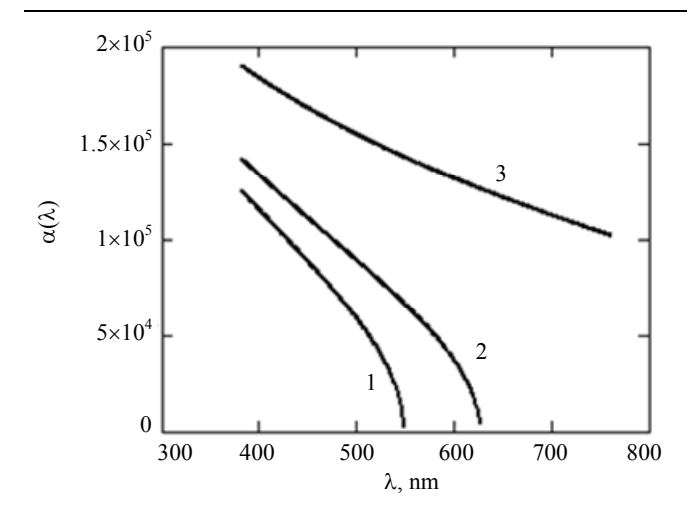


Fig. 3. The absorption coefficient dependencies on the radiation wavelength in the range $\lambda = 0.38$ to 0.76 μ m for films: 1 - ITO; 2 - ZnO and 3 - perovskite CH₃NH₃PbI₃

As shown in the figure, the ITO and ZnO absorption coefficients are several times lower than those of perovskite. Their values $\alpha(\lambda)$ exhibit a sharp decline as the radiation wavelength increases, becoming negligible at wavelengths exceeding 550 nm for ITO and 630 nm for ZnO, respectively. The absorption coefficient of perovskite varies by ~1.5 times within the $\lambda = 0.38-0.76 \,\mu\text{m}$ spectrum range and exceeds that of the oxides by more than 2 times. In contrast to zinc and nickel oxides, the perovskite layer absorbs radiation across the entire spectral range $\lambda = 0.38-0.76 \mu m$. Thus, the solar cell we propose, similar to the one in [4], is designed to convert infrared radiation into electrical energy.

The recombination of free charge carriers in materials with a low defects concentration and mobility is frequently characterized as direct recombination. Based on Langevin's theory, the charge recombination rate is directly proportional to the electrons and holes densities:

$$R = r\left(np - n_i^2\right),\tag{4}$$

where r is the recombination coefficient, and $n_i = N_c \times \exp(-E_{gap}/2kT)$ is the intrinsic charge carriers concentration, which is significantly lower in perovskite materials compared to the charge carriers generated by photons. Recombination may also take place through traps and defects, a process that may be modeled using the Shockley-Reed-Hall method [3, 9]:

$$R = \frac{np - n_i^2}{\tau_p(n + n_1) + \tau_n(p + p_1)},$$
 (5)

where τ_p and τ_n are the holes and electrons lifetimes, respectively, while n_1 and p_1 are the electrons and holes concentrations at the point where the quasi-Fermi level aligns with the trap energy. While n_1 and p_1 depend on the energy levels of the E_d recombination centers:

$$n_1 = N_c \exp\left[-\left(E_C - E_d\right)/\left(kT\right)\right],$$

$$p_1 = N_{v} \exp \left[\left(E_V - E_d \right) / \left(kT \right) \right].$$

Figure 4 shows the distribution profiles of the generation and recombination rates of charge carriers within the active layers of the ZnO/CH₃NH₃PbI₃/NiO solar cell structure, with the layer thicknesses of: ZnO – 100 nm, perovskite – 850 nm and NiO – 100 nm.

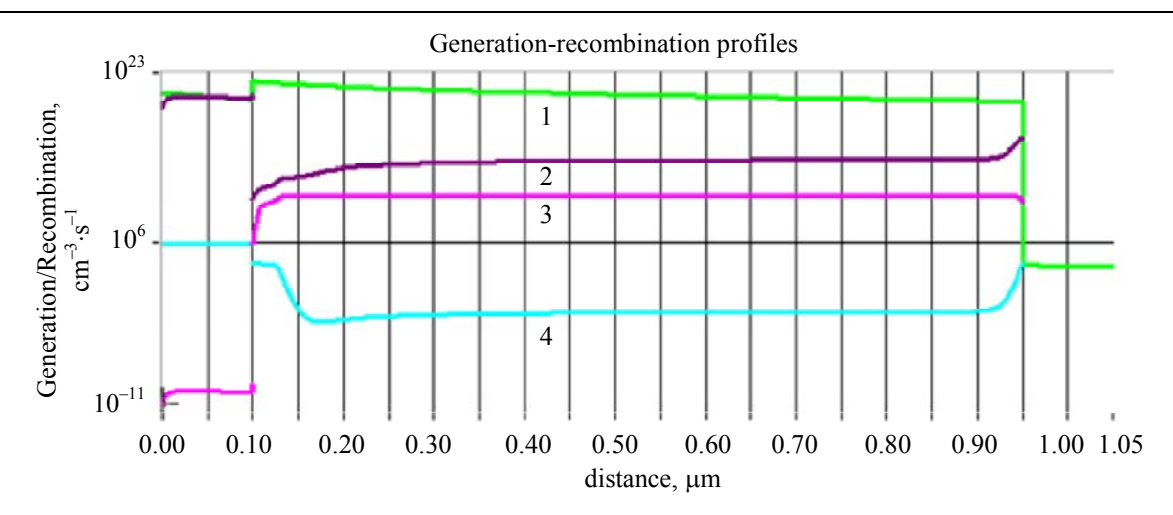


Fig. 4. Distribution profiles of generation and recombination rates in $ZnO/CH_3NH_3PbI_3/NiO$ layers: 1 – electron-hole pairs generation; 2 – hole capture; 3 – hole emission; 4 – electron emission

The figure shows that the generation rate of electron-hole pairs reaches its peak at $\sim 10^{22}~\text{cm}^{-3}\text{·s}^{-1}$, which is greater than the electron and hole capture rates.

Conclusion

Calculations conducted using the proposed model demonstrate that the perovskite layer exhibits high quantum efficiency across the entire examined range of the solar radiation spectrum. The band diagram of the proposed structure ensures charge carriers efficient generation. perovskite layer absorption coefficient is significantly greater than that of the zinc and nickel oxide layers. The electron-hole pairs generation rate in the structure is high, exceeding $10^{22} \text{ cm}^{-3} \text{c}^{-1}$.

The work was carried out with the support of the Russian Science Foundation, project (Grant project No. 23-13-20012).

REFERENCES

- 1. Zhou Y. and Gray-Weale A., Physical Chemistry Chemical Physics **18** (6), 4476–4486 (2016).
- 2. Ullah S., Gulnaz A. and Wang G., Journal of Applied Mathematics and Physics **12** (3), (2024). doi: 10.4236/jamp.2024.123061
- 3. Saenko A. V., Malyukov S. P. and Rozhko A. A., Applied Physics, No. 1, 19–27 (2022) [in Russian].
- 4. Takashi Minemoto, Yu Kawano and Takahito Nishimura, Jakapan Chantana, Optical Materials **92**, 60–66 (2019).
- 5. Burgelman M., Nollet P. and Degrave S., Thin Solid Films **361–362**, 527–532 (2000).
- 6. Kapim Kenfack A. D., Thantsha N. M. and Msimanga M., Solar **3** (3), 458–472 (2023). doi: 103390/solar3030025
- 7. Handbook of geophysics and outer space / ed. Valley S. L. and McGraw-Hill, New York, 1965.
- 8. Akmanov A. G. and Shakirov B. G. Fundamentals of quantum and optoelectronic devices. Study guide. Ufa: RIO BashSU, 2003, p. 129 [in Russian].
- 9. Pikhtin A. N. Optical and quantum electronics. Moscow, Higher School, 2001 [in Russian].

About authors

Akhmed Matsevich Karmokov, Doctor of Physical and Mathematical Sciences, Professor, Kabardino-Balkarian State University named after H. M. Berbekov (360004, Russia, Nalchik, 173, Chernyshevskogo st.). E-mail: karmokov@kbsu.ru SPIN-code 5445-9389, Author ID 248531

Evgeniy Nikolaevich Kozyrev, Doctor of Technical Sciences, Professor, North Caucasus Mining-Metallurgical Institute (Technological University) (362021, Russia, Vladikavkaz, 44, Nikolaeva st.). E-mail: kozyrev@skgmi-gtu.ru RSCI SPIN code 9131-1691, Author ID 202347

Artur Zalimkhanovich Agoev, student (master's degree, 2nd year of study), Kabardino-Balkarian State University named after H. M. Berbekov (360004, Russia, Nalchik, 173, Chernyshevskogo st.). SPIN code 6458-6420, Author ID 1266717

Oleg Artemovich Molokanov, Candidate of Technical Sciences, scientific supervisor of the department, Kabardino-Balkarian State University named after H. M. Berbekov (360004, Russia, Nalchik, 173, Chernyshevskogo st.). E-mail: molokanov@kbsu.ru SPIN-code 6057-8764, Author ID 110079

Rita Yurievna Karmokova, Candidate of Physical and Mathematical Sciences, Senior Lecturer, Kabardino-Balkarian State University named after H. M. Berbekov (360004, Russia, Nalchik, 173, Chernyshevskogo st.). E-mail: karrit@mail.ru SPIN-code 4770-5532, Author ID 719705

=PLASMA PHYSICS AND PLASMA METHODS =

UDC 532.5, 537.39 PACS: 68.03.Hj

EDN: VTHMIB

Electric field strength measurements in transformer oil using microdroplets of water

© V. A. Panov*, A. S. Saveliev and Yu. M. Kulikov

Joint Institute for High Temperatures of Russian Academy of Sciences, Moscow, 125412 Russia

* E-mail: panovvladislav@gmail.com

Received 24.03.2025; revised 11.04.2025; accepted 11.08.2025 Scientific specialty code: 1.3.9

Experimental determination of the pulsed electric field strength in a liquid dielectric can be difficult when it is necessary to minimize the disturbance introduced by the measurement. The optical method based on the Kerr effect is applicable at sufficiently high strengths. An alternative solution can be water microdroplets introduced into the gap, the fragmentation of which in the electric field is determined by its amplitude and occurs at an electric capillary number $Ca_E \geq 0.2$. Experimental and theoretical studies for droplets of the same size have been conducted, which have shown the potential applicability of this method. The influence of the depth of field of the optical system and the initial charge of the droplets on the accuracy of measurements is discussed.

Keywords: electric field; intensity; measurement; microdroplets; water; electric capillary number.

DOI: 10.51368/1996-0948-2025-4-30-36

Introduction

Until Taylor's definitive study [1], the widely held belief was that liquid drops submerged in an immiscible liquid would act as ideal dielectrics, and that exposure to an electric field always resulted in an elongated deformation (lengthening along the direction of the electric field) of the surface [1]. This is known as the electrohydrostatic model, where electrostatic forces act only normal to the interphase boundary. Later studies [2] revealed that not all dielectric liquids elongate the electric field. Contrary the electrohydrostatic model, some exhibit flattened deformation (elongation perpendicular to the field). Based on these experiments, Taylor developed a model for low-conductivity dielectrics [3, 4]. He proposed that even a small amount of conductivity in a liquid allows a minor electric current to flow, leading to the accumulation of free charge at the liquid-liquid boundary.

In a low-conductivity dielectric, the interaction of free charge with the electric field generates electric forces tangential to the boundary, in addition to the normal stresses. Since these tangential forces shall be balanced in a stationary state, concluded that a vortex hydrodynamic flow exists. which confirmed was later experimentally. Taylor's theory accurately predicts the small deformation of emulsion drops under Stokes flow. Subsequent experimental and theoretical studies [5] of drop behavior in constant and alternating electric fields revealed that Taylor's theory generally underestimates the deformation magnitude, although it accurately predicts the deformation shape observed in experiments. Subsequent publications [6] refined the Taylor model, enabling the calculation of drop deformation up to the second-order approximation.

The studies identified several characteristics that determine the drop's evolution. For a drop of radius a subjected to an unperturbed external electric field of strength E, the characteristic velocity U is defined as: $U = \varepsilon_0 \varepsilon_{\text{out}} E^2 a / \mu_{\text{out}}$. The subscripts "in" and "out" denote the liquid properties within the drop and the surrounding medium, respectively. ε represents the dielectric permeability, and µ represents the dynamic viscosity. The dynamics of drop deformation are governed by dimensionless parameters derived from the properties of the internal and external fluids. These include conductivity ratio $R = \sigma_{in}/\sigma_{out}$, the dielectric capacitivity ratio $S = \varepsilon_{in}/\varepsilon_{out}$, and the viscosity Non-dimensionalization ratio $M = \mu_{in}/\mu_{out}$. yields several other dimensionless parameters, including the flow Reynolds number Re, the electric Reynolds number Re_E, and the electric capillary number Ca_E. The Re number represents the ratio of inertial forces to viscous forces and is defined as $Re = \rho_{out}aU/\mu_{out}$, where ρ_{out} is the density of the external fluid. The Taylor model is applicable only to the flows with a low Reynolds number $\text{Re} \leq O(1)$ and, consequently, small drop sizes. to The Ohnesorge number, a dimensionless parameter, determines transient deformation modes (e.g., monotonic and oscillatory). It is defined as the ratio of viscous forces to the square root of the product of inertial and surface tension forces: Oh = $\mu_{in}/(\rho_{inv}a)^{0.5}$, where γ is the coefficient of surface tension between the two liquids. The electric capillary

number is the ratio of the electrical stress εE^2 to the capillary voltage γ/a . It determines the drop's deformation modes, distinguishing between stable and unstable deformation: $Ca_E = \mu_{out}U/\gamma = \varepsilon_0 \varepsilon_{out} E^2 a/\gamma$. The electric Reynolds number is defined as the ratio of the characteristic relaxation time $t_c = \varepsilon_0 \varepsilon_{out} / \sigma_{out}$ to the charge-transport time by the flow $t_h = \mu_{out}/(\epsilon_0 \epsilon_{out} E^2)$. A small electric Reynolds number ReE indicates that convection effects are negligible. Depending on the properties of the medium, ReE is defined $Re_E = t_c/t_h = \varepsilon_0^2 \varepsilon_2^2 E^2/\mu_2 \sigma_2.$ The number Sa, defined as the ratio of the electric Reynolds number to the electric capillary number, is another key dimensionless parameter that controls transitions between different drop breakup modes. Sa = Re_E/Ca_E. For the current studies, the aforementioned parameters fall within the following ranges: $Re = (0.01-0.1), Re_E = (10^4-10^5), Oh = 0.035,$ $Ca_F = (0.05-1).$

When the capillary number falls below a critical value, the conductive drop stabilizes and electrical flows are absent within the drop and its environment. When the capillary number exceeds the critical value, the voltage on the drop increases until surface tension is insufficient to balance it, leading to drop rupture. Taylor, employing the spheroidal drop model, calculated the critical capillary number roughly 0.2 [7]. Several as 9], and experimental [8], analytical [6, numerical [10–14] studies indicate the critical CaE is approximately 0.20 ± 0.02 .

The objective of this study is to explore the possibility of using water microdrops to measure the strength of the electric field at specific points within the discharge gap in transformer oil.

Experimental unit

Figure 1 shows a schematic of the experimental arrangement used to investigate the deformation and breakage of polar liquid drops (water) when subjected to an electric

field. Two immiscible liquids, water (W) at the bottom and transformer oil (O) at the top, are introduced into a tank (T) designed as a right parallelepiped with transparent walls. A rounded electrode E1 is submerged in water, which has an electrical conductivity of 300 μS/cm, and is grounded via a measuring resistor R_s (25 Ohm). In contrast, a pointed electrode E2 is placed in the oil and is supplied with voltage from a storage capacitor C using a semiconductor highvoltage switch S. This capacitor is charged through a ballast resistor R_b (1 MOhm) from a high-voltage positive voltage source, reaching a voltage of +20 kV. To restrict the current in the electrical circuit, a resistor R₁ with a resistance of 5 kOhm has been added to the circuit. When a low-voltage pulse is sent from the digital generator G to the control input of the switch S, it activates the switch, delivering high voltage to electrode E2. In the absence of a synchronous pulse, the switch links the E2 electrode to the ground via a 50 Ohm current limiting resistor $R_{\rm g}$. This prevents any charge from building up in the high voltage supply area until the experiment starts. The semiconductor switch characterized by a voltage rise time of approximately 0.1 µs, as well as a voltage fall time of about 0.1 µs.

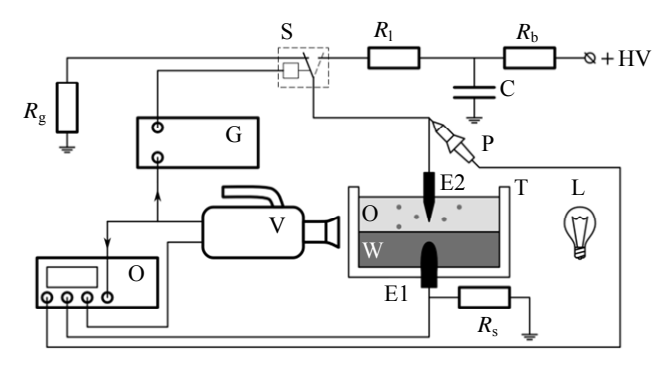


Fig. 1. Experimental setup diagram: O-oscillograph, V-camera, T-discharge cell, E1, E2-pair of electrodes, L-light source, G-pulse generator, P-voltage probe, HV-high-voltage power source, S-semiconductor high-voltage switch, $R_s-current$ shunt, $R_g-protective$ resistance of switch, S, $R_l-current-limiting$ resistance, $R_b-ballast$ resistance, C-shock capacitance

To create water drops in oil, an initial phase is performed with a duration of high voltage applied to electrode E2 that allows for the formation of an electric discharge between the electrodes as outlined in [15]. A rapidly expanding zone of hot gas (plasma) is provided between the electrodes, causing swift deformation and interface disruption between the liquids, resulting in the formation of drops of one liquid within the other (the dots in the figure represent droplets of water in oil). Since the liquids' densities are similar and their viscosity is relatively high, the suspended droplets of one liquid remain for a considerable duration. The characteristic time of their movement is significantly longer than the duration of the applied stress. This allows for the next experiment to be conducted within a few tens of seconds after the drops formation.

To observe the droplet deformation and destruction, a high-speed digital video camera (V) and background illumination of the tank (T) are employed, using an incandescent lamp (L). Additionally, an oscilloscope (O), a 1:1000 high-voltage probe (P), and a current shunt (R_s) are used to measure the electrical parameters. The REC READY signal, which indicates the filming start, is transmitted from the video camera (V) to the oscilloscope to trigger its operation and to the generator input (G), which activates the switch (S) after a predetermined time delay to synchronize visualization and measurement in time. Additionally, a video camera signal F SYNC is sent to one of the oscilloscope channels, which corresponds to the exposure durations of the film frames. The duration of the high voltage applied to electrode E2 is 0.4 ms, which is shorter than the time necessary for the discharge to establish between the electrodes.

Mathematical model

A detailed explanation of the problem for modeling is provided in [16]. We will

only outline the key geometric parameters of the model. The electric field distribution is calculated using a cylindrical coordinate system, with the axis aligned parallel to the electrode system's axis. The calculation area dimension in the radial direction is 40 mm. The distance from the tip of the electrode immersed in the oil to the interphase boundary is 3 mm, the total thickness of the oil layer is 15 mm, the distance from the pin electrode surface to the interphase boundary is also 3 mm. The diameter of the cylindrical section of the pointed electrode is 1 mm, that of the cylindrical electrode – 1.8 mm. The radius of the needle tip rounding is 70 µm. The parameters used for water and oil in the calculations were as follows: density 1000 and 980 kg/m³, dynamic viscosity 8.9×10⁻⁴ and 2.36×10⁻², dielectric capacitivity 80 and 2, electrical conductivity 300 μS/cm 1 pS/cm, surface tension between water and oil 24.7 mN/m.

Findings and discussion

Figure 2 shows photographs of the discharge gap captured at an exposure of 17 μ s, taken at 0 μ s and 400 μ s, with the observed drops highlighted. The drops that break down into smaller individual drops are highlighted red (11 pcs.), those with slight deformation but no destruction is highlighted blue (19 pcs.), and the drops without any visible deformation are highlighted pink (7 pcs.). The drops highlighted red share a common characteristic: they are situated close to either a high-voltage electrode or the interface, where the potential is similar to that of the probe electrode due to the relatively high water conductivity. The pink drops are located at the edges of the observation area, whereas the blue drops are positioned in an intermediate position. Some drops exhibit a clearly defined boundary, indicating location in the focusing plane of the optical system, which allows accurate size measurement. The images of the other marked drops display

a blurred boundary. These drops are located outside the focusing plane, and their size may only be measured approximately. The average diameter of selected drops is about 50 μ m.

The capillary electric number Ca_E was calculated for all identified drops (Fig. 3). The results are presented into the three abovementioned groups, with points arranged in order of increasing Ca_E . Individual Ca_E values do not always meet the fragmentation criterion of $Ca_E \ge 0.2$. Some drops do not undergo fragmentation at $Ca_E \ge 0.2$, while others may fragment at $Ca_E < 0.2$.

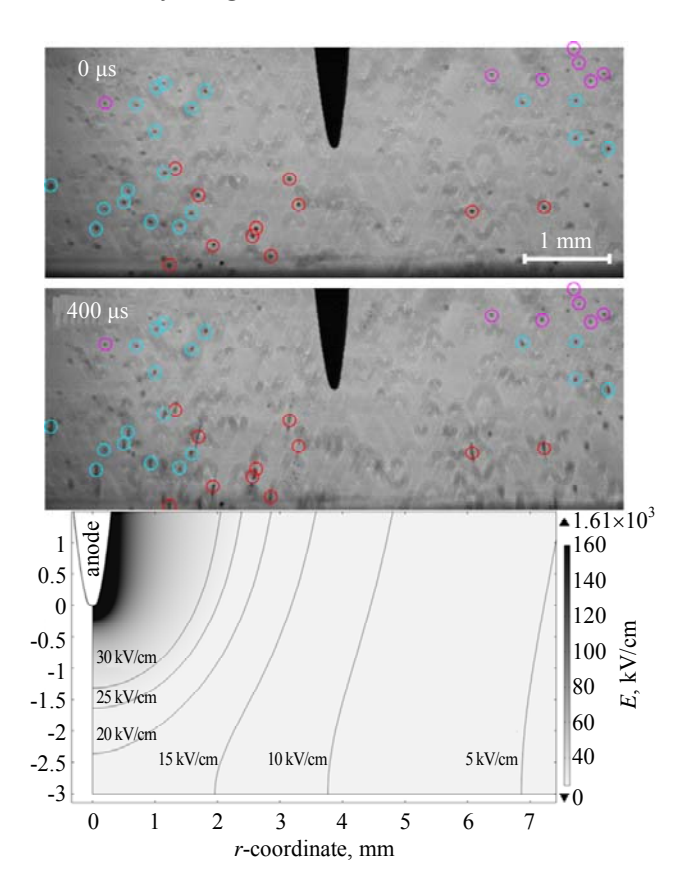


Fig. 2. Deformation and streaming of water droplets suspended in oil under the action of the voltage pulse with the amplitude of 20 kV and a duration of 400 µs (time moments 0 and 400 µs). Red circles indicate drops that have undergone fragmentation, blue circles indicate drops with significant deformation, and pink circles indicate drops that do not show noticeable deformation

The horizontal bar in each group represents the mean Ca_E value: 0.15, 0.17 and 0.30. The average values align with literature data concerning the critical value at values

below 0.2 (i.e. 0.15 and 0.17), only deformation or no response of the drop to the field's action is noted, whereas at a 0.30 value fragmentation of the droplets is observed.

The probable explanation for the inconsistency between the deformation of certain drops and the calculated CaE value is related to the following factors. The microscope used as a camera lens

possesses a considerable depth of field at the specified magnification (Fig. 4). The relationship between d/d_0 and the distance between the drop and the focusing plane, L, suggests that the drop apparent diameter, d, will exhibit only minor changes compared to its actual diameter, d_0 , when the drop's position deviates from the focusing plane by L=1 mm.

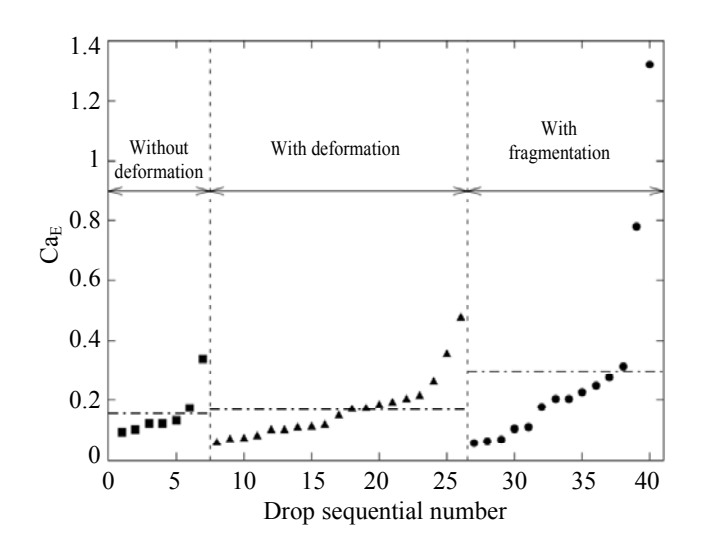


Fig. 3. The capillary electric number CaE for the droplets shown in Figure 2. The vertical dotted lines separate the groups of drops categorized as "without deformation", "with deformation", and "with fragmentation". The horizontal dash-dotted lines represent the average Ca_E value for each group

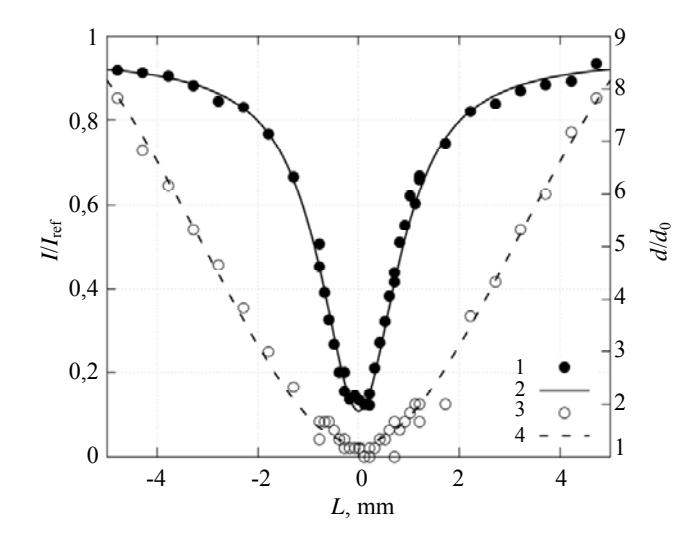


Fig. 4. Experimental dependences of the relative intensity of droplet images (I/I_{ref}, "1") and relative visible diameter (d/d₀, "3"), as well as corresponding approximations by the Lorentz function ("2" and "4")

Although relatively low deviation L can drastically alter the field strength at the drop's visible center, used to calculate Ca_E . This is because the field is highly inhomogeneous, especially near the tip. This explains why drops deform without fragmenting when their calculated number is > 0.2. A second factor is

the electric charge of the drops, which they can acquire if they form at the interface within an electric field. To quantify the influence of surface charge on the droplet fragmentation criterion, we use the electric capillary number Ca_E. To accomplish this, we examine the disintegration of a charged drop

in the absence of an external electric field. Instability and subsequent fragmentation occur when $f = E_c/(2E_s) \ge 1$, where E_c and E_s represent the electrostatic energy and surface energy of the drop, respectively. These energies can be expressed as $E_c = Q^2/(8\pi\epsilon_0 a)$, $E_s = 4\pi \gamma a^2$. Substituting the expressions into expression for f, we obtain $f = Q^2/(64\pi^2 \epsilon_0 a^4) \ge \gamma/a$. Considering a charged drop subjected to an external electric field, we combine the previously derived condition with the criterion $Ca_E \ge 0.2$:

$$Q^{2}/(64\pi^{2}\varepsilon_{0}a^{4}) + 5\varepsilon_{0}\varepsilon_{\text{oil}}E^{2} \ge \gamma/a. \tag{1}$$

To practically apply the derived expression, we will estimate the magnitude of the drop charge formed as a result of separation from a water-oil interface. We assume that the surface charge density of the drop prior to separation is equal to that of the interface from which it separates. The surface charge density can be estimated using the expression $\sigma = \varepsilon_0 E_n$, where E_n is the electric field strength on the axis of the electrodes near the surface, obtained from numerical modeling (Fig. 2). Expression (1) can then be expressed as:

$$1/\left(4\varepsilon_{0}E_{n}^{2}\right)+5\varepsilon_{0}\varepsilon_{oil}E^{2} \geq \gamma/a. \tag{2}$$

This correction accounts for an additional 10% to 20% in the capillary electric number breakup criterion, thereby explaining the fragmentation of drops even when their calculated $Ca_E < 0.2$.

Conclusions

As the electric field strength increases, a conductive drop deforms into the shape of a spheroid, whose major axis aligns with the electric field vector. This deformation can be stable or unstable. The deformation is determined by the value of the electric

capillary number. For drops with a capillary electric number $Ca_E < 0.2$, deformation is stable. Exceeding the CaE threshold results in unstable drop deformation. The subsequent disintegration is further influenced by the conductivity ratio, dielectric capacitivity, dynamic viscosity, and the Saville number, as described above.

The experimental results indicate that the average electrical capillary numbers for drops exhibiting no noticeable, or unstable deformation correlate to the critical value of 0.2 reported in the literature. This observation provides a practical means for determining the magnitude and distribution of the electric voltage in the interelectrode gap, assuming known drop diameters.

REFERENCES

- 1. O'Konski C. T. and Thacher H. C., The Journal of Physical Chemistry **57** (9), 955–958 (1953).
- 2. Allan R. and Mason S., Proceedings of the Royal Society of London. Series A. Mathematical and Physical

Sciences 267 (1328), 62–76 (1962).

- 3. Taylor G. I., Proceedings of the Royal Society of London. Series A. Mathematical and Physical Sciences **291** (1425), 159–166 (1966).
- 4. Melcher J. R. and Taylor G. I., Annual Review of Fluid Mechanics **1** (1), 111–146 (1969).
- 5. Torza S., Cox R. G. and Mason S. G., Philosophical Transactions of the Royal Society of London. Series A. Mathematical and Physical Sciences **269** (1198), 295–319 (1971).
- 6. Ajayi O. O., Proceedings of the Royal Society of London. A. Mathematical and Physical Sciences **364** (1719), 499–507 (1978).
- 7. Wilson C. T. R. and Taylor G. I., Mathematical Proceedings of the Cambridge Philosophical Society **22** (5), 728–730 (1925).
- 8. Ha J.-W. and Yang S.-M., Journal of Fluid Mechanics **405**, 131–156 (2000).
- 9. Taylor G., Proceedings of the Royal Society of London. Series A. Mathematical and Physical Sciences **280** (1382), 383–397 (1964).
- 10. Miksis M. J., The Physics of Fluids **24** (11), 1967–1972 (1981).
- 11. Sherwood J. D., Journal of Fluid Mechanics **188**, 133–146 (1988).

- 12. Basaran O. A. and Scriven L. E., Physics of Fluids A: Fluid Dynamics 1 (5), 799–809 (1989).
- 13. Feng J. Q. and Scott T. C., Journal of Fluid Mechanics **311** (1), 289 (1996).
- 14. Dubash N. and Mestel A. J., Physics of Fluids **19** (7), (2007).
- 15. Panov V. A., Kulikov Yu. M., Pecherkin V. Ya., Vasilyak L. M. and Saveliev A. S., Applied Physics, № 6, 5–10 (2023) [in Russian].
- 16. Panov V. A., Saveliev A. S. and Kulikov Yu. M., Applied Physics, № 2, 5–11 (2025) [in Russian].

About authors

Vladislav Aleksandrovich Panov, Candidate of Physical and Mathematical Sciences, senior research scientist, Joint Institute for High Temperatures of Russian Academy of Sciences (125412, Russia, Moscow, 13, Izhorskaya st., bldg. 2). E-mail: panovvladislav@gmail.com SPIN code 5821-2776, Author ID 755538

Andrey Sergeevich Saveliev, Candidate of Physical and Mathematical Sciences, senior research scientist, Joint Institute for High Temperatures of Russian Academy of Sciences (125412, Russia, Moscow, 13, Izhorskaya st., bldg. 2). E-mail: fisteh@mail.ru SPIN code 6888-7369, Author ID 866343

Yuri Matveevich Kulikov, Candidate of Physical and Mathematical Sciences, senior research scientist Joint Institute for High Temperatures of Russian Academy of Sciences (125412, Russia, Moscow, 13, Izhorskaya st., bldg. 2). E-mail: kulikov-yurii@yandex.ru SPIN code 7719-8459, Author ID 1130937

PLASMA PHYSICS AND PLASMA METHODS

UDC 537.525 PACS: 52.27.Lw; 37.10.Ty.

EDN: BFPHPG

Accumulation of ions in an electrostatic plasma trap within a cloud of charged microparticles in an electric discharge

© D. N. Polyakov^{1,*}, V. V. Shumova^{1,2} and L. M. Vasilyak¹

¹ Joint Institute for High Temperatures of Russian Academy of Sciences, Moscow, 125412 Russia * E-mail: cryolab@ihed.ras.ru

Received 9.04.2025; revised 30.04.2025; accepted 11.08.2025 Scientific specialty code: 1.3.9

A novel plasma trap using an electrostatic method to trap positively charged ions within a cloud of negatively charged microparticles in the plasma of a positive column of a glow discharge (complex plasma) is considered. Such a trap may be of interest for plasma technologies at low and cryogenic temperatures, as it is characterised by a high concentration of trapped ions and generates less heat than plasma without microparticles. Calculation of the parameters of the complex plasma was carried out on the basis of experimental data by means of the liquid model. The efficiency of ion accumulation in the plasma trap within the microparticle cloud was evaluated. It is found that the intensity of the accumulation of ions in the cloud of microparticles can be higher or lower than the intensity of their birth in the plasma of a discharge free of microparticles. In the first case, the complex plasma is in the efficient ion retention regime, where the trap is an ion concentrator, and, in the inefficient retention regime in the second case. Based on the determination of the values of the relative overheating coefficient, it is shown that complex plasma is a more effective tool for producing the required concentration of cold ions than the plasma without microparticles.

Keywords: complex plasma; direct current discharge; charged microparticle cloud; ion trap efficiency.

DOI: 10.51368/1996-0948-2025-4-37-44

Introduction

Penning [1] and Paul [2] electrodynamic traps are used to address various physical problems related to maintaining the desired concentration of ions in a specific region of space. Charged particles trapped in electrodynamic systems create strongly coupled Coulomb systems [3]. To decrease

the kinetic energy of ions, they are cooled to extremely low temperatures [4], allowing for study their interaction potentials, transfer processes, thermalization, and collective phenomena. In this context, Paul and Penning traps enable the confinement and investigation of individual frozen ion atoms [5] and ion clouds, which manifest as atomicion Coulomb clusters and crystals [6, 7].

² Semenov Federal Research Center for Chemical Physics, Russian Academy of Sciences, Moscow, 119991 Russia

In plasma chemistry, scientists aim to regulate chemical reactions by cooling the area where these reactions occur [8]. Moreover, reactions occurring at low and temperatures [9] enable ultra-low the production of new phase states via plasmachemical synthesis that cannot be achieved under different conditions [10]. This drives researchers' interest in exploring applications related to the generation of plasma chemically active medium at cryogenic temperatures [11]. The electrodynamic traps applied in the scope of plasma chemistry are considered not effective due to the limited number of $N_i \sim 10^4$ retained ions and the concentration $n_i < 10^8 \, \text{cm}^{-3}$ restrictions of Moreover, the complexity of manufacturing and the high cost of these traps further complicate their use. In the applied plasma chemistry, achieving a high concentration of ions within a large reaction volume is crucial. To increase the concentration of positive ions, a neutralizing background of electrons is required, which may be achieved in lowtemperature gas discharge plasma. Thus, a direct current glow discharge in neon, where n_i can reach $\approx 10^{11} \, \text{cm}^{-3}$ in the positive column of the discharge [13], may be used as a basic source, due to its possibility to provide a high concentration of ions in a large plasma volume (~1000 cm³). However, this method of ion production is poorly suitable for application under cryogenic cooling conditions due to the significant heat generation $\lceil 14 \rceil$. The most promising technique for capturing and generating ions, which overcomes most of the disadvantages, is implemented in dusty (complex) plasma [15]. Dusty plasma of electrical discharges in gases allows to form traps composed of clouds of charged microparticles which properties are based on strong electrostatic interactions, allowing for the accumulation localization and of ions [16, 17]. Such clouds may create Coulomb crystals and clusters [15], resembling the behavior of ions in cold Paul traps [6, 7].

Dusty plasma in an electric discharge may be obtained in large volumes. This type of dusty plasma was generated in a glow discharge in a tube with a radius of 40 cm and a length of 80 cm in argon [18]. Currently, researchers also study gas discharge of dusty plasma under cryogenic temperature conditions, as it may accumulate and sustain cold ions with a specified concentration [10, 19, 20].

In this study, the accumulation of positive ions in an electrostatic trap created by a cloud of charged microparticles, along with a plasma from a direct current electric discharge in neon, was studied using numerical methods, and the trap's effectiveness was evaluated.

Model for calculating complex plasma parameters

The parameters of the dusty plasma were calculated using the diffusion-drift model for the positive column of a glow discharge in neon containing microparticles [14, 16, 17]. The model met the experimental conditions, as the mean free paths of ions and electrons were significantly smaller than the discharge radius. The experiments were conducted in a vertically oriented glass tube with a length of L = 40 cm and an internal radius of R = 0.825 cm, within an extended DC discharge (where $R \ll L$). calculations were performed using typical average parameters for clouds composed of microparticles with a diameter of 2.55 µm, with neon current and pressure values that correspond to the experimental conditions.

In the proposed model of the dusty plasma, the material balance equations account for the processes of generation and death of electrons, ions, and metastable neon atoms with an energy of 16.6 eV, within the plasma volume and on the surfaces of the microparticles. The list of collision processes considered in the model is given in [14]. The drift and diffusion of electrons, ions, and

metastable atoms were analyzed in the E_z axial (longitudinal) electric field, as well as in the E_r self-consistent radial electric field. The electron average energy, transport coefficients, and rate constants for excitation and ionization reactions involving electrons were calculated using the BOLSIG+ software package [21] in conjunction with the SIGLO database [22]. The microparticles' charge is determined while considering ion-atom interactions within the weak-collision plasma approximation [23]. The flux of excited atoms onto the microparticles is calculated using the gas-kinetic approximation, while quenching is assessed under the assumption of complete energy accommodation. It was assumed that there is no emission of electrons photoelectrons from the surfaces of the dust particles, the distribution of microparticles within the cloud is uniform, and it decreases exponentially at the cloud's boundary. It was assumed that the I total current passing through the discharge cross section remained constant during variations concentration of microparticles n_p , as the experimental studies were conducted under conditions of a constant current value.

Results and discussion

Figure 1 shows a schematic representation of the plasma region for which the calculations were conducted. The left side of the figure shows the plasma composition along with the voltage drop measurement circuit employed in the experiment, while the right side shows the radial distributions of the electric field, as well as the concentrations of ions and electrons. The upper fragment corresponds to plasma without microparticles, and the lower one to plasma with a cloud of microparticles with $n_p = 4 \times 10^5 \text{ cm}^{-3}$. In a plasma free of microparticles (free discharge), the primary plasma losses are attributed to the loss of electrons (indicated by the blue background on the left side of the figure) and

ions (the red dots), which occur due to their radial diffusion and drift towards the walls of the discharge device. The drift of charged particles occurs in the E_r radial electric field. microparticles, the profiles Without electrons $n_e(r, 0)$ and ions $n_i(r, 0)$ similar to the Bessel distribution $J_0(2,4r/R)$. The maximum ionization occurs along the discharge axis. The ionization balance facilitates the compensation of radial losses and the conservation of I in the $E_z(0)$ longitudinal electric field. A voltmeter in a discharge without particles shows $V_0 = E_z(0)l$ potential value. As microparticles enter the plasma along the discharge axis, they self-organize into a cloud that is confined within a r_c radius (as shown in the lower section of Fig. 1). A distinct pattern of losses and ionization processes is observed compared to that of a pure discharge. In addition to the losses of charged plasma particles on the walls of the discharge tube, there are also microparticle losses. The greater mobility of electrons compared to ions results in the generation of more intense electron flows on the microparticles, which defines their negative charge Microparticles may acquire a significant $q \sim 10^4 e^{-1}$. charge The electroneutrality equation for the dusty plasma can be expressed as $n_i = n_p q/e^{-} + n_e$. $n_i(r,$ The concentration of positive ions $n_i(r, n_p)$ within the microparticle cloud region increases, counteracting the high charge q, and can significantly surpass the ion concentration in the discharge that lacks $n_i(r, 0)$ microparticles. Compensation for the additional plasma losses associated with microparticles and maintenance of the current I is achieved by elevating the ionization frequency. This increase is driven by a rise in electron temperature resulting from a stronger longitudinal electric field E_z . The experiment revealed the development of a microparticle cloud within the discharge plasma, accompanied by a rise in potential V in the plasma region where the microparticle cloud

with r_c radius was formed. An increase in electron temperature was observed while studying the effect of dust particles on the intensity of plasma spectral lines [24]. The E_z field in a cloud plasma depends on n_p , since microparticles can represent a significant source of plasma losses [25]. A voltmeter in a discharge with a cloud with microparticles concentration n_p demonstrates an increase in the $V = E_z(n_p)l$ potential value. The shift in the maximum electron concentration position shown in Fig. 1 indicates that the ionization

peak shifts from the discharge axis beyond boundary. the cloud Experiments numerical calculations have revealed changes in the $E_z(n_p)$ field in a DC glow discharge resulting from varying concentrations of n_p for different gases, including air [26–28], neon [25, 29], argon [30], and helium [31]. The distributions of n_i shown in Fig. 1 indicate that the cloud of charged microparticles within the plasma acts as a trap for positive ions, concentrating the ions around the microparticles within the cloud.

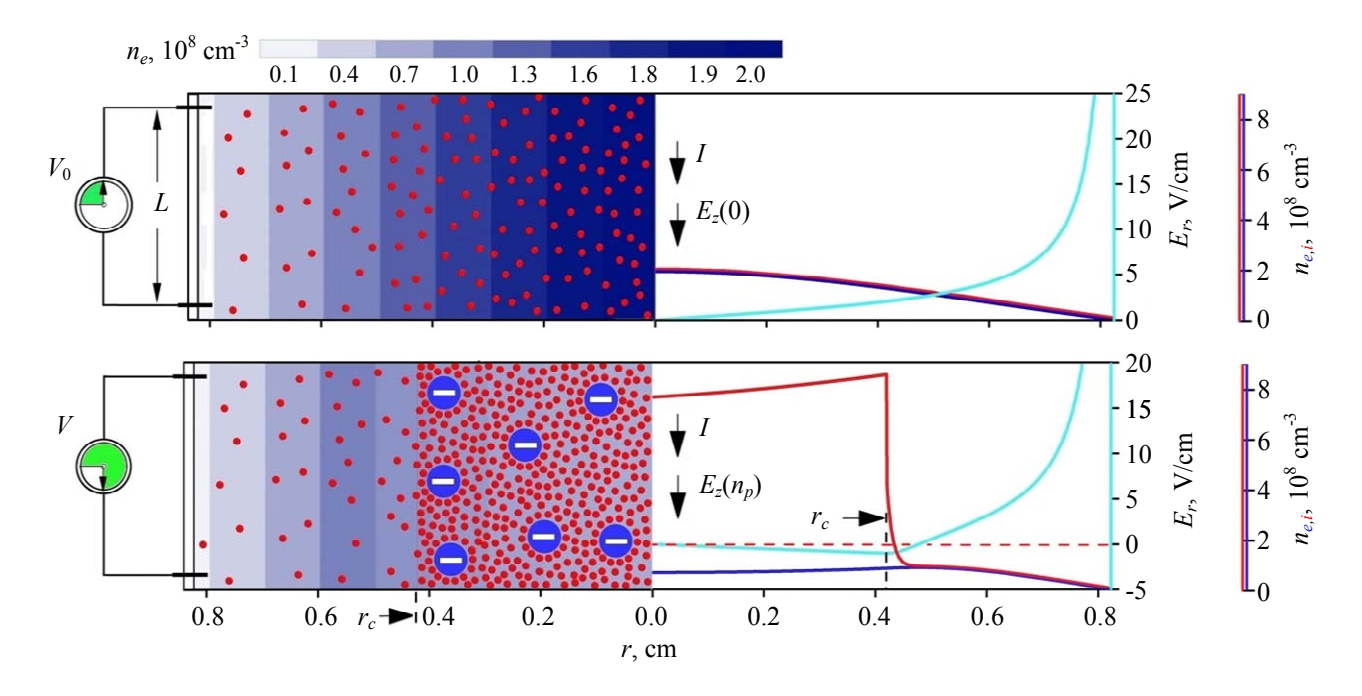


Fig. 1. Diagram shows the axial cross-section of the discharge tube containing plasma at the voltage V measurement point. The left side of the section shows the plasma composition: red dots represent positively charged ions, the blue area represent electrons, and blue circles represent negatively charged dust particles. The right side of the section displays the ions concentration profiles n_i (red lines), electrons n_e (blue lines), and the radial electric field E_r (light blue lines) for I=0.5 mA and p=0.6 Torr. The upper segment shows a discharge without microparticles, while the lower segment shows a discharge containing microparticles with $n_p=4\times10^5$ cm⁻³ in a cloud of r_c radius

A picture of the ion capture process by a negatively charged sphere, along with their distribution, was derived from PIC modeling [32]. The results demonstrated that the captured ions form dense clusters around the sphere, providing additional shielding while substantially compensating for the positive charge deficit of the plasma in the presence of a strong electric field near the sphere.

The effectiveness of an ion trap may be characterized by several metrics that assess the efficiency of ion accumulation for both a cloud and individual microparticles, as well as indicators that reflect the effectiveness of energy expenditures [16]. There are discharge modes with equivalent parameters in which the ion concentrations in the plasma region confined by the cloud radius in a discharge

containing microparticles $n_i(r_c, n_p)$ may exceed or fall below the concentrations $n_i(r_c, 0)$ observed in a discharge without microparticles. If $n_i(r_c, n_p) > n_i(r_c, 0)$, it indicates that the plasma cloud functions as trap. The efficiency of accumulation by the trap is determined by the $\zeta = n_i(r_{c_i}, n_p)/n_i(r_{c_i}, 0)$ [16, 17] ratio. When data on the number of ions in the plasma's reaction volume is available, the effectiveness of ion accumulation by the cloud can be assessed linear using ion density $\zeta^* = N_i(r_c, n_p)/N_i(r_c, 0).$ Where $N_i(r_c, n_p) =$ $= 2\pi \int_0^{r_c} r n_i(r, n_p) dr$ $N_i(r_{\rm c}, 0) =$ and = $2\pi \int_{0}^{r_c} r n_i(r, 0) dr$ represents the linear ion density in the cloud and linear ion density in the discharge without microparticles within the area defined by the cloud's radius, respectively [16, 33].

Fig. 2 shows the efficiency of ion accumulation by the cloud ζ^* as a function of microparticle concentration and discharge current under different neon pressures. If the complex system is in a state where $\zeta^* > 1$, then the trap acts as an ion concentrator and operates in state of effective ion a accumulation (area I in Figure 2). The maximum values of ion accumulation efficiency by the cloud ($\zeta_{max}^* = 4.73$ at $p = 0.6 \text{ Torr}, \zeta_{max}^* = 4.71 \text{ at } \zeta_{max}^* = 0.3 \text{ Torr},$ and $\zeta_{\text{max}}^* = 4.2$ at p = 0.9 Torr) are associated with the lowest values of I and the highest values of n_p . The inefficient state of the system corresponds to area II with $\zeta^* \leq 1$. The transition boundary between areas ($\zeta^* = 1$) is indicated with a white line. From Figure 2, we can conclude that the range of values for $\zeta^* \le 1$ increases as p rises, while I shifts to larger and smaller values with a n_p increase.

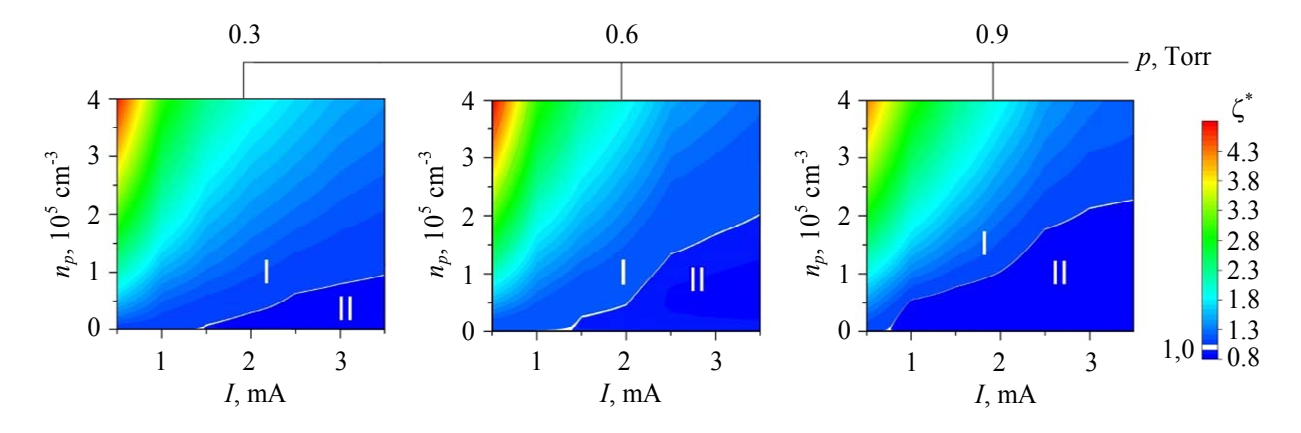


Fig. 2. The efficiency of ion cloud accumulation ζ^* depending on the concentration of microparticles n_p and the discharge current I under different neon pressures p

It can be postulated that the dusty plasma is a more effective method for generating the desired ion concentration compared to free discharge plasma. In a free discharge operating in normal mode, $n_i \propto I$, E_z exhibit minimal variation with changes in current or show no dependence on the current at all. The energy required to generate a single ion is directly proportional to the linear electric power of the discharge, given by $P_i \propto IE_z$ [16]. The generation of additional

ions as ionization frequency increases results in a corresponding rise in losses due to ambipolar diffusion toward the discharge boundary. In dusty plasma, a rise in ion concentration is attained under conditions of decreased ambipolar plasma losses, where further increases in ion concentration occur due to the redistribution of ions from the periphery of the discharge to the center of the microparticle cloud. In addition, free discharge has several disadvantages when

compared to discharge with microparticles, and an increase in current *I* results in:

- increased heat generation at the electrodes and additional electrodes erosion;
- an increase in near-electrode potential drops and heat generation in the nearelectrode plasma;
- increased heating of the discharge plasma and the onset of thermal instability, which causes the discharge to its contraction;
- the necessity to expand the cathode surface to achieve the required electron emission while keeping the current density at a normal level.

The energy advantage of a discharge with microparticles compared to a free discharge is linked to the additional Joule heating of the plasma. In dusty plasma, when producing the same ion concentration, less heat can be generated within a specific range of I values compared to plasma without microparticles, while maintaining the same p. Such modes were detected at I < 2.7 mA [14]. The energy advantage in these modes is assessed by calculating the relative overheating coefficient η_O . In reference [14], this coefficient was calculated as the ratio of the additional linear power consumed in the plasma of a free discharge while achieving same ion concentration, corresponding value in a discharge with microparticles $\eta_O = Q(n_p = 0)/Q(n_p)$. In a free discharge, an increase in ion concentration can be attained by raising the current by a value ΔI while keeping $E_z \approx \text{const.}$ In contrast, in a discharge with microparticles, this increase is linked to a rise in the electric field ΔE_z while maintaining a I = const, resulting in $\eta_O \approx \Delta I E_z / \Delta E_z I$. Understanding the η_O coefficient is particularly valuable for plasma technologies and processes that take place at low and cryogenic temperatures, where heat generation is not desirable [10, 11, 19, 20, 33, 34].

Fig. 3 shows the change in η_Q with pressure for different discharge currents. Higher currents lead to lower η_Q values across the entire pressure range. The thermal

gain in the complex plasma diminishes faster increasing pressure. The thermal with gain vanishes at point (8) (I = 2.7 mA)p = 0.3 Torr), as shown in Fig. 4. At this point, the heat released in the complex plasma equals the heat released in the free discharge. For a current of 0.5 mA, the η_0 distribution peaks at approximately $p \approx 0.5 \text{ Torr } (1)$. At this pressure, the complex plasma exhibited a significant thermal gain, with $\eta_Q \approx 13$. With increasing current, this peak shifts towards lower pressures, reaching p = 0.3 Torr at I = 0.75 mA (3).

Complex plasma offers an advantage over free-discharge plasma through its ability to control the microparticle cloud [17, 35]. This control enables manipulation of the cloud's spatial arrangement in the discharge, leading to optimized conditions for achieving desired ion concentrations within the reaction zone.

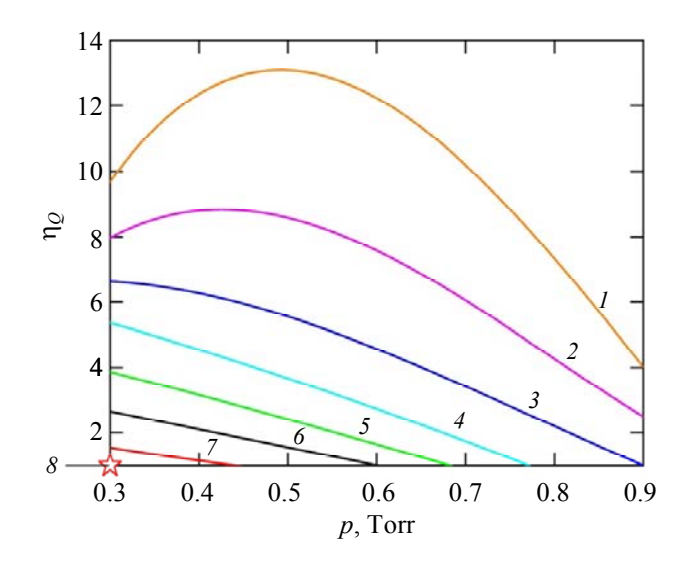


Fig. 3. The relationship between relative overheating coefficient η_0 and neon pressure p, shown for various discharge currents I: 1 - 0.5 mA, 2 - 0.6 mA, 3 - 0.75 mA, 4 - 1 mA, 5 - 1.5 mA, 6 - 2 mA, 7 - 2.5 mA, 8 - 2.7 mA

Conclusion

Within a specific range of discharge parameters, a low-pressure direct current discharge creating a complex plasma with microparticles functions as an electrostatic plasma trap. This trap accumulates and

ions within the localizes charged microparticle cloud. In some dusty plasma modes, ion concentrations within the cloud are lower than those achieved under identical conditions in a free discharge in the same plasma area. We propose using the linear ion density within the microparticle ζ^* cloud as a measure of the effectiveness of ion accumulation. We measured ζ^* values across a range of microparticle concentrations $(n_p = 0-4\times10^5 \text{ cm}^{-3})$ and discharge currents (I = 0.5 - 3.5 mA),specifically pressures of 0.3, 0.6, and 0.9 Torr. Results indicate that ζ^* is maximized when the discharge current is minimized and the microparticle concentration is maximized. The parameter regions for which $\zeta^* > 1$ correspond to an ion trap that concentrates ions and operates in a state of effective accumulation. We identified inefficient states of the plasma system with $\zeta^* \leq 1$. We found that the range of values $\zeta^* \leq 1$ on $n_n - I$ diagrams expands with increasing pressure, expanding to both higher and lower currents, and with increasing microparticle concentration. We observed that the thermal gain of the complex plasma, as measured by the relative overheating coefficient η_{O} , increases with pressure at lower discharge currents. $\eta_O \approx 13$ reaches its maximum value at $p \approx 0.5$ Torr and I = 0.5 mA. It has been shown that the dusty plasma is a more effective method for generating the desired ion concentration compared to free discharge plasma.

The work was performed with the support of the Ministry of Science and Higher Education of the Russian Federation (State assignment No. № 075-00269-25-00).

REFERENCES

- 1. Dehmelt H., Rev. Mod. Phys. **62**, 525–530 (1990).
- 2. Paul W., Rev. Mod. Phys. **62**, 531–540 (1990).
 - 3. Mihalcea B. M., Filinov V. S.,

- Syrovatka R. A. and Vasilyak L. M., Phys. Rep. **1016**, 1–103 (2023).
- 4. Balakrishnan N., J. Chem. Phys. **145**, 150901 (2016).
- 5. Langin T. K., Gorman G. M. and Killian T. C., Science **363**, 61 (2019).
- 6. Wineland D. et al., Phys. Rev. Lett. **59**, 2935–2938 (1987).
- 7. Bollinger J. J. et al., J. Phys. B: At. Mol. Opt. Phys. **36**, 499–510 (2003).
- 8. Krems R. V., Phys. Chem. Chem. Phys. **10**, 4079–4092 (2008).
- 9. Goldanskii V. I., Ann. Rev. Phys. Chern. **27**, 85–126 (1976).
- 10. Polyakov D. N., Shumova V. V. and Vasilyak L. M., Surf. Eng. Appl. Electrochem. **51**, 143–151 (2015).
- 11. Stauss S., Muneoka H. and Terashima K., Plasma Sources Sci. Technol. **27**, 023003 (2018).
- 12. Vasilyak L. M. et al., New J. Phys. **15**, 043047 (2013).
- 13. Grigorian G. M., Dyatko N. A. and Kochetov I. V., Phys. Plasmas. **24**, 073503 (2017).
- 14. Polyakov D. N., Shumova V. V. and Vasilyak L. M., J. Appl. Phys. **128**, 053301 (2020).
- 15. Fortov V. E. and Morfill G. E. Complex and Dusty Plasmas: From Laboratory to Space. Boca Raton, CRC Press, 2009.
- 16. Polyakov D. N., Shumova V. V. and Vasilyak L. M., Plasma Sources Sci. Technol. **31**, 074001 (2022).
- 17. Polyakov D. N., Shumova V. V. and Vasilyak L. M., Plasma Sources Sci. Technol. **30**, 07LT01 (2021).
- 18. Thomas E., Amatucci W. E., Compton Ch. and Christy B., Phys. Plasmas. **9**, 3154–3158 (2002).
- 19. Polyakov D. N., Shumova V. V. and Vasilyak L. M., Russ. J. Phys. Chem. B. **17** (4), 1241–1245 (2023).
- 20. Shumova V. V., Polyakov D. N. and Vasilyak L. M., Russ. J. Phys. Chem. B. **19**. (2025) (in print).
 - 21. https://www.bolsig.laplace.univ-tlse.fr/
 - 22. https://nl.lxcat.net
- 23. Khrapak S. A., Morfill G. E., Khrapak A. G. and D'yachkov L. G., Phys. Plasmas. **13**, 052114 (2006).
- 24. Kostenko A. S., Ochkin V. N. and Tskhai S. N., Tech. Phys. Lett. **42** (7), 743–746 (2016).
- 25. Polyakov D. N., Shumova V. V. and Vasilyak L. M., Plasma Phys. Rep. **43** (3), 397–404 (2017).
- 26. Vasilyak L. M., Polyakov D. N., Fortov V. E. and Shumova V. V., High Temp. **49**, 623–628 (2011).
 - 27. Polyakov D. N., Shumova V. V. and

- Vasilyak L. M., Surf. Eng. Appl. Electrochem. **49**, 114–124 (2013).
- 28. Ding Z., Chen Q., Liu C. and Qian Z., Journal of Electrostatics **135**, 104048 (2025).
- 29. Vasilyak L. M., Polyakov D. N. and Shumova V. V., Contrib. Plasma Phys. **53**, 432–435 (2013).
- 30. Tian R. et al., Journal of Applied Physics **123**, 083301 (2018).
- 31. Fedoseev A. V., Salnikov M. V., Demin N. A. et al., Phys. Plasmas. **25**, 083710 (2018).
 - 32. Kiselyov A. A., Dolgonosov M. S. and

- Krasovsky V. L., Doklady Physics **59** (5), 209–213 (2014).
- 33. Polyakov D. N., Shumova V. V. and Vasilyak L. M., Russ. J. Phys. Chem. B. **18** (4), 1128–1133 (2024).
- 34. Shumova V. V., Polyakov D. N. and Vasilyak L. M., J. Phys. D: Appl. Phys. **50**, 405202 (2017).
- 35. Polyakov D. N., Shumova V. V. and Vasilyak L. M., Plasma Phys. Rep. **50** (12), 1609–1613 (2024).

About authors

Dmitry Nikolaevich Polyakov, senior research scientist, Joint Institute for High Temperatures of Russian Academy of Sciences (125412, Russia, Moscow, 13, Izhorskaya st., bldg. 2). E-mail: cryolab@ihed.ras.ru SPIN-code 8670-4302, Author ID 25782

Valeria Valerievna Shumova, Candidate of Physical and Mathematical Sciences, senior research scientist, Joint Institute for High Temperatures of Russian Academy of Sciences (125412, Russia, Moscow, 13, Izhorskaya st., bldg. 2); Semenov Federal Research Center for Chemical Physics, Russian Academy of Sciences (119991, Russia, Moscow, 4, Kosygina st.). E-mail: shumova@ihed.ras.ru SPIN code 2700-8783, Author ID 12812

Leonid Mikhailovich Vasilyak, Doctor of Physical and Mathematical Sciences, Senior Research Assistant, Joint Institute for High Temperatures of Russian Academy of Sciences (125412, Russia, Moscow, 13, Izhorskaya st., bldg. 2). E-mail: vasilyak@ihed.ras.ru SPIN code 5623-5167, Author ID 19599

PLASMA PHYSICS AND PLASMA METHODS

UDC 537.523.9 PACS: 52.80.-s

Influence of electrolyte temperature on the formation of small-scale current pulsations in a gas discharge with a liquid cathode

© G. K. Tazmeev and A. K. Tazmeev

Kazan (Volga Region) Federal University, Naberezhnye Chelny Institute, Naberezhnye Chelny, 423812 Russia * E-mail: gktazmeev@kpfu.ru

> Received 29.01.2025; revised 25.04.2025; accepted 11.08.2025 Scientific specialty code: 1.3.9

A gas discharge with a liquid electrolyte cathode was experimentally studied in the following parameter ranges: current 80–170 mA, electrolyte temperature 5–70 °C, interelectrode distance 2–8 mm. An aqueous solution of sodium chloride with a molar concentration of 0.1 mol/l was used as a cathode. The formation of current pulsations was considered under the assumption of droplet transfer of matter from the aqueous solution to the discharge plasma.

Keywords: gas discharge; liquid-plasma interface; droplet transfer of matter; charge transfer; liquid cathode discharge; water-solution cathode; current pulsations.

DOI: 10.51368/1996-0948-2025-4-45-50

Introduction

Gas discharges created with the use of liquid electrolytes as electrodes offer a versatile source of plasma with extensive practical applications [1, 2]. Many researchers have explored gas discharge with liquid electrolyte cathode [3-7],generating substantial experimental data on its electrical, thermal, and optical properties. However, the processes governing matter and charge transfer at the plasma-liquid boundary remain incompletely understood. Studies [8, 9] suggest that the transfer of electrolyte matter into plasma occurs through local non-equilibrium evaporation impacted by ion flux bombarding the cathode. This approach, however, fails to clarify mechanism of droplet formation. The mechanism of cathode sputtering in the form of small droplets also lacks explanation.

The study [10] presents the use of an aqueous sodium chloride solution as a liquid electrolyte cathode. The authors proposed two mechanisms for droplet generation from the electrolyte cathode. The first mechanism involves distortion of the electrolyte surface shape, where droplets form at the tip of the cone-shaped electrolyte surface due to a process equal to electrospraying. High-speed video recording revealed this first mechanism operating during the early stage of discharge temporal evolution. The second mechanism involves an explosive reaction between sodium particles and water. The authors assume that sodium particles form from atoms in the gas phase. However, questions remain about how sodium particles form and why they move toward the aqueous solution (electrolyte cathode) rather than being carried away by the vapor-air flow. They suggest that this second mechanism creates a self-sustaining liquid cathode sputtering process.

The study [11] reported spectroscopic investigations of discharge plasma with a distilled water electrode. Optical effects arising under various factors were analyzed. One of these factors was the temperature of the water serving as the cathode. The authors observed a decrease in OH band intensity by half when water temperature increased from 30 to 60 °C. This effect is presumed to be caused by an increase in the partial pressure of water vapor.

The influence of liquid cathode temperature on discharge properties was intentionally studied by the authors of paper [12]. In this study, direct current discharge occurred between a liquid electrolyte cathode and a metal anode nozzle emitting a miniature helium flow. An aqueous sodium chloride solution served as the cathode. As a result, a significant influence of the liquid electrolyte cathode temperature on sodium transport into the plasma was revealed. Sodium radiation intensity decreased along with cathode cooling and increased with heating. When they applied pulse-modulated direct current voltage, sodium emission displayed a delay relative to discharge initiation.

These findings demonstrate that liquid electrolyte temperature profoundly affects matter transfer from electrolyte cathode to plasma. This study aims to investigate the influence of liquid electrolyte temperature on droplet transfer through analysis of current oscillograms.

Experiment

The experimental setup diagram is shown in the Fig. 1. The discharge occurred in air between a metal anode (1) and a liquid electrolyte cathode (2), while ignition was

achieved by a contact using an auxiliary metal The interelectrode electrode. distance (hereinafter *l*) was set by changing the liquid electrolyte level in a vessel (3). The anode was a tungsten rod with a diameter of 3 mm. An aqueous sodium chloride solution with a molar concentration of 0.1 mol/l was used as the electrolyte. A graphite electrode (4) was used to create electrical contact with the liquid electrolyte. It was placed in a vessel (5) with openings (6) near the bottom. The use of the vessel (5) prevented electrolysis hydrogen formed on the surface of electrode (4) from entering the discharge zone under the anode (1). Thus, the current pulsations that could arise due to hydrogen bubbles entering the discharge zone were excluded. Electrical power was supplied from source (10), equipped with an induction-capacitance filter. The output voltage was 1740 V. The current was regulated by changing the resistance of ballast resistor R1 within the range of $6-12 \text{ k}\Omega$. A digital oscilloscope (AKIP-15/1, Professional Control and with Measurement Equipment) 25 MHz bandwidth recorded current oscillograms using a 10Ω shunt resistor (R2). A mercury thermometer (8) with 1°C divisions measured electrolyte temperature.

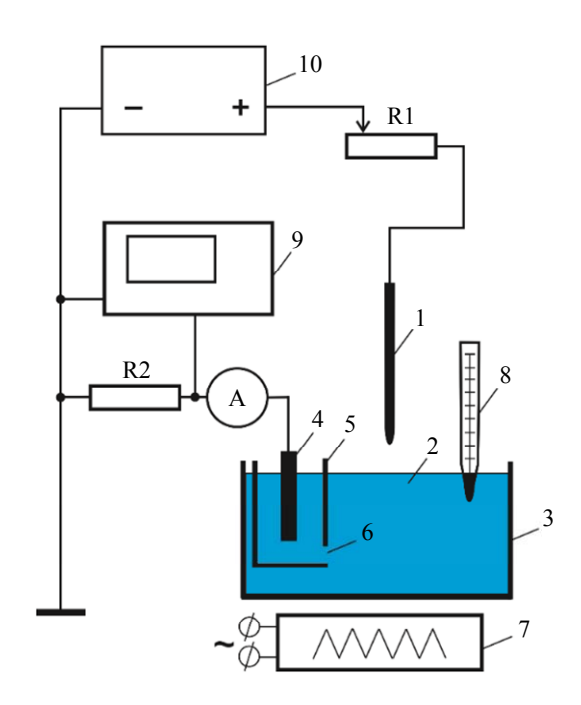


Fig. 1. Experimental unit

An electric heater (7) with a power of 1 kW was used to increase the temperature of the aqueous solution. Uniform heating was achieved through mechanical stirring. Measurements were conducted with heater turned off for a short period of about 1 minute. During this short period, temperature of the aqueous solution changed insignificantly (no more than 1 °C). For experiments requiring below-roomtemperature conditions, pre-cooled solutions were used.

The duration of a single experiment (the time during which discharge ignition, solution temperature measurement, and oscillogram recording were performed) did not exceed 1 minute. Experiments conducted using the contact method (by touching the liquid cathode with the metal anode at a maximum current of 170 mA) showed that Joule heating

of the solution (liquid cathode) could be neglected within the experiment.

The instantaneous photographs of the discharge were obtained using a high-speed VIDEOSCAN-401 camera.

Results of Experiments and Analysis

Figure 2 presents current oscillograms characteristic of discharge behavior across small (2 mm) and extended (8 mm) discharge gaps. Small-gap discharges exhibit minimal current pulsations (Fig. 2*a*–*c*). As electrolyte temperature increases, vertical artifact streaks appear in the oscillograms, creating a background that makes it difficult to observe current pulsations (Fig. 2*c*). This happens due to thermal degradation of the anode, which causes a release of metallic microparticles, seen as the streaks.

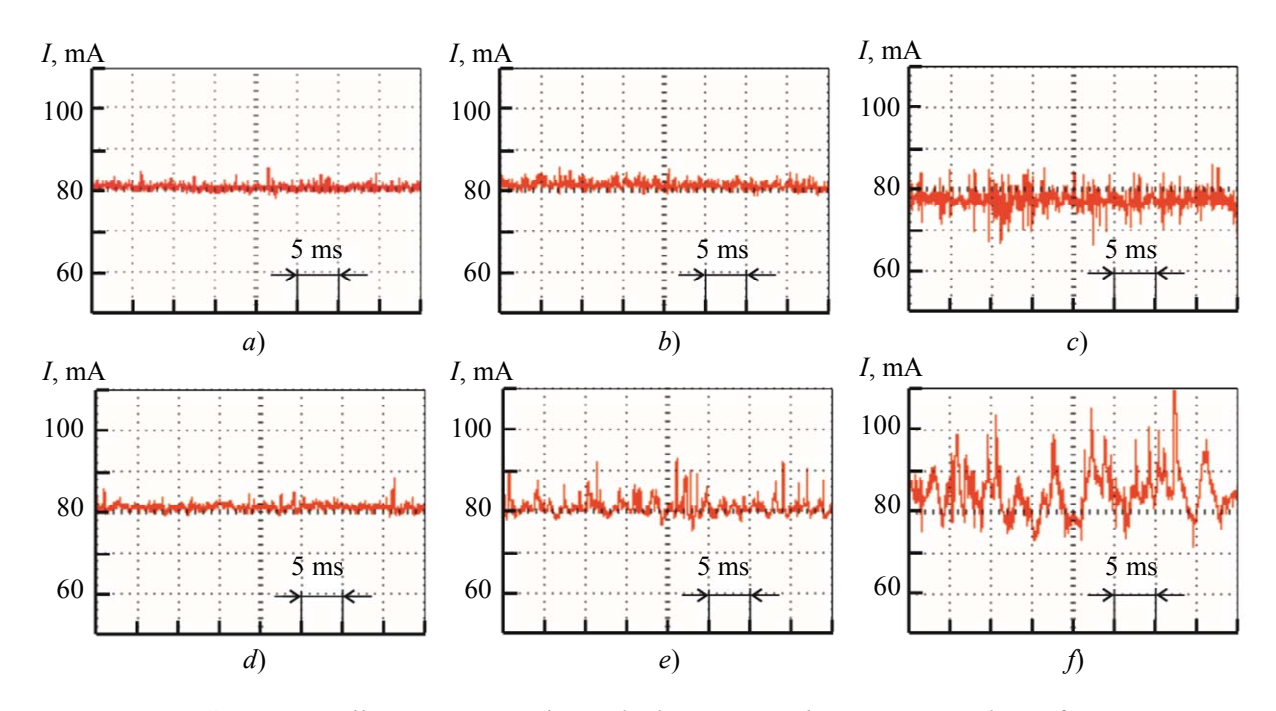


Fig. 2. Current oscillograms. Interelectrode distance: a), b), c) – 2 mm; d), e), f) – 8 mm. Electrolyte temperature: a), d) – 6 \mathbb{C} ; b), e) – 20 \mathbb{C} ; c), f) – 70 \mathbb{C}

The experiments showed that electrolyte temperature effects become significant as interelectrode distance *l* increases. In this case, temperature increase leads to substantial intensification of pulsations. This pattern is clearly demonstrated by the oscillograms in

Fig. 2*d*–*f*. The amplitude of pulsations gradually increases and at a temperature of 70 °C reaches tens of milliamperes (Fig. 2*f*).

A distinctive feature of current pulsations is that they occur as upward jumps from a nominal current value. Their

frequency and amplitude vary randomly. Based on such patterns observed in the oscillograms, it can be assumed that current pulsations form due to the ejection of liquid electrolyte cathode droplets into the discharge region. These droplets carry sodium from the electrolyte, which subsequently ionizes in the discharge region. The electrons released during sodium ionization readily respond to the electric field, contributing to current flow. Each droplet thus introduces additional current carriers into the discharge zone, triggering abrupt increases. current Simultaneously with ionization. recombination processes occur. Naturally, this decreases the number of electrons, and the current decreases to its nominal value.

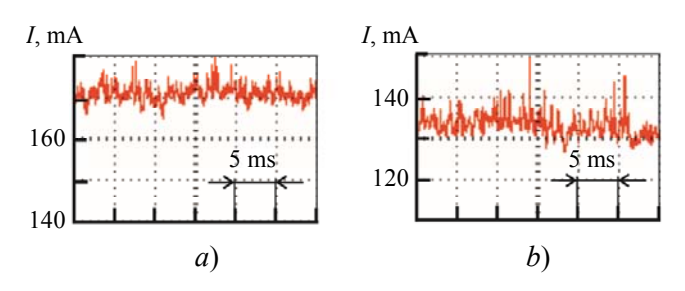


Fig. 3. Oscillograms at elevated currents. a) -l = 2 mm, electrolyte temperature is 20 °C; b) -l = 8 mm, electrolyte temperature is 6 °C

Figure 3 shows oscillograms recorded at elevated currents. The temperature conditions were selected in such a way to enable comparison with the oscillograms in Fig. 2. Fig. 3a can be compared with Fig. 2b, and Fig. 3b with Fig. 2d. In both cases, the same pattern is revealed. At the same electrolyte temperatures, instead of insignificant pulsations (Fig. 2b and 2d), more intense ones appear (Fig. 3a and 3b). Consequently, increasing current contributes to intensification of current pulsations. Apparently, this can be related to thermal phenomena, happening in the discharge attachment zone on the electrolyte surface. The primary energy input to the electrolyte comes from bombardment cathode positive ions, accelerated by the electric field.

With increasing current, the number of bombarding ions increases, delivering energy faster than thermal conductivity and convection can dissipate it. This triggers explosive localized boiling with droplet ejection. Sodium contained in the droplets acts as an indicator of such explosive boiling. As already noted, this sodium contributes to current pulsation formation when entering the discharge region.

Another feature of current pulsations is that they are most intense at relatively low frequencies. It was clearly seen in pulsation spectra obtained using the oscilloscope's Fourier analysis function. As an illustration of this phenomenon, Fig. 4 shows a randomly formed spectrum, highlighting the 0–1.0 kHz frequency range where current pulsation amplitudes reach their maximum. Above 1.0 kHz, the pattern becomes monotonic without significant amplitude peaks. These patterns occurred consistently at both low and elevated temperatures of the aqueous solution (liquid cathode).

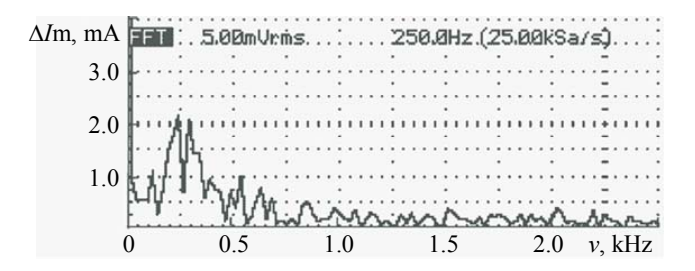


Fig. 4. Current pulsation spectrum. Electrolyte temperature is 70 °C. l = 6 mm. I = 100 mA

Due to the fact that sodium transfers from the electrolyte to the discharge region, the interelectrode space turns yellow (Fig. 5).

When the discharge operates across short gaps, the interelectrode space becomes almost entirely filled with a yellow cloud (Fig. 5a-c). As the electrolyte temperature rises, the yellow cloud expands and begins to enshroud the anode tip (Fig. 5c). Apparently, the anode heats more intensely under such conditions. It begins to erode, resulting in background artifacts appearing in the

oscillograms (Fig. 2c). When the discharge operates across more extended gaps, the yellow clouds adjoins the electrolyte surface (Fig. 5d, 5c, and 5f). Increasing the electrolyte temperature to 70° C leads to a substantial increase in its size (Fig. 5f). This pattern

indicates a significant increase in the amount of matter entering the discharge region from the liquid electrolyte. Some of the matter is carried in the form of droplets. The higher the electrolyte temperature, the more intense the droplet transfer of matter becomes.

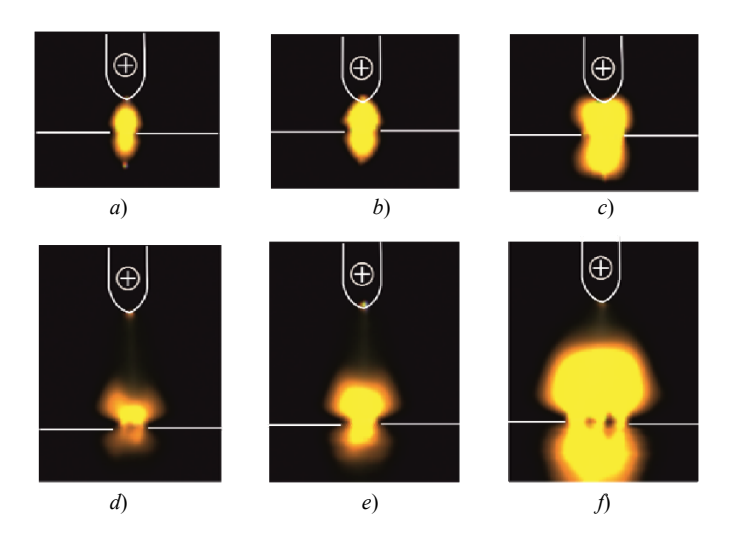


Fig. 5. Instantaneous photos of the discharge. The white lines indicate the anode contours and the electrolyte surface. The discharge column's reflection can be observed on the solution surface. The exposure is 1 ms. Interelectrode distance: a, b, c) – 2 mm; d), e), f) – 8 mm. Electrolyte temperature: a), d) – 6 C; b), e) – 20 C; c), f) – 70 C

Conclusion

It has been experimentally established that small-scale current pulsations arising in a gas discharge with a liquid electrolyte cathode significantly depend the electrolyte temperature. Increasing the electrolyte temperature results intensification of these pulsations. At lower temperatures, it is possible to achieve discharge conditions with minimal current pulsations. The observed pulsation formation patterns align with the droplet model of a matter transfer from the liquid cathode to the plasma. These findings can serve as a basis for a more comprehensive development of this model.

This research was funded by a grant from the Academy of Sciences of the Republic of Tatarstan awarded to young Candidates of Science (postdoctoral researchers) to support doctoral dissertation defense, research activities, and work in scientific and educational institutions of the Republic

of Tatarstan under the State Program 'Scientific and Technological Development of the Republic of Tatarstan', agreement No. 42/2024-PD dated December 16, 2024.

REFERENCES

- 1. Reuter S. and Hamdan A., Plasma Processes and Polymers **22** (1), 2400278 (2025).
- 2. Bruggeman P. J. et al., Plasma sources science and technology **25** (5), 053002 (2016).
- 3. Verreycken T., Schram D. C., Leys C. and Bruggeman P., Plasma Sources Sci. Technol. **19**, 045004 (2010).
- 4. Sirotkin N. A. and Titov V. A., Applied Physics, No. 6, 25 (2016) [in Russian].
- 5. Barinov Yu. A., Applied Physics, No. 6, 19–22 (2023) [in Russian].
- 6. Chistolinov A. V., Yakushin R. V., Lubin A. A. and Perfilieva A. V., Applied Physics, No. 4, 5–13 (2024) [in Russian].
- 7. Tazmeev G. K., Timerkaev B. A., Tazmeev K. K. and Miftakhov M. N., High Energy Chemistry **52** (1), 99 (2018).
- 8. Zakharov A. G., Maksimov A. I. and Titova Yu. V., Russian Chemical Reviews **76**, 235 (2007).

- 9. Khlyustova A. V., Maksimov A. I. and Sirotkin N. A., Elektronnaya obrabotka materialov **47**, 66 (2011).
- 10. Shirai N., Suga G. and Sasaki K., Plasma Sources Sci. Technol. **29**, 025007 (2020).
- 11. Chuchman M. P. et al., Journal of Applied Spectroscopy **83** (5), 781 (2016).
- 12. Shirai N., Ichinose K., Uchida S. and Tochikubo F., Plasma Sources Sci. Technol. **20**, 034013 (2011).

About authors

Tazmeev Gayaz Kharisovich, Ph.D. of Technical Sciences, Associate Professor, Kazan (Volga Region) Federal University, Naberezhnye Chelny Institute (423812, Russia, Naberezhnye Chelny, Prospect Mira, 68/19). E-mail: gktazmeev@kpfu.ru SPIN code 2893-0027, Author ID 937904

Tazmeev Almaz Kharisovich, Ph.D. of Chemical Sciences, Associate Professor, Kazan (Volga Region) Federal University, Naberezhnye Chelny Institute (423812, Russia, Naberezhnye Chelny, Prospect Mira, 68/19). E-mail: tazmeev@gmail.com SPIN code 9342-6714, Author ID 719638

=PLASMA PHYSICS AND PLASMA METHODS =

UDC 537.521 PACS: 51.50.+v

EDN: XRYSUD

On the characteristics of the positive column of a glow discharge at low pressure of an inert gas

© S. A. Maiorov¹, R. I. Golyatina², E. S. Dzlieva³ and V. Yu. Karasev³

¹ Joint Institute for High Temperatures of the Russian Academy of Sciences, Moscow, 125412 Russia

*E-mail: mayorov_sa@mail.ru

² Prokhorov General Physics Institute of the Russian Academy of Sciences, Moscow, 119991 Russia

E-mail: rusudan@intemodino.com

³ Saint Petersburg State University, Saint Petersburg, 199034 Russia
E-mail: plasmadust@yandex.ru

Received 25.06.2025; revised 5.08.2025; accepted 11.08.2025 Scientific specialty code: 1.3.9

The analysis of the kinetic characteristics of electrons and ions during their drift in inert gases under experimental conditions with dusty plasma in a direct current discharge in a tube with a diameter of 2 cm, a gas pressure of 0.33 Torr and a current of 1.5 mA was performed. The electron drift velocity, Townsend energy coefficient, average energy, ionization coefficient, and the fraction of energy input to gas excitation and ionization for cases of homogeneous and stratified discharges were calculated using the many-particle dynamics method with Monte Carlo collision simulation. Estimates of the wall potential and plasma density were obtained and compared with the experiment. The characteristics of the ion component are calculated and the influence of nickel cathode sputtering on the time characteristics of the discharge is assessed.

Keywords: glow discharge; diffusion; mobility; distribution function; Monte Carlo method; ionization; inert gases; cathode sputtering; gas heating.

DOI: 10.51368/1996-0948-2025-4-51-58

Introduction

This paper is aimed at conducting the analysis of experiments with dusty plasma the results of which are presented in [1]. This paper depicts how dust traps were formed in fixed striations in a glow-discharge in different inert gases with the same discharge parameters: discharging tube with a radius R = 1 cm, pressure p = 0.33 Torr and

current i = 1.5 mA. We obtained data on the size of dust particles trapped in the gravity-electrostatic trap for all inert gases. Very significant changes in the average size of polydisperse quartz particles were discovered: from 6.3 µm in helium to 3.0 µm in xenon. This indicates a very big shift in plasma characteristics of the positive column in a discharge with different plasma-supporting gases with the same similarity

parameters $pR = 3.3 \times 10^{-4} \text{ Torr} \cdot \text{cm}$ and $i/R = 1.5 \times 10^{-3} \text{ A} \cdot \text{cm} [2-5].$

Let us consider the main factors affecting the dust subsystem with the same current and pressure of different gases in a tube of a fixed diameter:

- 1) when the gas grade changes, the voltage between the anode and cathode also changes, the value of the average electric field strength in the positive column and the electron energy distribution function determining all the kinetic characteristics of the electronic subsystem.
- 2) dust particles levitate in a stratum with a strongly inhomogeneous electric field and the non-locality effect can be very significant;
- 3) ionic component determines not only the entrainment force affecting the dust particles but also the ionization frequency necessary to maintain the self-sustaining discharge due to the ionic recombination on the tube walls;
- 4) cathode sputtering leads to the appearance of metal vapors in noble gases which are ionized more easily and can significantly change the ionic composition of plasma in a fairly short period of time.

In the experiment [1] the positive column contained dust particles but the conditions were such that they did not significantly affect the gas discharge plasma characteristics. This situation is typical for dust systems in direct current discharges at low gas pressure. The problems of ions and electrons drift do not take into account the influence of dust particles on the gas discharge plasma characteristics.

Characteristics of ions drift

In case of strong fields of low gas temperatures [6], the deviation of the ion distribution function from the shifted Maxwell's function can be very significant and the average random energy of ions along the electric field and across it can vary greatly. To consider the effect of ion heating during drift in the electric field, it is convenient to introduce the concept of effective ion temperature: $T_{eff} = \frac{2}{3} \langle \varepsilon \rangle =$

 $=\frac{1}{3}m\langle v^2\rangle$, which consists of thermal motion of ions and directed energy and together with drift speed it is an average (hydrodynamic) characteristic of ion flux. It is the effective temperature of ions as a measure of their average energy determines for example, Debye ionic radius.

Despite the fact that the ion distribution functions both along and across the field direction are very different from the Maxwell's value [6], it makes sense to introduce two different ion temperatures – longitudinal T_L along the field and transversal T_T across the field as measures of mean-square deviation from the average value (dispersion). At the same time the average ion energy consists of the direct and random motion of ions with different dispersion relative to the drift direction:

$$\langle \varepsilon \rangle = \frac{1}{2} m W^2 + \frac{1}{2} T_L + T_T,$$

where *W* is drift speed.

In Table 1 for the experimental conditions of [1] the results of calculation using Monte-Carlo method [6] of the characteristics of drift of the inert gas singly charged ions in the homogeneous field: gas grade, field value *E*, drift speed *W*, directed motion energy, effective, longitudinal and transversal temperatures, coefficients of longitudinal and transversal diffusion.

Table 1

WΕ, D_T , mW^2 , KGas T_{eff} , K T_L , K T_T , K D_L , cm²/s V/cm km/s cm²/s He 8.5 1.64 646 1072 2385 416 1105 635 0.49 293 Ne 6 662 1248 368 328 249 499 92 Ar 4.5 0.16 64 377 316 96 7 429 59 58 Kr 0.14 105 626 330 Xe 5 0.07 38 344 419 307 38 34

Characteristics of ions drift of inert gases

Characteristics of electrons drift

The electronic subsystem largely determines the dusty plasma characteristics and, ultimately, the size of trapped dust particles. With the same discharge current and gas pressure, in addition to the ionization potential and atom weight, the voltage in the tube and the electric field distribution also change. The average values of the field in [1] were determined according to the voltage on the positive column (considering cathode and anode potential drop) and its length. Since the positive column was stratified in experiments, the drift was calculated for each gas in a constant homogeneous field or strongly inhomogeneous periodic $E(x) = \langle E \rangle [1 + \delta \sin(2\pi x/L)]$ with an amplitude of the average field value order <E>. Field period L is determined according to the Novak rule [2, 7–9]: e < E > = IL. Influence of the field inhomogeneity on the drift characteristics was studied in [10, 11].

Results ofcalculation of the characteristics of electrons drift are given in Table 2. For each gas grade two first lines is drift in homogeneous ($\delta = 0$) and periodic $(\delta = 1)$ fields of the released electron (Bulk model); the next two lines are drift in homogeneous and periodic fields with recombination on the wall of the most energetic electron during the ionization act (SST wall model) [12, 13]. Temperature of drift speed, Townsend energy coefficient, effective temperature determined through the average energy value, wall potential, share of radiation and ionization losses in the energy balance, ionization reduced factor.

Fig. 1–5 show the dependence of the electric field in the stratum, distributed of the average energy along the length, drift speed and energy deposition share used for ionization.

Characteristics of electrons drift

Gas		δ	W, km/s	eD_{\perp}/μ , eV	$T_{e\!f\!f},\mathrm{eV}$	ϕ_{wall},V	$\alpha_{\rm rad}$, %	α_{ion} , %	α/N , Å ²
Не	Bulk	0	187	7.4	7.73	∞	55.4	30.9	0.098
		1	149	8.05	6.53	8	54.9	31.4	0.100
	SST	0	170	7.28	7.26	40.0	47.4	20.0	0.064
		1	123	8.63	5.82	39.7	49.9	21.6	0.068

Table 2

End of Table 2

Gas		δ	W, km/s	eD_{\perp}/μ , eV	$T_{e\!f\!f},\mathrm{eV}$	ϕ_{wall},V	$\alpha_{\rm rad}$, %	$\alpha_{\rm ion}$, %	α/N , Å ²
Ne	Bulk	0	151	8.7	7.60	∞	56.8	33.4	0.085
		1	142	9.08	6.95	8	54.1	35.5	0.091
	SST	0	145	9.81	7.29	31.8	50.3	21.6	0.055
		1	137	9.20	6.46	32.0	46.7	22.2	0.057
Ar	Bulk	0	41.3	6.45	3.96	8	92.9	5.1	0.013
		1	39.1	6.91	4.04	∞	86.0	12.1	0.032
	SST	0	41.7	6.52	3.96	16.6	89.9	4.0	0.011
		1	39.4	7.69	4.02	17.4	79.9	9.0	0.024
Kr	Bulk	0	47.6	5.88	3.54	8	83.8	14.1	0.065
		1	45.1	6.16	3.54	8	75.5	21.3	0.098
	SST	0	48.2	5.25	3.52	16.0	78.6	9.6	0.044
		1	45.3	6.90	3.48	16.6	65.9	15.2	0.069
Xe	Bulk	0	26.9	4.70	2.79	∞	93.3	5.5	0.021
		1	24.8	5.32	2.85	8	85.0	13.2	0.050
	SST	0	26.4	5.09	2.78	12.5	89.6	4.2	0.016
		1	24.8	4.85	2.82	12.9	79.6	9.7	0.037

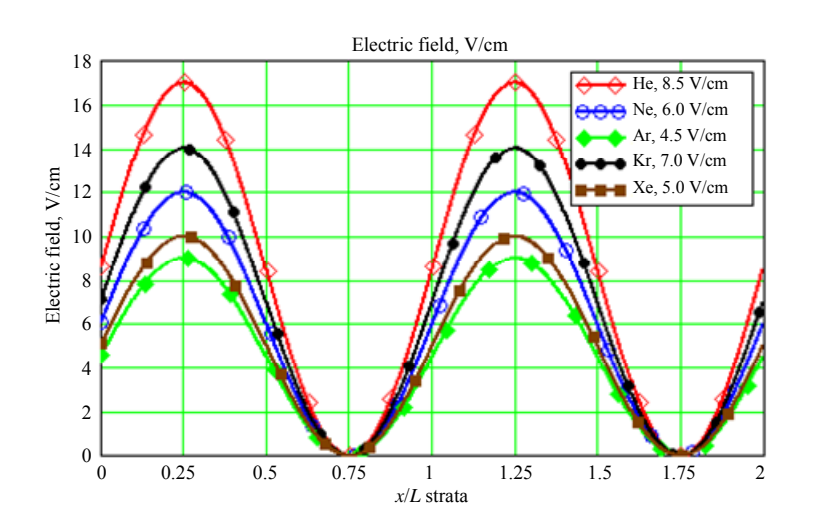


Fig. 1. Dependence of the electric field along the strata length

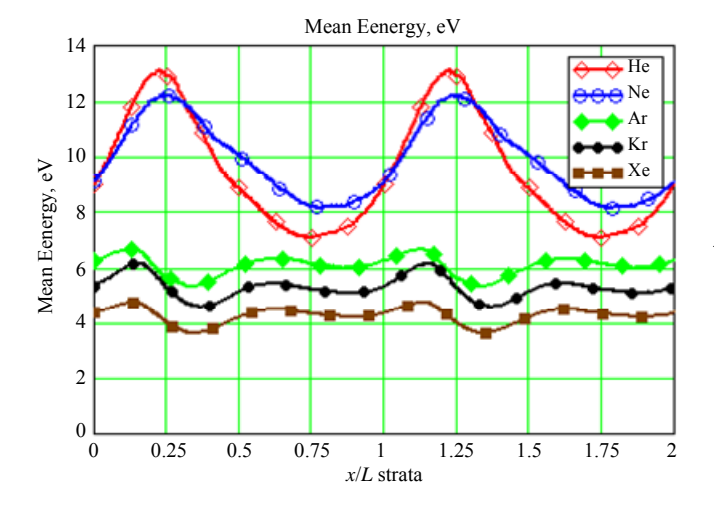


Fig. 2. Distribution of average energy along the strata length

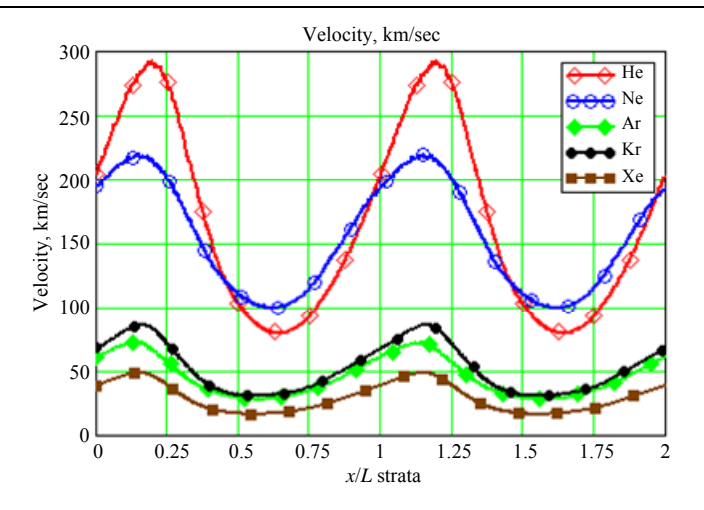


Fig. 3. Dependence of electrons drift speed

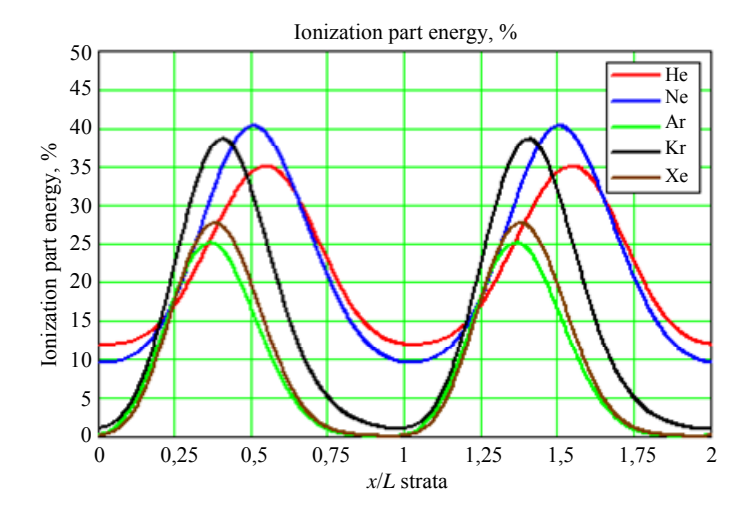


Fig. 4. Share of energy spent on ionization

Analysis of the tabular data of the electronic component of the gas-discharge plasma properties in inert gases with the same pressure and current shows that the field inhomogeneity is most strongly manifested in the discharge characteristics caused inelastic processes: atoms excitation and their ionization. For light inert gases (helium and neon) the influence of stratification on the ionization and luminosity is insignificant about 1% but the drift speed and average electrons energy in the stratified discharge is significantly lower – by dozens %. For heavy inert gases this situation changes radically. The main part of energy is used on atoms excitation and in the volumetric luminescence (characteristic for the discharge type) and it leaves the plasma in the form of radiation. Drift speed in the homogeneous field is higher for all gases; it is

most pronounced for light gases without Ramsauer effect – helium and neon. Field non-uniformity practically does not affect the wall potential value.

On gas heating

Joule heat is partially used to heat the gas. Assuming that all the energy is spent on heating the gas and is dissipated by thermal conductivity through quartz walls of the gas discharge tube, we obtain an upper estimate for the heating of the tube internal surface $\Delta T_{\text{wall}} = i < E > \Delta R_{\text{tube}} / 2\pi R \lambda_{\text{glass}}$ value: (Wall $\Delta R_{\text{tube}} = 1 \text{ mm}, \text{ quartz}$ thickness thermal conductivity $\lambda_{glass} = 1.32 \text{ W/m} \text{ deg.}$). The corresponding values ΔT_{wall} are given in table 3 and they make up a small part of K degree.

To estimate the gas heating, we shall use the well-known solution of the thermal conductivity equation for the dependence of the gas temperature on the ratio: $\frac{1}{r}\frac{d}{dr}\left(r\lambda\frac{dT}{dr}\right) = Q(r), \text{ where } Q(r) - \text{ is a power}$

released in the form of heat per volume unit [2]. In the approximation of a parabolic relation, the $Q(r) = Q(0)(1-r^2/R^2)$ and $\lambda(r) = \lambda_0 = \text{const}$ has the following form:

$$T(r) = T(R) + \frac{3}{16} \frac{Q(0)}{\lambda} R^2 \left(1 - \frac{4}{3} \frac{r^2}{R^2} + \frac{1}{3} \frac{r^4}{R^4} \right).$$
 The

average energy transfer from electrons to atoms across the tube cross-section is equal to

$$=2\int_{0}^{R}Q(0)(1-r^{2}/R^{2})2\pi rdr/\pi R^{2}=\frac{1}{2}Q(0).$$

Using data from table 2 on the share of energy loss for excitation and ionization, we obtain an estimate for heating of gas atoms in the center of the rube:

$$\Delta T(0) = T(0) - T(R) = 3ieE(1 - \alpha_{rad} - \alpha_{ion}) / 8\pi\lambda.$$

Values given in table 3 $\Delta T(0)$ for the case of a periodic field in the model with wall show that the heating of gas in tube is several degrees. Electrons density N_e is determined using the ratio $i = eN_eW\pi R^2$.

Table 3

Characteristics of the stratified gas-discharge plasma in the tube

Gas	Не	Ne	Ar	Kr	Xe
Field, V/cm	8.5	6	4.5	7	5
Reduced field, Td	78.1	55.2	41.4	64.4	46.0
Strata period, cm	2.9	3.6	3.5	2.0	2.4
Wall potential, V	40.0	32.0	17.0	16.7	13.0
Electron temperature, eV	5.82	6.46	4.02	3.48	2.82
Ion temperature, K	1072	662	377	429	344
Upper limit gas heating, K	0.3	0.7	0.5	2.5	1.7
Upper limit wall heating, ΔT_{wall} , K	0.015	0.010	0.008	0.012	0.009
Free length Atom, m.f.p. mkm	940	800	560	490	420
Debue length, Electron, mkm	813	904	676	381	254
Debue length, Ion, mkm	102	85	61	39	26
Plasma density, 1/cm**3	2.4E8	2.2E8	7.6E8	6.6E8	1.2E9

General characteristics of the gasdischarge plasma in Table 3 correspond to the case of electrons drift in the periodic fields for model with wall which are most adequate to the conditions of current flow under the experiments [1].

On cathode heating and sputtering

In [1] the nickel cathode undergoes ionic bombardment with inert gas ions which cause its heating and sputtering. A simple assessment for the nickel cathode with a weight of 10 g at a current of 1.5 mA results

in temperature increase by 1 K during over a time of about 1 s. However, the hollow cathode effectively cools down due to the small distance (about 1 mm) to the tube walls, therefore, tube walls near the cathode can noticeably heat up. A more detailed consideration of this important issue is beyond the scope of this work.

After the discharge ignition the consecration and, consequently, the influence of sputtered metal atoms on the plasma characteristics is proportional to the discharge combustion time, i.e. the number of sputtered metal atoms ΔNme_{Me} in the tube is proportional to the sputtering coefficient,

bombarding ions flux and bombardment time: $\Delta N_{Me} = \gamma(i/e)\Delta t$. For a nickel cathode with a sputtering coefficient of $\gamma = 0.7$, tube volume of about 1 1 and current of 1.5 mA, the impurity concentration of 1% will be achieved in about 20 s. The appearance of nickel atoms in the working gas with a fraction of 1% leads to the fact that metal ions make up a significant part of ion component (see [14, 15], where the influence of admixture of iron atoms in helium and mercury in argon on the discharge is considered). The point of the above rough estimation of the running time of one percent of the impurity in the experiment [1] is that a significant proportion of the impurity can be achieved for less than a minute. As the impurity develops, a reverse mechanism of its removal will activate (for example, due to the cathode alloying with impurity ions) and a certain balance will be established between the concentrations of the impurity and working gas). As the impurity concentration was not estimated in [1], all the results for electrons drift calculation in Table 2 are given for pure gases.

In a sealed tube, as the proportion of metal atoms in the inert gas increases, they begin to influence not only the positive column plasma characteristics but the gas pressure. Our estimates show that with energy deposition parameters of 1 W characteristic to these experiments with dusty plasma, gas heating inside the tube is insignificant (see table 3), so the increase in gas pressure (indicator measured directly during the experiment) is due to the impurity component and gas heating in the cathode fall region.

Conclusion

The characteristics gas-discharge plasma in this work can be used for more accurate determination of dust component characteristics in the experiments with dusty plasma [1]. Moreover, using the similarity parameters pR and i/R these data can be

useful to estimate the characteristics of avalanche and spark discharge to determine the characteristics of transfer from avalanche to spark discharge and for determining the plasma characteristics in the streamer channel [3, 4, 16, 17].

The authors express gratitude to V. I. Kolbov for useful discussions on the application of similarity parameters when analyzing different types of gas discharge.

REFERENCES

- 1. Dzlieva E. S., Karasev V. Yu., Novikov L. A., Pavlov S. I., Golubev M. S. and Mashek I. Ch., Technical Physics **68** (10), 1328–1332 (2023).
- 2. Granovsky V. L., Electric current in gas. Steady-state current. Moscow, Nauka, 1971 [in Russian].
- 3. Bazelyan E. M. and Raiser Yu. P., Spark discharge. Moscow, Publishing House of Phys.-Techn. Institute, 1997 [in Russian].
- 4. Lozansky E. D. and Firsov O. B., Theory of the spark. Moscow, Atomizdat, 1975 [in Russian].
- 5. Polyakov D. N., Shumova V. V. and Vasilyak L. M., Plasma Physics Reports **43** (3), 397–404 (2017).
- 6. Mayorov S. A., Plasma Physics Reports **35** (9), 802–812 (2009).
- 7. Novac M., Czech. J. Phys. B, No. 10, 954–959 (1960).
- 8. Kolobov V. I. and Arslanbekov R. R., Phys. Rev. E **111**, l015203–17 (2025).
- 9. Golubovsky Yu. B., Kudryavtsev A. A., Nekuchaev V. O., Prokhorova I. A. and Tsendin L. D. Kinetics of electrons in nonequilibrium gas-discharge plasma. SPb., Publishing house of St. Petersburg University, 2004.
- 10. Mayorov S. A., Bulletin of the Lebedev Physics Institute **40** (9), 258–264 (2013).
- 11. Kodanova S. K., Bastykova N. Kh., Ramazanov T. S. and Mayorov S. A., Ukr. J. Phys. **59** (4), 371–374 (2014).
- 12. Maiorov S. A. and Golyatina R. I., High Temperature, No. 4 (2025) (in press).
- 13. Maiorov S. A., Golyatina R. I., Kodanova S. K. and Ramazanov T. S., Plasma Physics Reports **50** (8), 1029–1041 (2024).
- 14. Golyatina R. I. and Mayorov S. A. Applied Physics, No. 5, 33–27 (2011) [in Russian].

- 15. Golyatina R. I., Maiorov S. A., Ragimkhanov G. B. and Khalikova Z. R., Physical Sciences and Technology **7** (1), 15–18 (2020).
- 16. Kurbanismailov V. S., Golyatina R. I., Maiorov S. A., Ragimkhanov G. B., Khalikova Z. R.
- and Ramazanov I. G., Applied Physics, No. 4, 24–31 (2020) [in Russian].
- 17. Kolobov V. I. and Golubovskii Y. B., Plasma Sources Sci. Technol. **31**, 094003 (2022).

About authors

Sergey Alekseevich Mayorov, doctor of physics and mathematics, leading research scientist, Joint Institute for High Temperatures of the Russian Academy of Sciences (Russia, 125412, Moscow, 13, Izhorskaya st., bldg. 2). E-mail: mayorov_sa@mail.ru SPIN-code 9331-1751, Author ID 24761

Rusudan Igorevna Golyatina, research scientist, Prokhorov General Physics Institute of the Russian Academy of Sciences (Russia, 119991, Moscow, Vavilova, 38). E-mail: rusudan@intemodino.com Author ID 28890

Elena Savonovna Dzlieva, Candidate of Physical and Mathematical Sciences, senior research scientist, Saint Petersburg State University (Russia, 199034, Saint Petersburg, Universitetskaya embankment, 7/9). E-mail: plasmadust@yandex.ru

Viktor Yuryevich Karasev, doctor of physics and mathematics, professor, Saint Petersburg State University (Russia, 199034, Saint Petersburg, Universitetskaya embankment, 7/9). E-mail: plasmadust@yandex.ru SPIN code 4423-2530, Author ID 31685

= PHYSICAL SCIENCE OF MATERIALS=

UDC 621.315.592 PACS: 81.10-h

Metrological support of digital measurements of images of etch pit inhomogeneity in GaAs single crystals

© N. Y. Komarovskiy^{1,2,*}, S. N. Knyazev¹, E. A. Sokolovskaya², A. V. Kudrya², A. S. Sukhanova^{2,3}, V. E. Antonova^{2,3} and E. V. Molodtsova¹

¹ Sazhin Giredmet JSC, Moscow, 111524 Russia *E-mail: nickkomarovskiy@mail.ru ² University of Science and Technology MISIS, Moscow, 119049 Russia ³ RD&P Center ORION, JSC, Moscow, 111538 Russia

> Received 2.06.2025; revised 1.07.2025; accepted 11.08.2025 Scientific specialty code: 2.2.3, 2.6.1

An analysis of the brightness field of panoramic images of the dislocation structure of GaAs (100) single crystals grown by the Czochralski method was performed. The binarisation threshold algorithm was selected based on the patterns of brightness field formation. Differences in the distribution of pixel brightness values (in 256 shades of grey) were evaluated by the values of asymmetry and excess coefficients. It was shown that when individual frames are stitched together, a characteristic 'dark frame' may form at the points where individual frames overlap. It has been established that, given the asymmetric nature of the distribution of experimental samples of measurement results for structural elements, the assessment of their differences or similarities according to the Student's and Smirnov's criteria may not coincide.

Keywords: Czochralski method; GaAs; etching patterns; dislocations concentration; light microscopy; digital image processing.

DOI: 10.51368/1996-0948-2025-4-59-67

1. Introduction

addition demand for In to semiconducting single crystals, development of solid-state electronics also justifies the requirements to growing their quality, including the density of structural defects dislocations [1]. The effect of dislocations on electrophysical parameters of the integrated circuit is ambivalent: on one hand, they create additional levels in the band gap; on the other hand, they are a sink of point defects [2]. Dislocations concentration level (N_d) in case of growth according to Czochralski method is foremost determined by the value of thermoplastic deformation relaxation, and lays within N_d : 10^2 (InSb) ... 8×10^4 cm⁻² (GaAs) interval for semiconducting compounds of AIIIBV group [3, 4].

ASTM standard provides for determination of dislocation density with the use of optical light microscopy in 9 fields of view, location of which considers the specific features of temperature gradients during growth (Fig. 1). It is not clear to which extent it is consistent with the dislocation structure of a single crystal as a whole, since there is no

idea regarding the required scope of measurements (the number of the reviewed fields) and criteria for choosing arrangement thereof, which is critical to obtain reproducible and consistent results.

Mass observations of dislocations on the sample scale with the use of light and electron microscopy methods (followed by determination of their concentration, regularity of arrangement within a viewing field) are complicated due to high labor

intensity [5]. Digital transformation of the structures measurement process should allow for proceeding from local measurements to intrinsic measurements on a sample (plate) scale and assessment of non-uniformity of etching pits arrangement. This approach has already proved its efficiency and relevance in studying other materials [6], but the efficiency for assessment of dislocation structure of single crystals of A^{III}B^V group is not evident.

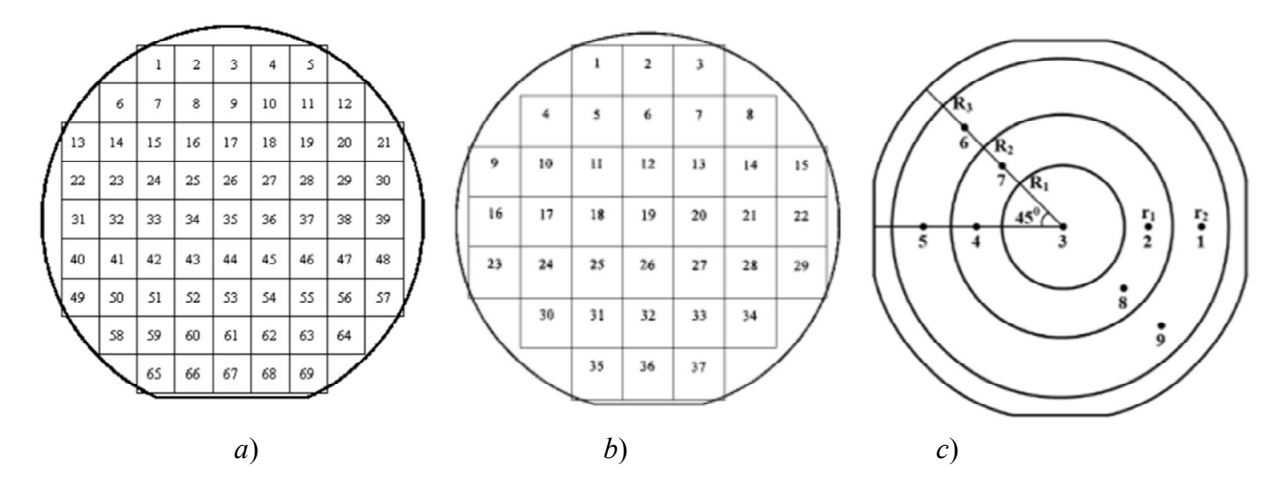


Fig. 1. Fig.1 Diagram for choosing fields of view according to SEMI M36-0699 ASTM 1404-92 requirements for single crystals with the diameters of (a) 50 mm, (6) 76 mm and ASTM 1404-92 (c) [7, 8]

The objective of this work is to assess the possibility to use the advanced digital image processing methods for development of the traditional method of preferential etching and quality assessment of single crystals of GaAs, based on the need to improve assessments objectivity, particularly by virtue of extending the parameters, which characterize their dislocation structure.

2. Study object

GaAs single crystals alloyed with Te, 40 mm in diameter, were grown with the use of Czochralski method with liquid encapsulation of (LEC) molten mass in crystallographic direction [100]. The plates cut perpendicularly to the growth axis on the

disk-cutting machine were used as the samples. The plates surfaces were machined, chemically polished in acid solution with the following ratio – H₂SO₄: H₂O₂: H₂O (3:1:1) and preferentially etched in KOH alkali melt at 450°C within 7 minutes [6,10].

The pan views of dislocation structures on GaAs plates obtained on Axio Observer D1m Carl Zeiss microscope with 50-fold magnification by virtue of individual frames linking in Thixomet [10] software package was used as the study object.

3. Justification for choosing the binarization limit

On the grayscale pan digital view of the dislocation structure (Fig. 2), each pixel is

consistent with its own value of brightness intensity I (0 to 255), which determines the brightness field of the view in general. The lower (as compared to the light background) brightness level corresponds to the dislocation etching pits. Thus, it is possible to represent

the view in a binary form (matrix of 1-0 type, where 0 corresponds to a pit, and 1 corresponds to the background) and further measure the pits geometry (including their arrangement on the thin section) on the studied plate scale (Fig. 2).

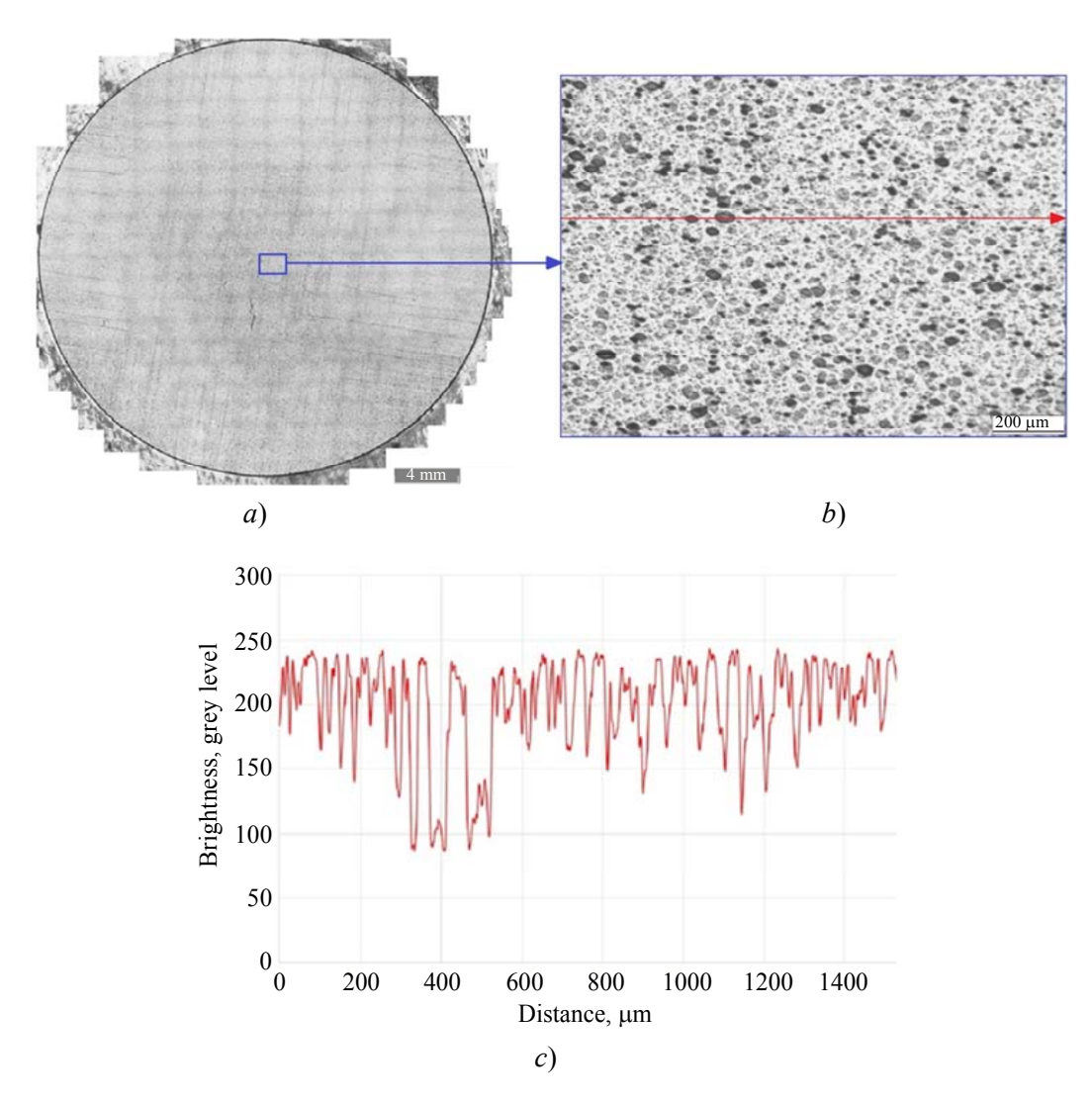


Fig. 2. Pan view of etching pits in GaAs (100) (a), including larger magnification (b); distribution of pixels brightness (c)

However, the occurrence of additional brightness field anomalies, particularly related to formation of a darker "mesh" in the areas of individual frames superimposition under their cross-linking, is possible when creating the pan view (see Fig. 2a). The scope of accompanying distortions of the image brightness field was assessed by comparison of distribution of the brightness intensity values within the mesh framework and the cells (frames) thereof: 1–4 (Fig. 3).

The differences in the form of the pixels brightness intensity values distribution within cells and framework were found, which is confirmed by the values of asymmetry and excess coefficients. The lighter level of the cell was consistent with a larger deviation of asymmetry coefficients from zero (normal distribution sign) - left-side asymmetry $(A_s = -0.82...-0.84)$, with a sharp distribution spike close to a normal distribution $(E_s = -0.05...-0.09)$. For distribution of the

framework excess coefficients, A_s to E_s ratio was opposite: -0.45...0.49 and -0.57...-0.78, respectively.

The difference of average values of pixels intensity in framework and cell was notable: $159 \pm 43...169 \pm 39$ and $180 \pm 42...184 \pm 42$ respectively. Despite overlapping the fields of average values errors by samples, the significance of difference was confirmed by the results of testing the hypothesis based on Student criterion, its experimental values of $t_{\rm exp.}$ were at least 2.585, which exceeded its tabular value $t_{\rm tab.} = 2.021$ at the risk level $\alpha = 0.05$ (sample size was 3600 pcs).

Such difference in brightness fields of individual fragments of the pan view would

inevitably complicate the choice of binarization criteria. Due to its "meshed" configuration, the difficulties would occur even in the use of the most common criterion—by the level of visual consistency of initial and binary images. Apparently, the intrinsic choice of the binarization level should consider the regularity of the studied views brightness field formation. To this end, the secant lines were drawn within the background and the pits, respectively. The histograms of individual pixels brightness intensity values distribution corresponding to etching pits on GaAs (100) surface and the background (for the mesh framework and cell) were compared in the unified coordinates (Fig. 4.)

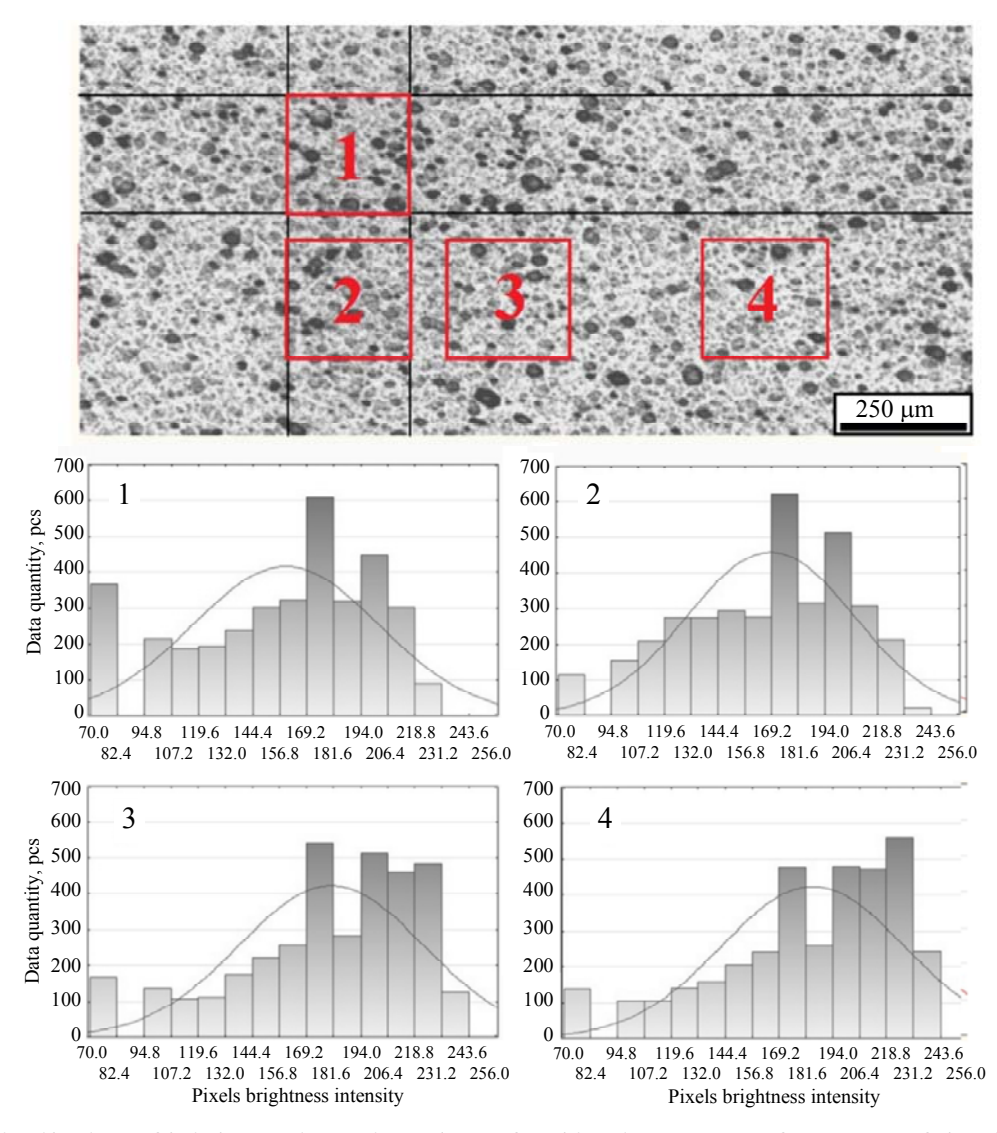


Fig. 3. Distribution of brightness intensity values of etching images on 4 fragments of the viewing field (1 and 2 – mesh framework, 3 and 4 – cell thereof) of GaAs (100) surface

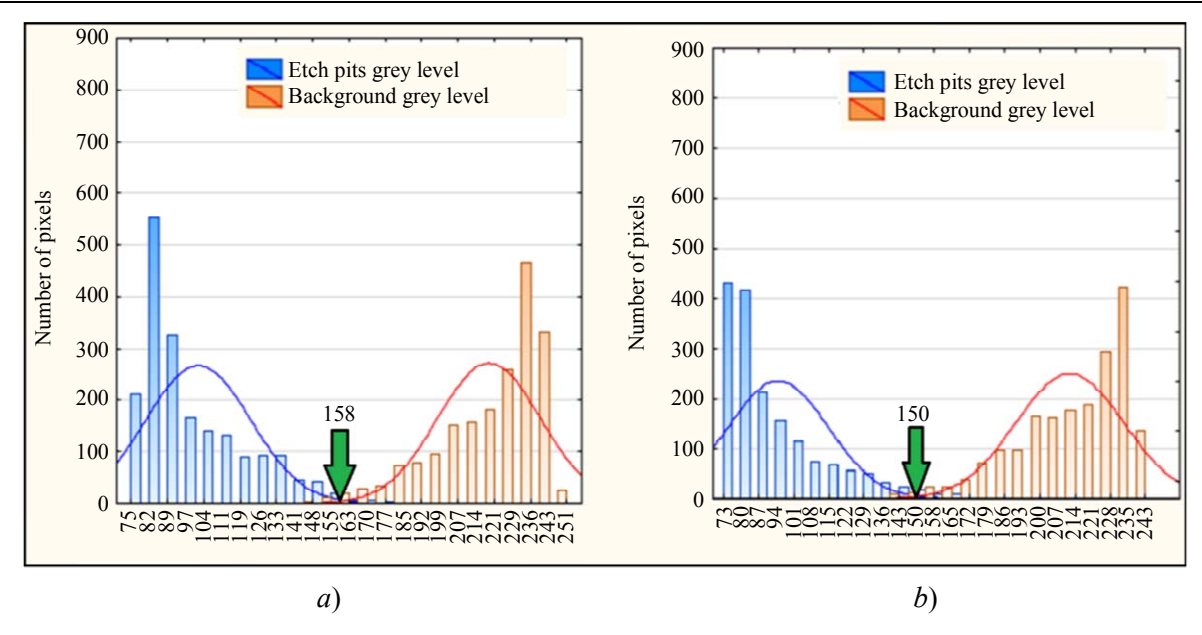


Fig. 4. Distribution of brightness intensity values in grey scale for pits and background within the mesh cell (a) and framework (b)

It is demonstrated that intersection of of the histograms brightness values distribution of background and pits in cell and framework corresponds to the brightness of 150 and 158 interval grey units. respectively. It apparently retains binarization limit value to be determined. To identify the limit value (contrast) within this interval univocally, the image fragments "cut" from the panorama frame and cell were converted into a binary form, at the contrast level compliant with median and boundary values of the found interval of the shades of gray – 150, 154, 158 (Fig. 5).

The obtained binary images were consistent with the histograms of areas

distribution of dark objects – etching pits (Fig. 6).

It was determined that distribution of the values of average areas of the dark objects in cells and framework, same as distribution of their lamination intensity, differ from each other. The lighter level of the cell was consistent with the largest deviation of asymmetry coefficients from zero - right-side asymmetry $(A_s = 3.27...2.88)$ and high peakedness that was reduced with an increase of binarization limit ($E_s = 12.18...9.63$). A_s to E_s ratio for distribution of the values of excess coefficients of the dark framework objects opposite: 2.16...2.73 was 4.82...7.98, respectively.

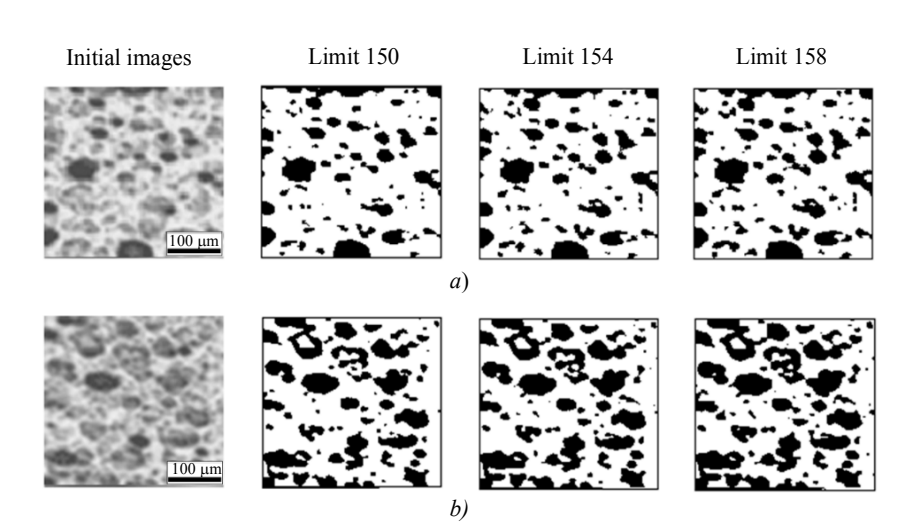


Fig. 5. Effect of differences in binarization limit level on etch pits morphology after limit binarization: fragments of the cell (a) and the framework (b) of the pan view

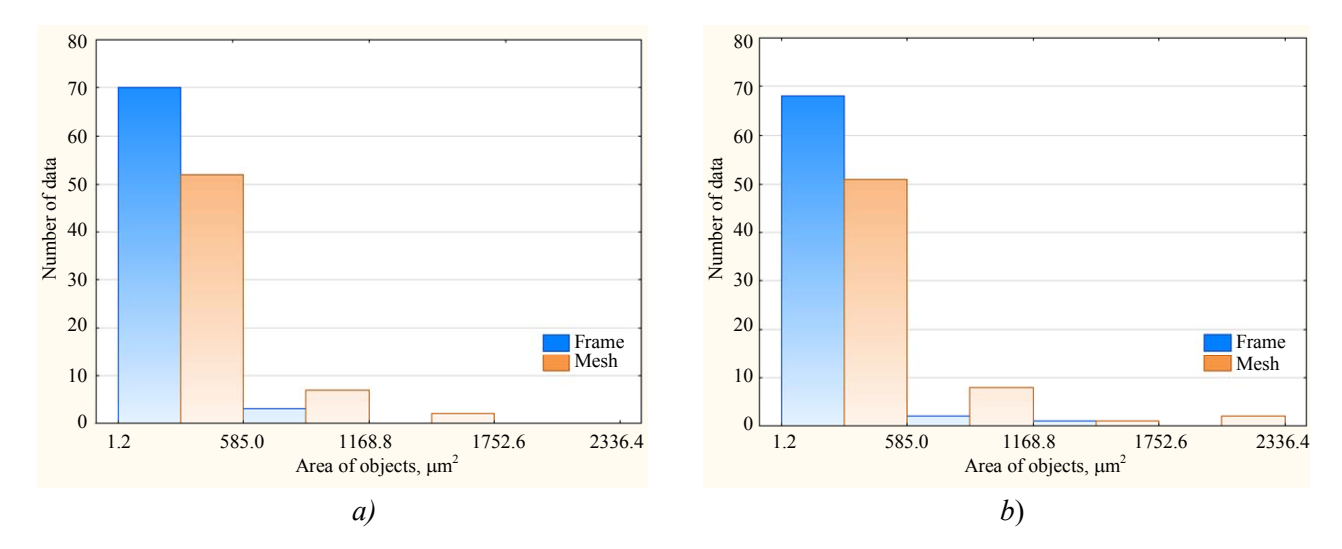


Fig. 6. Histograms of distribution of the values of areas of dark objects pegged to fragments of cells and framework of the pan view of etch pits on thin section at binarization limit of 150 (a) and 158 (b) shades of grey

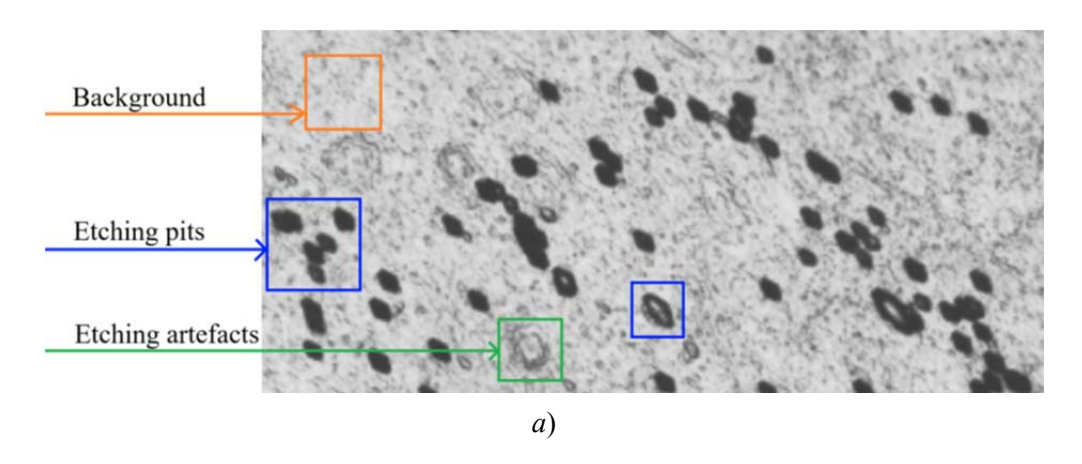
Due to high asymmetry of experimental distribution under samples testing hypotheses on their difference or similarity, the use of their average values (and Student criterion, respectively) may occur to be incorrect. Thus, for example, in our case, the studied samples fall under the $(t_{\rm exp} < 0.722;$ population $t_{\rm tabl} = 1.98$; $\alpha = 0.05$). However, the use of nonparametric Smirnov criterion non-depending on the distribution type [11] resulted in an opposite conclusion: its experimental values $t_{\rm exp}$ were not lower than 2.116, which exceeded the tabular value $t_{\text{tab.}} = 1.358$ at the risk level $\sim = 0.05$ (sample α 70). This circumstance should be considered under digital measurement of structures in materials science where the type of distribution of some parameters of the structure geometry deviates from standard (symmetrical) type quite often.

As it follows from the obtained results, the successive increase of the binarization limit from 150 to 154 and to 158 shades of grey is accompanied with two processes: formation of new dark objects due to achievement of their lower boundary of brightness intensity and increase of dimensions, a range of already existing objects, with a possibility to combine some of them into one. Therewith, as follows from

Fig. 6, the number of large etch pits (with an area exceeding $900 \mu m^2$) from among their total number was not high– less than 1.8 %, but therewith a black share taken by them for cell and framework amounted to 9–14 and 7–11 %, respectively.

It was established that in addition to etch pits and background, the studied images have etching artefacts (Fig. 7a) which occurrence may be related to defects emerging during abrasive finishing of the plate surface.

When comparing the brightness intensity of individual structural components, it comes out that the etching artefacts have an intermediate position in terms of brightness intensity between etching pits background. Reduction of the binarization limit from 158 to 150 shades of grey facilitates their transition to the background, resulting in significant reduction of dark objects on the view, which creation is related to mechanical processing of the plate surface. In addition, the lower binarization level reduces a possibility of merging the adjacent pits, which are mostly located in the dark framework, which makes the measurements of the number of pits in framework and cells compatible. Further reduction binarization limit value (below 150 shades of grey) can result in violation of etching pits contour integrity, which may significantly change their morphology and distribution statistics. These circumstances determined the choice of the binarization level of the binary view as a whole, equal to 150 shades of grey.



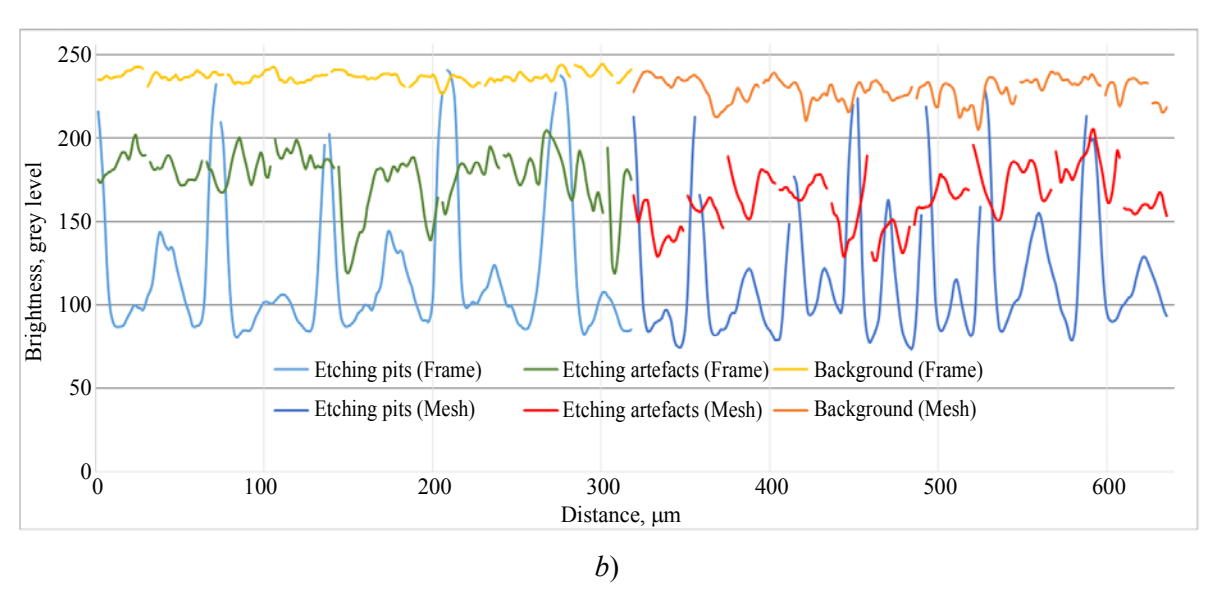


Fig. 7. Pixels brightness intensity of individual structural components (a) along secant lines drawn through etching pits and artefacts and background, respectively (b)

It is obvious that the registered objects with a size of 1.2 to 585 μ m² likely have non-dislocation nature [9]. Such objects are nothing more than a noise on the studied image, it can be eliminated by filtration. Elimination of the dark objects with an area equal to or below 585 μ m² on the image reduced the amount thereof 6 times and increased the large pits contribution into creation of the black area for cell and framework up to 42 and 45 %, respectively.

It should be noted that the etching pits which contour differed from the correct diamond-shaped facet on the binary view are also the matter of interest and not considered "artefacts" of digital processing of optical images.

Conclusion

The algorithm for choosing the binarization threshold, based on the grey level

distributing values consistency, corresponding to etching pits and background within unified coordinates (in individual frames which are a part of the panorama cell and framework – the points of frames superimposition), the level of which amounted to 150 shades of grey, developed for GaAs (Te) etching pits images linked into the panorama (option of Thixomet Pro software) in 256 shades of grey.

Based on the statistics of distribution of the dark objects areas for the pan view of the binary image under study in the work, the noises filtration threshold was determined to be $585 \mu m^2$. Elimination of such dark objects reduced the amount thereof 6 times and increased the large etching pits contribution into creation of the black area for cell and framework of pans up to 42 and 45 %, respectively.

Definition of thresholds of binarization and noise filtration increase the accuracy of application of modern methods of digital processing of images when assessing the structural perfection of GaAs single crystals during the study of dislocation density on a sample scale by light and electron microscopy methods.

REFERENCES

- 1. Subramanyam N. and Tsai C. T., Journal of materials processing technology **55** (3–4), 278–287 (1995). doi: 10.1016/0924-0136(95)02018-7
- 2. Frigeri C., Weyher J. L., Jimenez J. N. and Martin P., Journal de Physique III, No. 12, 2339–2360 (1997).
- 3. Elliot A. G., Wei C. L. N. and Vanderwater D. A., Journal of Crystal Growth. **85** (1–2), 59 (1987).
- 4. Yu H. Y., Zhao Y. W., Zhan R., Gao Y. L. N. and Hui F., J. Semicond. **29** (9), 1775 (2008).
- 5. Sokolovskaya E. A., Kudrya A. V., Kodirov D. F. ugli, Sergeyev M. I., Budanova E. S. N. and Samoshina M. E., Metallurgist **68**, 38–44 (2024).
- 6. Kudrya A. V., Sokolovskaya E. A. N. and Tang V. F., Russian metallurgy (Metally) **2022** (10), 1318–1331 (2022).
- 7. SEMI M36-0699 Test Method for Measuring Etch Pit Density (EPD) in low dislocation density Gallium Arsenide wafers
- 8. Test Method for Crystallographic Perfection of Gallium Arsenide by Molten Potassium Hydroxide (KOH) Etch Technique ASTM F1404–92
- 9. Sangwal K. Etching of crystals: theory, experiment and application. Elsevier, 2012
 - 10. http://www.thixomet.com/
- 11. Journal of the American Statistical Association **46** (253), 68–78 (Mar., 1951).

About authors

Nikita Yuryevich Komarovsky, Head of the research group of the laboratory of high-temperature semiconducting compounds of A^{III}B^VV group, Sazhin Giredmet JSC (111524, Russia, Moscow, Electronnaya St.2, bldg. 1). University of Science and Technology MISIS (119049, Russia, Moscow, Leninsky Prospekt, 4, bld. 1). E-mail: nickkomarovskiy@mail.ru NYKomarovsky@rosatom.ru https://orcid.org/0000-0002-7869-7886 Scopus Author ID 58510893300. Web of Science Researcher ID NRX-9045-2025. SPIN code 9642-8920

Stanislav Nikolaevich Kniazev, Ph.D. of Technical Sciences, Head of Laboratory, Sazhin Giredmet JSC (111524, Russia, Moscow, Electronnaya St.2, bldg. 1).

Elina Aleksandrovna Sokolovskaia, Candidate of Technical Sciences, Associate professor of the Department of the Metallurgical science and Physics of strength, University of Science and Technology MISIS (119049, Russia, Moscow, Leninsky Prospekt, 4, bld. 1). E-mail: sokolovskaya@misis.ru ORCID 0000-0001-9381-9223. Web of Science Researcher ID AAM-6419-2021. Scopus Author ID 15077468100. SPIN code 2633-6344. Author ID 185426

Aleksandr Viktorovich Kudria, Candidate of Technical Sciences, Holder of chair ad interimr of the Department of the Metallurgical science and Physics of strength, University of Science and Technology MISIS (119049, Russia, Moscow, Leninsky Prospekt, 4, bld. 1). E-mail: AVKudrya@misis.ru ORCID: 0000-0002-0339-2391. Web of Science ResearcherID GWZ-8579-2022. Scopus AuthorID 6603628218. SPIN code 6497-2109. Author ID 11030

Anna Sergeevna Sukhanova, engineer, University of Science and Technology MISIS (119049, Russia, Moscow, Leninsky Prospekt, 4, bld. 1). RD&P Center ORION, JSC (111538, Russia, Moscow, Kosinskaya st., 9). E-mail: sukhanova11@mail.ru SPIN code 3007-4250. Author ID 1245396

Valeria Evgenievna Antonova, Engineer Cat. 2, (119049, Russia, Moscow, Leninsky Prospekt, 4, bld. 1). (111538, Russia, Moscow, Kosinskaya st., 9). E-mail:avaleriya98@mail.ru

Elena Vladimirovna Molodtsova, Candidate of Technical Sciences, Leading Research Scientist of the laboratory of high-temperature semiconducting compounds of A^{III}B^VV group, Sazhin Giredmet JSC (111524, Russia, Moscow, Electronnaya St.2, bldg. 1).

PHYSICAL SCIENCE OF MATERIALS :

UDC 620.197.5+ 57.087.1+ 57.033 PACS: 68.90.+g, 43.80.-n

EDN: BRHCIM

Long-term field tests of corrosion and biofouling of stainless steel samples in a tropical climate

© V. Ya. Pecherkin^{1,*}, E. A. Deshevaya², L. M. Vasilyak¹ and C. V. Fialkina²

¹ Joint Institute for High Temperatures of Russian Academy of Sciences,
Moscow, 125412 Russia

* E-mail: vpecherkin@yandex.ru

² Institute of Biomedical Problems of Russian Academy of Sciences,
Moscow, 123007 Russia

Received 18.04.2025; revised 13.05.2025; accepted 11.08.2025 Scientific specialty code: 1.3.21

In a tropical climate, stainless steel samples were tested at various test sites for their biofouling. After being exposed for 18 months in outdoor areas near the cities of Ho Chi Minh City, Hanoi, Nyagang in Vietnam, significant corrosion and biofouling spots were found on samples placed in outdoor grass sites, and minor impacts on samples placed in indoor mycological sites.

Keywords: stainless steel; microorganisms; bacteria; mold fungi; corrosion; biocorrosion; biofouling.

DOI: 10.51368/1996-0948-2025-4-68-73

Introduction

The operational reliability of technical products is determined by the materials ability to withstand external environmental factors, which naturally include chemical and biological elements. Stainless steels typically exhibit excellent resistance to chemical and biological corrosion and function effectively in a wide range of environments. The corrosion resistance limit of a specific grade of stainless steel is influenced by the elements that make up its composition. As a result, each brand exhibits a different response when exposed to corrosive environment. Stainless steel corrosion may be caused by a disruption in the chemical composition of the surface layer, exposure to

corrosive environments, and mechanical damage. The main types of corrosion include pitting corrosion, general corrosion, intercrystalline corrosion, erosion corrosion, and galvanic corrosion [1]. The cumulative impact of aggressive factors can significantly increase the corrosion and degradation rate [2–4]. When in contact with other metals and in the electrolytes presence, stainless steel may experience galvanic corrosion [5].

Biofouling can also cause biodeterioration of stainless steels and products, which can lead to the performance properties loss. Under natural conditions, new active strains of degrading fungi frequently emerge across different climatic zones, including both forests and open spaces. Their activity, growth rate, quantity, and

composition are influenced by the climatic conditions. Harmful biological factors encompass bacteria and fungi, particularly in tropical climates, where fungi, specifically micromycetes, play a predominant role in biofouling and the degradation of materials [6–11]. Microorganisms growing on the materials may cause damage through their waste products [12, 13].

There is currently shortage a of organized quantitative data on the biodeterioration processes affecting technical elements in operating conditions, and reliable methods for diagnosing and predicting the metals durability and their structures in interaction with living organisms have yet to be developed. The impact of non-biological factors on technical objects, including chemically corrosive substances, temperature, mechanical stress, light radiation, etc., has been thoroughly studied. However, characteristics and patterns of influence of biological factors have not been thoroughly studied. Researchers primarily concentrate on the ecological and biological aspects of the issue [14].

The objective of this work is to conduct a long-term study into the resistance of unprotected stainless steel samples to biofouling by microorganisms under field conditions in both open and closed environments in a tropical climate.

Experimental section

For the research, thirty samples of 12X18N10T stainless steel, each measuring $50 \times 50 \times 1$ mm, were produced. Samples underwent mycological testing under tropical climate conditions near Ho Chi Minh City, Hanoi and Nyagan, Vietnam. **Testing** occurred at open grassy areas and sheltered stations protected from direct sunlight and precipitation. Each sample was secured to the bench tester with black-painted metal clips. Figure 1 shows a photograph of the sample exhibition stands used for testing near Ho Chi Minh City.





Fig. 1. Exhibition stands near Ho Chi Minh City. a) – open grassy area, b) – box protected from precipitation and wind at the mycological site

In open grassy areas, samples were exposed to ambient temperature, humidity, and light-UV radiation conditions typical of Samples region of Vietnam. that mycological testing areas were placed inside non-hermetic boxes to provide protection from precipitation and wind. The boxes were protected from direct sunlight by forest vegetation. Each sample was secured with special metal fittings. The continuous exposure time of each sample was 18 months.

Following exposure, each sample was placed in individual sterile bags and transported to the microbiology laboratory for testing. Each sample was processed in a laminar box and placed in a sterile, square Petri dish. The samples were then observed under a Stemi 2000 stereomicroscope (Zeiss) through the sealed Petri dish. Fouling of the samples was assessed using the 6-point scale outlined in GOST 9.048-75 [15, 16]. Table 1 shows the sample surface inspection results.

Table 1

Evaluation of fungal growth on sample surfaces after exposure (points)

Mate	rial/test location	Degree of mold fungi development (point): on sample/on fitting	Surface inspection result
Stainless steel,	Nyagan, open area	0	No fungal growth detected
12X18H10T	Nyagan, mycological site	0	No fungal growth detected
	Hanoi, open area	0/2	Fungal growth is visible on the sample fitting
	Hanoi, mycological site	0	No fungal growth detected
	Ho Chi Minh City, open area	0/2	Fungal growth is visible on the sample fitting
	Ho Chi Minh City, mycological site	0	No fungal growth detected

Rust spots were found at the attachment points of samples in open areas. Fungal growth occurred on and around rust spots where traces of corrosion were present.

inspection, Following the microbiological samples were collected from sample's surface in a Class microbiological box. This was done using a special sterile swab to determine the bacteria and fungi presence. Each swab was then placed in an individual test tube containing 5 ml of sterile saline solution and shaken on a Vortex mixer for at least two minutes. Then, a 1.0 ml aliquot of the solution was spread onto a solid nutrient medium. HiMedia's Potato Dextrose Agar Medium and tryptic soy agar were used for fungal and bacterial inoculation, respectively. Cultures in Petri dishes were incubated at 28 ± 1 °C for 2 days for bacteria and 5–7 days for fungi. After incubation period, the number of colony-forming units (CFU) was counted. Then, the grown bacteria and fungi were identified, if necessary. Table 2 shows the microbiological research results.

Table 2 The microbial content on the surface of the studied samples of stainless steel grade 12X18H10T after the exposure (CFU/cm^2)

No.	Sample testing site	Average number of microorganisms, CFU/cm ²	Average number of bacteria, CFU/cm ²	Average number of fungi, CFU/cm ²
1	Nyagan, open area	2.5×10^{0}	2.5×10 ⁰	0
2	Nyagan, mycological site	1.54×10^2	4.0×10^{0}	1.5×10^2
3	Hanoi, open area	9.45×10 ⁴	2.5×10 ³	9.2×10 ⁴
4	Hanoi, mycological site	3.4×10^4	3.3×10 ⁴	1.0×10^{3}
5	Ho Chi Minh City, open area	2.5×10 ⁴	3.9×10 ¹	2.5×10 ⁴
6	Ho Chi Minh City, mycological site	1.47×10^3	1.7×10 ²	1.3×10 ³

Samples without rust showed no fungal growth (Fig. 2, 3). On these samples, only fungal spore contamination was observed on the metal surfaces. The fungal species composition is characteristic of each site. Penicillium species dominate in mycological areas, whereas dark-colored fungi are predominant in open areas.

As shown in the figures, test samples installed in open grassy areas exhibited rust at their attachment points. The samples were secured with black-painted metal clips. The contact potential difference between stainless

steel and another metal may initiate oxidation processes, resulting in corrosion at the contact point. Furthermore, rust formation was observed only on samples exposed in open areas, while no rust spots were found in mycological areas across different zones of Vietnam. In open areas, meteorological factors likely damage the paint coating of the sample holder. This damage then initiates the corrosion of the sample metals and the holder due to the contact potential difference. An aggressive environment may further accelerate this corrosion.





Fig. 2. Photo of the surface of samples after open-site exposure in Hanoi

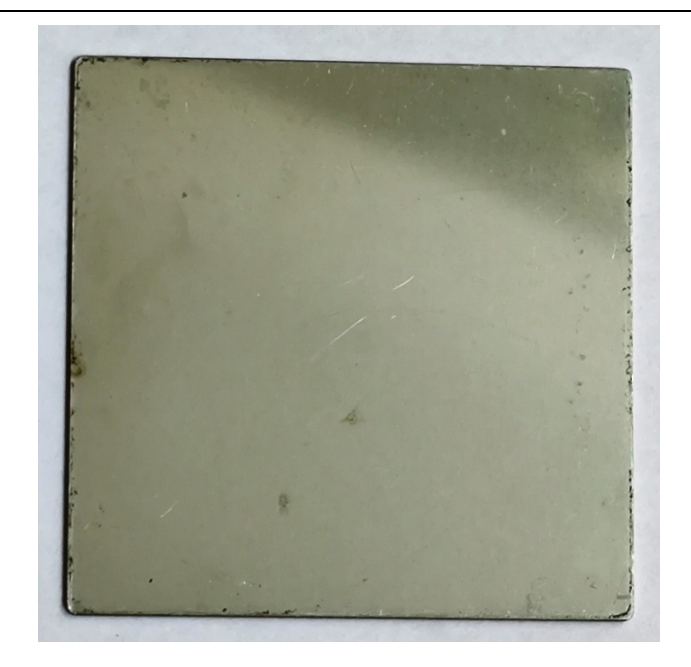




Fig. 3. Photo of the surface of samples after exposure at the mycological site in Hanoi

Therefore, to prevent corrosion under these conditions, contact between the metals should be avoided.

Conclusion

Field testing demonstrated that 12X18N10T stainless steel samples can be subject to chemical corrosion when in contact with other metals due to contact potential differences. In open areas, these corroded areas are prone to extensive fungal overgrowth.

The paper has been prepared with the support by the Ministry of Science and Higher Education of the Russian Federation (State Assignment No. 075-00269-25-00). Fungal strains were prepared, tests were conducted, and results were analyzed as part of research project FRFM-2024-0035. The methodology was developed using funds from the joint project Ekolan T-1.18.

REFERENCES

- 1. Balangao J. K., Journal of Chemical Health Risks **14** (1), 79 (2024).
- 2. Ikeda A., Morita Y. and Matsuki N., The Sumitomo Search **37**, 43 (1988).
- 3. Prakash T. L. and Malik A. U., Desalination **23**, 215–221 (1999).
- 4. Hoffmeister H., Corrosion, NACE International Corrosion Conference & Expo, 05476 (2005).
- 5. Chen L., Hu J., Zhong X., Yu S., Zhang Z., Zeng D. and Shi T., International Journal of Electrochemical Science, **12** (10), 9445–9455 (2017).
- 6. Alexandrova A. V., Sidorova I. I. and Tiunov A. V., Micologya and Phitopatalogya **1**, 12–25 (2011) [in Russian].
- 7. Alexandrova A. V. and Kalashnikova K. A. Modern Mycology in Russia, Moscow, National Academy of Mycology, 2012.
- 8. Kalashnikova K. A. and Alexandrova A. V., Mycology and Phytopathology **2**, 91 (2015) [in Russian].
- 9. Telegdi J., Shaban A. and Trif L., International Journal of Corrosion and Scale Inhibition **9** (1), 1 (2020).
- 10. Lugauskas A. Yu., Mikulskene A. I. and Shlyauzhene D. Yu., Catalog of micromycetes –

biodestructors of polymer materials. Moscow, Nauka, 1987 [in Russian].

- 11. Zhigletsova S. K., Rodin V. B., Kobelev V. S. et al., Applied biochemistry and microbiology **36** (6), 637–641 (2000).
- 12. Chugunov V. A., Martovetskaya I. I., Mironova R. I. et al., Applied biochemistry and microbiology **36**, 544–549 (2000).
- 13. Allsopp D., Seal K. J. and Gaylarde C. C., Introduction to Biodeterioration. UK, Cambridge,

Cambridge University Press, 2004.

- 14. Belov D. V. and Belyaev C. N., Galvanotehnika and obrabotka poverhnosty **30** (3), 4–21 (2022) [in Russian].
- 15. GOST 9.048-75. Materials and products. Methods of testing for microbiological resistance, Moscow, Publishing House of Standards, 1978.
- 16. Pecherkin V. Ya., Deshevaya E. A., Vasilyak L. M., Vasilyak S. L. et al., Applied Physics, No. 6, 60–65 (2023) [in Russian].

About authors

Vladimir Yakovlevich Pecherkin, Candidate of Physical and Mathematical Sciences, senior research scientist Joint Institute for High Temperatures of Russian Academy of Sciences (125412, Russia, Moscow, 13, Izhorskaya st., bldg. 2). E-mail: vpecherkin@yandex.ru SPIN code 4910-0417, Author ID 1089774

Elena Andreevna Deshevaya, Candidate of Biological Sciences, leading research scientist, Institute of Biomedical Problems of Russian Academy of Sciences (123007, Russia, Moscow, 76 a, Khoroshevskoe Highway). E-mail: deshevaya@imbp.ru SPIN code 3206-9869, Author ID 126892

Leonid Mikhailovich Vasilyak, Doctor of Physical and Mathematical Sciences, Senior Research Assistant, Joint Institute for High Temperatures of Russian Academy of Sciences (125412, Russia, Moscow, 13, Izhorskaya st., bldg. 2). E-mail: vasilyak@ihed.ras.ru SPIN code 5623-5167, Author ID 19599

Svetlana Vladimirovna Fialkina, Candidate of Biological Sciences, senior research scientist, Institute of Biomedical Problems of Russian Academy of Sciences (123007, Russia, Moscow, 76 a, Khoroshevskoye Highway). SPIN code 3967-0655, Author ID 168529

PHYSICAL SCIENCE OF MATERIALS

UDC 533.376 PACS: 85.30.-z

EDN: ZBLQDO

In situ Ga-doped mono- and polycrystalline Ge and GeSn films deposited by HW CVD

© V. G. Shengurov¹, A. M. Titova^{1,*}, N. A. Alyabina¹, S. A. Denisov¹, V. Yu. Chalkov¹, V. N. Trushin¹, A. V. Kudrin¹ and Yu. N. Buzynin²

¹Lobachevskii State University of Nizhnii Novgorod, Nizhnii Novgorod, 603950 Russia

* E-mail: asya_titova95@mail.ru

² Institute of Microstructure Physics of the Russian Academy of Sciences,
Nizhny Novgorod Region, Kstovo region, Afonino, 603087 Russia

Received 25.02.2025; revised 31.03.2025; accepted 11.08.2025 Scientific specialty code: 2.2.6

Mono- and polycrystalline Ge and GeSn films doped in situ with Ga atoms evaporated from a Ge:Ga source were grown by HW CVD on Si(100) and SiO_2/Si substrates. Their structural and electrical properties were studied using X-ray diffraction, Hall measurements, and CV-profilometry. During co-evaporation of the dopant from a sublimating Ge:Ga source in the vapor-phase deposition of Ge with the decomposition of GeH₄ on "hot wire", the incorporation of Ga atoms into the growing film was controlled by changing the substrate temperature from 300 to 500 °C on the ratio of Ga and Ge flows. To increase the Ga atom flux from the Ge:Ga source, a melt zone was formed in it, which made it possible to increase the hole concentration in the polycrystalline GeSn films to 5.4×10^{19} cm⁻³.

Keywords: epitaxy; polycrystalline films; GeSn; alloying.

DOI: 10.51368/1996-0948-2025-4-74-80

Introduction

GeSn solid solution films offer an alternative to post-silicon materials in optoand microelectronics due to their higher charge carrier mobility compared to Si and Ge. The addition of Sn to the Ge grate enables a direct band gap in the material, and also results in a higher effective mass and charge carrier mobility compared to Si and Ge. Polycrystalline GeSn films on dielectric substrates with high transport parameters are currently a focus of intense research due to their potential for creating diverse opto- and microelectronic devices. Polycrystalline GeSn films are essential for applications like three-dimensional integrations (3D DIs) and liquid crystal display (LCD) control matrices, where they serve as the only viable option. This is due to the fact that only the first layer deposited on a single-crystalline substrate can achieve a single-crystalline structure with

high electrophysical characteristics in 3D DIs. Depositing an insulating oxide or metal on this layer results in the formation of amorphous or polycrystalline structures in subsequent layers. A monocrystalline layer cannot be achieved on the amorphous glass substrates of a liquid crystal display. Polycrystalline GeSn films with high carrier mobility are fabricated on dielectric substrates by recrystallizing amorphous GeSn films using solid-phase crystallization (SPC) [1, 2], laser annealing [3, 4], or metal-induced crystallization [5, 6].

To enhance hole mobility in polycrystalline GeSn films, researchers aim to increase grain size, typically through solidphase crystallization (SPC). SPC involves prolonged annealing (450°C for up to 50 hours) in a resistance furnace under an inert gas atmosphere. Developing devices like 3D DIs and LCD control matrices requires a low-temperature process with a heat budget of 400°C for 2 hours. It ensures that the characteristics of electronic devices on the underlying films of 3D DI and LCD display substrates are not degraded.

Low thermal budget film deposition techniques are essential, among which the method of gas-phase deposition with the decomposition of germane on a "hot wire" – Hot Wire Chemical Vapor Deposition (HWCVD), offers significant advantages among these methods. In contrast to traditional CVD method, HWCVD achieves

precursor (GeH4) thermal decomposition on a hot wire located near the substrate, rather than directly on the substrate itself. Consequently, film deposition occurs rapidly and at low temperatures. Therefore, HWCVD method appears promising for depositing GeSn films on amorphous substrates even at equally low temperatures.

Limited information is currently available regarding dopant behavior and the resulting properties of polycrystalline GeSn films. In situ p-type doping of polycrystalline GeSn films is an under-explored area of research. The higher solubility of gallium (Ga) in the Ge matrix, relative to boron and aluminum, makes it a promising p-type dopant [7]. The aim of the work is to study in situ gallium (Ga) doping of single- and polycrystalline GeSn films during their growth using HWCVD method. We have previously demonstrated [8] that this method effectively produces high-quality epitaxial Ge layers on Si(001) at low temperatures (~ 350 °C).

Experiment procedure

Single- and polycrystalline Ge and GeSn films were deposited using HWCVD method in a custom-built setup at N. I. Lobachevsky State University of Nizhny Novgorod. The installation scheme is shown in Figure 1.

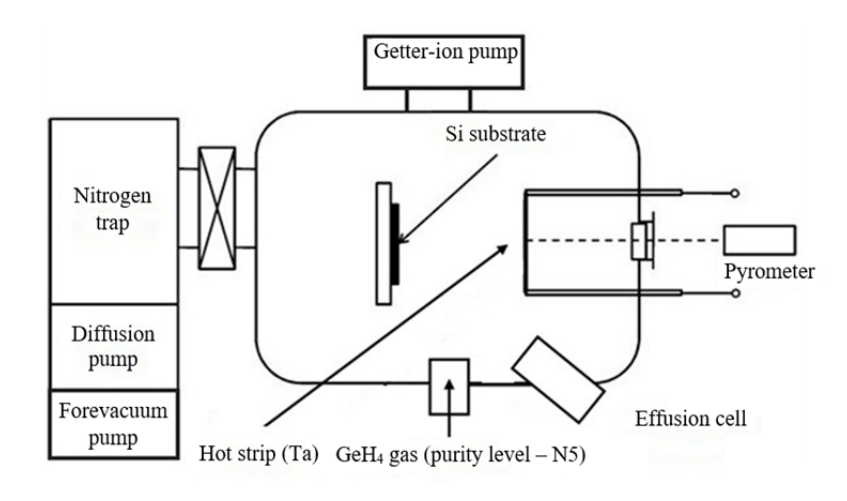


Fig. 1. Schematic diagram of the setup used for growing polycrystalline GeSn films using the HWCVD method

Film growth was conducted under non-equilibrium conditions, i.e., at low temperatures ($T_s = 250-350$ °C) due to the thermodynamic instability of GeSn solid solutions.

The substrates were radiatively heated using a custom-built heating setup. The base pressure in the growth chamber $\sim 5 \times 10^{-9}$ Torr and was created by titanium getter-ion pumps (GIP). Diffusion pump and a forevacuum pump were used to rough pump the **GINs** and the growth chamber. The diffusion pump allows pumping out any gases (including germane) in atomic and molecular states. A nitrogen trap, positioned above the diffusion pump, protected the growth chamber from back diffusion of oil from the forevacuum and diffusion pumps. A flow of germanium atoms was generated by decomposing germane (GeH₄) of N5 purity on a tantalum strip heated to 1400 °C. This introduced germanium into process growth chamber, achieving a pressure of 4×10^{-4} Torr. The germane pressure in the growth chamber during the growth polycrystalline GeSn films was maintained using a gas puffing system. The Sn flow was evaporated from a standard effusion cell. In situ doping of polycrystalline GeSn films with Ga atoms using a Ge:Ga source in HWCVD process was conducted for the first time. We first investigated the dopant transfer mechanisms from the source to the epitaxial film.

Subcontact device islands require polycrystalline films with a dopant concentration (up to $10^{20} \, \mathrm{cm}^{-3}$). We evaporated impurities from a molten zone

formed on a Ge:Ga source by increasing the current flow until melting occurred on its surface. The diffusion coefficient of Ga atoms in the semiconductor melt is several orders of magnitude higher than in the solid state [9]. This significantly increases the impurity flux density, leading to a higher Ga concentration in the deposited GeSn films.

High-resolution X-ray diffraction method (Bruker D8 Discover) was used to investigate the structure of single-crystalline and polycrystalline GeSn films grown on SiO2/Si(001) substrates. The parameters of Ge and GeSn films were studied by the Van der Pauw method at room temperature with Nanometrics H5500PC setup. The distribution of charge carrier concentration across the thickness of singlecrystalline films was determined with the C-V profiling method.

Results of experiment and discussion

We investigated the Ga atoms transfer from a Ge source: Epitaxial Ge films were doped with Ga (Ge grade GDG 0.003, Ga concentration: $\sim 1 \times 10^{19}$ cm⁻³) at substrate temperatures ranging from 300 to 500 °C. The Ge films grew at a rate of ~ 12 nm/min. The grown films thickness was $1 \div 2$ μ m. The relationship between hole concentration in the Ge:Ga film and the inverse growth temperature is shown in Figure 2. It exhibits an exponential relationship. The activation energy of doping calculated from the slope of the graph was 20.3 kcal/mol.

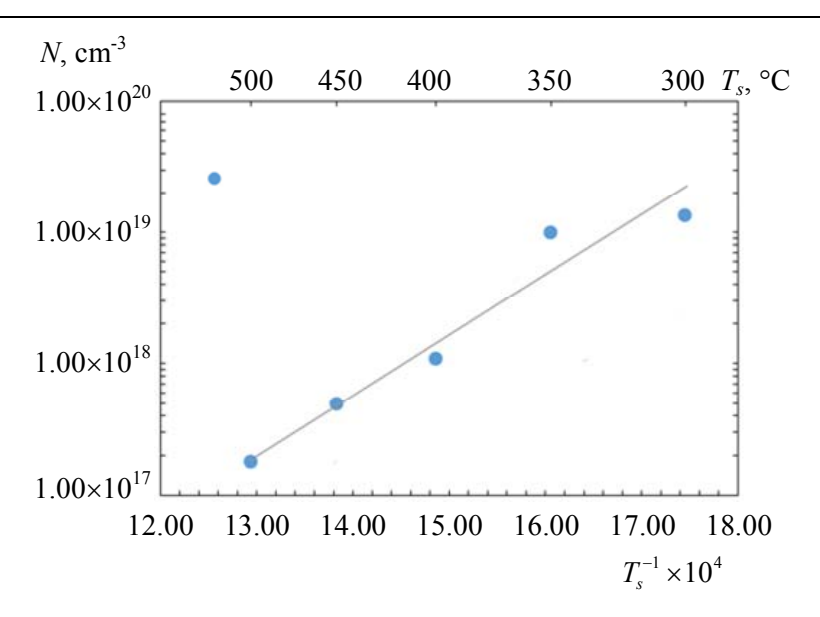


Fig. 2. Hole concentration dependence in Ge:Ga epitaxial layers on substrate temperature

Our study of Ga impurity transfer from a Ge:Ga sublimation source to a Ge film during Ge/Si(001) growth using HWCVD method revealed that hole concentration can be controlled by selecting an appropriate source and varying the growth temperature. This allows to obtain films with hole concentrations ranging from 1×10¹⁷ cm⁻³ to 1×10^{19} cm⁻³. Dopant concentration in the films was also controlled by varying the Ga/Ge atomic flux ratio, while maintaining a constant growth rate of v = 12 nm/min and temperature $T_{\rm s} = 350 \, {\rm ^{\circ}C}$. substrate The simplicity and reliability of this doping method for obtaining medium to high dopant concentrations in epitaxial films shall be emphasized. Growing highly doped films requires a maximum reduction in growth temperature. Due to the presence atomic hydrogen as a surfactant, HWCVD method enables the growth of structurally perfect Ge:Ga layers on Si(001) at low temperatures (300 °C). Table 1 structural parameters (according to the XRD method) Ge:Ga/Si(001) of films. For comparison, undoped Ge films were additionally grown in this set of experiments. As can be seen from the table, gallium doping enhances the structural perfection of Ge films, with a decreasing FWHM parameter.

Figure 3 shows the hole concentration distribution profile in the Ge:Ga/Si(001) epitaxial film grown at ~ 325 °C.

Table 1
Growth conditions and structural parameters of Ge/Si (001) and Ge films: Ga/Si (001)

No.	1	2	3	4	5
Film type	Ge	Ge:Ga	Ge:Ga	Ge:Ga	Ge:Ga
Ts, °C	300	300	350	450	500
Thickness, μm	1.5	1.6	2.0	0.8	1.4
FWHM, ang. min	6.9	3.87	3.75	5.7	2.898

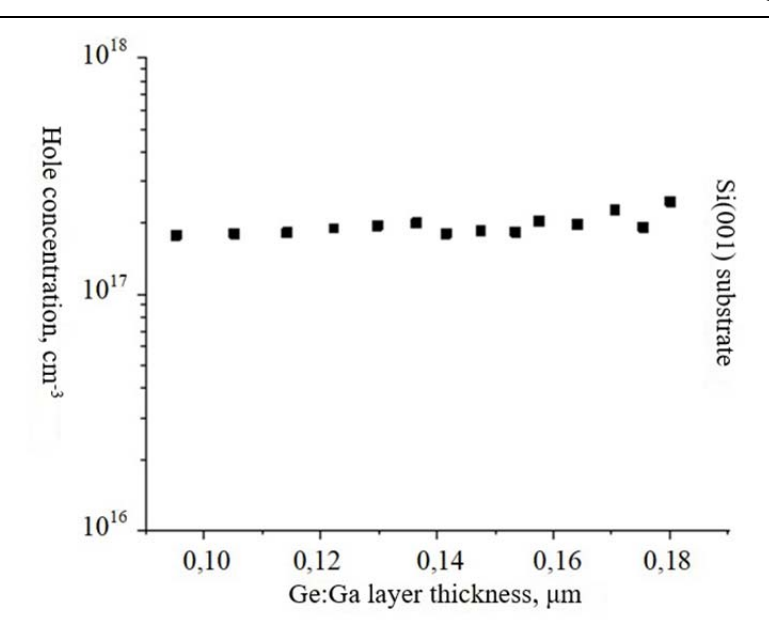


Fig. 3. Distribution of hole concentration across the Ge:Ga/Si(001) epitaxial layer grown thickness at $T_s = 325 \, \text{°C}$

The hole concentration in the epitaxial film was determined from diode capacitance dependence measurements of the $n^+-p^$ junction between the substrate and the film. Starting from the substrate the hole concentration is uniformly distributed at $\sim 2 \times 10^{17}$ cm⁻³ throughout nearly the entire measured film thickness. This value was also obtained using the Van der Pauw method when growing a Ge:Ga film on a highsubstrate. This uniform resistivity Ga concentration profile indicates segregation of Ga during film growth. This dopant behavior may be attributed to atomic hydrogen, a surfactant formed during GeH₄ decomposition on the "hot wire", which promotes layer-by-layer growth of Ge:Ga films.

Table 2 presents the growth parameters data (T_a – wire temperature, $T_{\rm Sn}$ – tin effusion cell temperature), composition (x) Ge_{1-x}Sn_x, structural perfection (FWHM), and electrical properties (charge carrier concentration and mobility, specific resistance) of both epitaxial and polycrystalline films.

Epitaxial GeSn films exhibit decreasing structural perfection with increasing tin content but improved structural perfection with in situ Ga doping. Evaporating Ga from a molten zone on a Ge:Ga source enabled us to achieve a maximum hole concentration of 55,4×10¹⁹ cm⁻³ in polycrystalline GeSn films grown on SiO₂/Si(100) substrates.

Table 2

Growth conditions, structural and electrical parameters of epitaxial and polycrystalline Ge_{1-x}Sn_x films

		T _{Sn} , °C	XRD data		Electrical parameters		
Sample No.	T _{Ta} , °C		<i>x</i> , %	FWHM,°	<i>N</i> , cm ⁻³	μ , cm ² /V·s	ρ, Ohm·cm
GeSn epitaxial films							
1	1450	1040	3.4	0.39	2.6×10 ¹⁷	124	0.19
2	1400	1040	3.7	0.43	5.2×10 ¹⁷	133	0.09

End of Table 2

Sample No.	T _{Ta} , °C	T _{Sn} , °C	XRD data		Electrical parameters		
			<i>x</i> , %	FWHM,°	N, cm ⁻³	μ , cm ² /V·s	ρ, Ohm·cm
GeSn:Ga epitaxial films							
3	1400	1040	1.7	0.2	4.4×10^{17}	299	0.05
4	1450	1040	2.2	0.24	1.3×10 ¹⁷	247	0.13
GeSn polycrystalline film							
5	1400	1020	-	1	5.9×10^{18}	34	0.03
6	1400	1030	_	-	3.9×10^{18}	37	0.043
GeSn:Ga polycrystalline films							
7	1400	1030	_	_	5.4×10^{19}	33	0.014
8	1450	1030	_	_	7.0×10^{18}	51	0.017

Conclusion

This study examined the factors governing in situ doping during the HWCVD growth of single- and polycrystalline Ge and GeSn films using a sublimating Ge:Ga source. The activation energy for Ga atoms (holes) doping in single-crystal Ge films was determined to be 20.3 kcal/mol from the dependence of hole concentration on substrate temperature. The uniform Ga distribution throughout the Ge film suggests minimal Ga segregation during the process. To enhance the hole concentration in the subcontact p+ regions of optoelectronic devices based on polycrystalline GeSn films grown on $SiO_2/Si(100)$ substrates, implemented a doping method used for the first time. By forming a molten zone on a achieved Ge:Ga source. we concentration of 5.4×10¹⁹ cm⁻³ in the GeSn films, surpassing the levels attainable with a sublimating Ge:Ga source.

The work was carried out with the support of the Russian Science Foundation, project (No. 23-22-00156).

Conflict of Interests:

The authors declare that they have no conflict of interests.

REFERENCES

- 1. Takeuchi W., Appl. Phys. Lett. **107**, 22103 (2015).
- 2. Uchida N., Appl. Phys. Lett. **107**, 232105 (2015).
- 3. Matsumura R., ECS Solid State. Lett. **4**, 95 (2015).
- 4. Takahashi K., Appl. Phys. Lett. **112**, 062104 (2018).
- 5. Toko K., Appl. Phys. Lett. **106**, 82109 (2015).
 - 6. Li H., Opt. Mater. Express 3, 1385 (2013).
- 7. Shengurov V. G., Semiconductors **49** (10), 1411–1414 (2015).
- 8. Glazov V. M. and Zemskov V. S. Physicochemical foundations of doping semiconductors: Monograph, Moscow, Nauka, 1967.
- 9. Shengurov V. G., Surface. Physics, Chemistry, Mechanics, No. 10-11, 44–50 (1994).
- 10. Boltaks B. I., Diffusion in Semiconductors. Moscow, State Publishing House of Physics and Mathematics Literature, 1961.

About authors

Vladimir Gennadievich Shengurov, leading research scientist, Lobachevskii State University of Nizhnii Novgorod (603950, Nizhny Novgorod, 23, Gagarin Ave., bldg. 3). E-mail: shengurov@nifti.unn.ru Author ID 121826

Anastasia Mikhailovna Titova, junior research scientist, Lobachevskii State University of Nizhnii Novgorod (603950, Nizhny Novgorod, 23, Gagarin Ave., bldg. 3). E-mail: asya_titova95@mail.ru

Natalia Alekseevna Alyabina, leading engineer, Lobachevskii State University of Nizhnii Novgorod (603950, Nizhny Novgorod, 23, Gagarin Ave., bldg. 3). Author ID 38741

Sergey Alexandrovich Denisov, head of the laboratory, Lobachevskii State University of Nizhnii Novgorod (603950, Nizhny Novgorod, 23, Gagarin Ave., bldg. 3). E-mail: denisov@nifti.unn.ru SPIN code 2743-6356, Author ID 624171

Vadim Yuryevich Chalkov, engineer, Lobachevskii State University of Nizhnii Novgorod (603950, Nizhny Novgorod, 23, Gagarin Ave., bldg. 3). E-mail: chalkov@nifti.unn.ru Author ID 125938

Vladimir Nikolaevich Trushin, leading research scientist, Lobachevskii State University of Nizhnii Novgorod (603950, Nizhny Novgorod, 23, Gagarin Ave., bldg. 3). E-mail: trushin@phys.unn.ru SPIN code 9995-2987, Author ID 27460

Alexey Vladimirovich Kudrin, senior research scientist, Lobachevskii State University of Nizhnii Novgorod (603950, Nizhny Novgorod, 23, Gagarin Ave., bldg. 3). E-mail: kudrin@nifti.unn.ru SPIN code 4194-2289, Author ID 612878

Yuri Nikolaevich Buzynin, research scientist, Institute of Microstructure Physics of the Russian Academy of Sciences (603950, Russia, Nizhny Novgorod Region, Kstovsky District, Afonino Village, 7, Akademicheskaya Street). E-mail: byzynin@ipmras.ru Author ID 28166

PHYSICAL SCIENCE OF MATERIALS

UDC 53.083.94 PACS: 07.07.Df EDN: EDLGZZ

Electrophysical properties of (Pd-SiO₂)/InP structures in hydrogen medium

© E. A. Grebenshchikova^{1,*}, V. A. Shutaev¹, F. A. Dobrychev¹, N. N. Gubanova^{2,3} and Yu. P. Yakovlev¹

¹ Ioffe Institute, St. Petersburg, 194021 Russia *E-mail: lot160@mail.ru

Received 16.12.2024; revised 24.03.2025; accepted 11.08.2025 Scientific specialty code: 1.3.11

Electrophysical properties of $(Pd\text{-}SiO_2)/InP$ structures in vacuum and in 100% hydrogen medium have been studied. The specified structures contained palladium nanoparticles in composition of a silica film synthesized by the sol-gel method on an n-InP substrate. It was shown that in hydrogen medium a decrease in cut-off voltage takes place by an amount of 0.03 V comparing to that in vacuum. Herewith the potential barrier resistance at U = 10 mV is decreased by about one order of magnitude in the temperature range 90–300 K. It is established that in hydrogen medium the tunneling conduction mechanism temperature range of the structure is increased from 90 to 200 K comparing to that in vacuum (90–150 K).

Keywords: nanoparticles; palladium; hydrogen; InP; sol-gel; conduction mechanism.

DOI: 10.51368/1996-0948-2025-4-81-86

Introduction

Palladium's (Pd) hydrogen unique absorption capacity and high hydrogen diffusion rate make the palladium-hydrogen system a subject of significant research interest [1–3]. The dissolution of significant amounts of hydrogen in Pd deforms the metal's crystal lattice, altering its electrical [2, 4], mechanical [5, 6], and optical [3, 7, 8] properties. These changes in properties enable the detection of hydrogen gas using various sensors. These sensors typically employ metal-semiconductor structures with

Schottky barrier [9] or metal-oxidesemiconductor (MOS) devices with catalytic metals like Pd or Pt [10, 11] as their sensing elements.

The Pd layer in these sensors is created using various techniques, such as thermal evaporation in a vacuum, vapor deposition, etc. [9, 12, 13]. We synthesized Pd nanoparticles dispersed within a thin silica film SiO₂ matrix using the sol-gel method [14]. Micro-level homogenization of the initial components ensures the production of materials with uniform composition [15].

² Petersburg Nuclear Physics Institute named by B. P. Konstantinov of NRC «Kurchatov Institute», Gatchina, 188300 Russia

³ Institute of Silicate Chemistry named by I. V. Grebenshchikov of PNPI of NRC «Kurchatov Institute», Saint-Petersburg, 199034 Russia

The sol-gel synthesis method is advantageous due to its simplicity, the readily available reagents and equipment, and its ability to form functional layers on various substrate geometries [16].

We have previously reported on the fabrication and electrical and photoelectric characterization of structures consisting of Pd nanoparticles in SiO₂ films, synthesized via sol-gel and deposited on *n*-InP substrates. Photoelectric hydrogen sensors based on these structures have shown promising results [17].

This article explores development of a hydrogen sensor using palladium Schottky diodes on A^{III}B^V semiconductors. This article investigates the electrophysical properties of (Pd-SiO2)/InP Schottky diodes with a thin silica film SiO₂ and Pd nanoparticles in vacuum and 100 % hydrogen atmosphere. This information is currently absent in the scientific literature.

Experiment

The manufacturing process used to create these structures is described in detail in [17]. The object of study is (Pd-SiO₂)/InP structures comprising Pd nanoparticles within the silica SiO₂ film fabricated by the sol-gel $n \sim 10^{16} \, \text{cm}^{-3}$. on *n*-InP (100), method Palladium chloride PdCl₂ served as precursor for Pd. A sol, prepared reproducible film formation, was spin-coated onto the InP substrate, forming a thin SiO2 film. The film was then annealed at ≤250 °C in air to enhance mechanical strength and silica matrix with uniformly a distributed Pd nanoparticles. The molecular ratio of components in the silica film was 20 mol Pd per 100 mol SiO₂. Hereinafter, these samples are designated as (Pd-SiO₂)/InP. X-ray reflectometry indicated that (Pd-SiO₂) films, containing Pd crystallites

approximately ~ 8 nm in size, had a thickness of ≤ 50 nm [17].

A cross-shaped Au contact was formed on the silica film to ensure uniform current distribution across the structure's surface. A silicon nitride (Si₃N₄) layer was used to define a 1 mm² active area and minimize leakage currents. A continuous Cr/AuGe/Au ohmic contact was formed on the substrate back side. 1.4×1.7 mm chips were mounted on standard TO-18 chip holders. A schematic diagram of the studied structures is shown in Fig. 1.

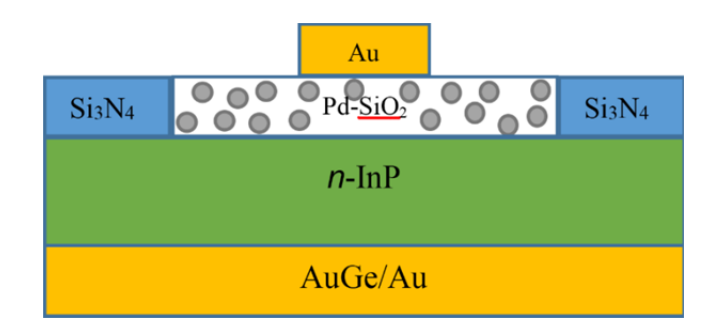


Fig. 1. Schematic diagram of the studied structure (Pd-SiO₂)/InP

The current-voltage characteristics (I-U) of the structures were measured from 80 to 300 K in 10 K increments, initially in a cryostat evacuated to 10^{-3} Torr, and subsequently in a cryostat filled with 100 % hydrogen. Measurements were conducted using a KEITHLEY-2600A source measurement unit (Keithley Instruments, Inc.), with data recorded on a computer (a positive potential was applied to the film containing Pd nanoparticles).

Results and their analysis

Let us consider the current-voltage characteristics (I-U) of $(Pd-SiO_2)/InP$ structures in the temperature range (80-300) K (Fig. 2).

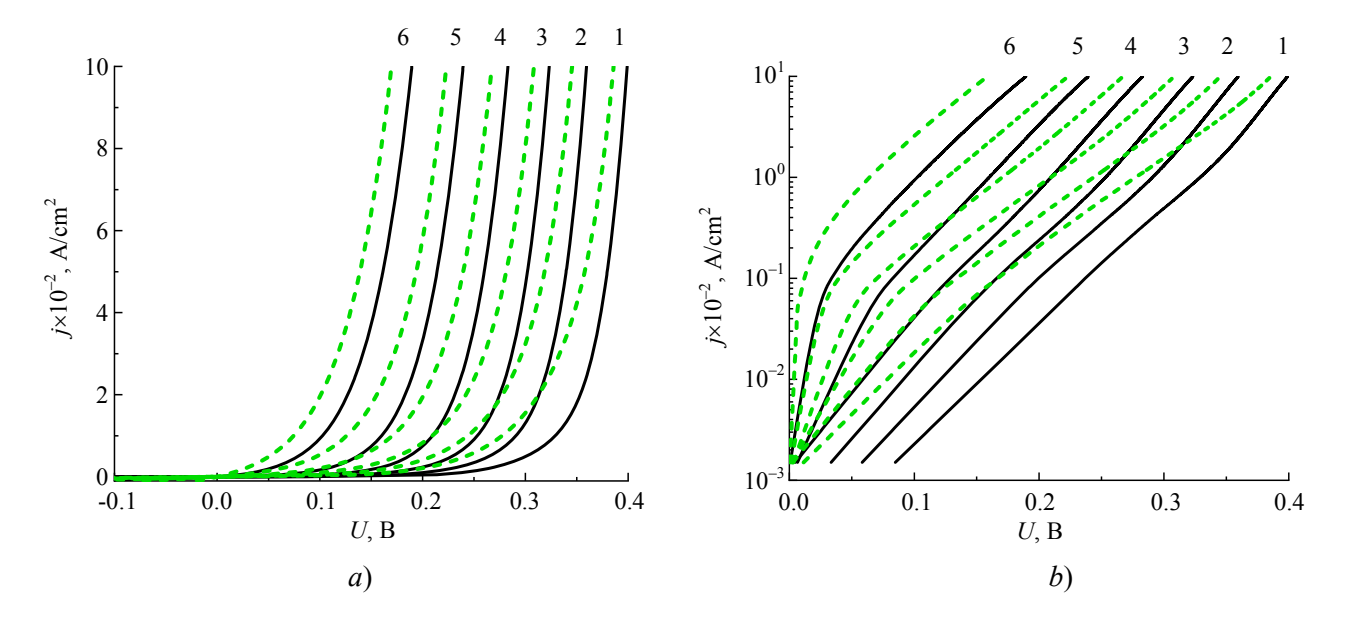


Fig. 2. Current-voltage characteristics of the $(Pd\text{-}SiO_2)/InP$ structure measured in vacuum (solid lines) and in 100 % hydrogen (dashed lines). Temperature K: 1 - 80, 2 - 130, 3 - 170, 4 - 210, 5 - 250, 6 - 300

It can be seen from the figure that the volt-ampere characteristics have a diode character. The forward current-voltage characteristic is well approximated by a function of the form:

$$j = j_0 \left[\exp(eU/\epsilon) - 1 \right], \tag{1}$$

where $\varepsilon = \beta kT$ describes different conductivity mechanisms in structures featuring a potential barrier, and j_0 is the voltage-saturation current.

The *I-U* characteristics undergo substantial changes when measured in a hydrogen atmosphere (100 % vol.) relative to *I-U* characteristics taken in vacuum (Figs. *2a* and *2b*). Throughout the studied temperature range (80–300 K), the forward *I-U* characteristics consistently shift left towards lower voltages, similar to the observed in Pd/InP structures with a continuous Pd layer.

The graph in Fig. 3 depicts how the cutoff voltage $U_{\rm cut-off}$ of the studied structure varies with temperature in vacuum and 100 % hydrogen atmosphere.

This parameter is obtained by extrapolating the volt-ampere forward characteristics to zero current at high forward bias. The cutoff voltage decreases almost

linearly with increasing temperature from 80 K to 300 K, both in vacuum and in hydrogen atmosphere. Within the temperature range of 80–300 K, the cutoff voltage studied in hydrogen environment is approximately ~0.03 V lower than that observed in vacuum.

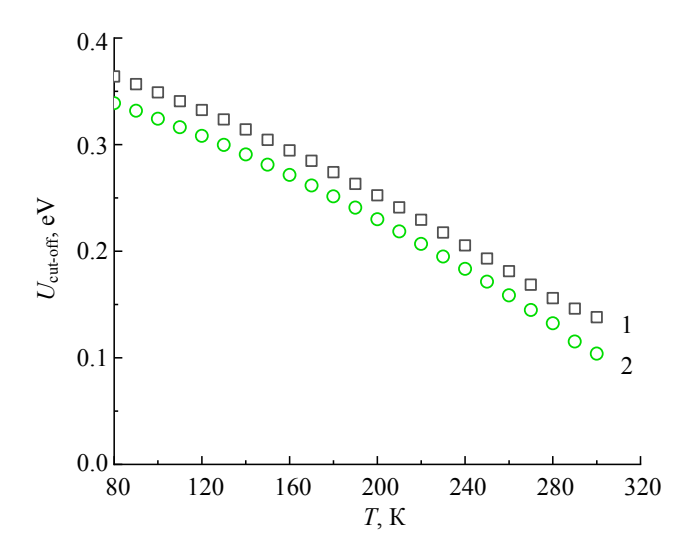


Fig. 3. Temperature dependence of the cutoff voltage of the (Pd-SiO₂)/InP structure; 1 – in vacuum, 2 – in a hydrogen environment

The resistance R_{sol} of the Pd-SiO₂ film, measured at high forward biases in vacuum over the temperature range 80–300 K, exhibits ohmic behavior and increases from 30 to 44 Ω with rising temperature (Fig. 4).

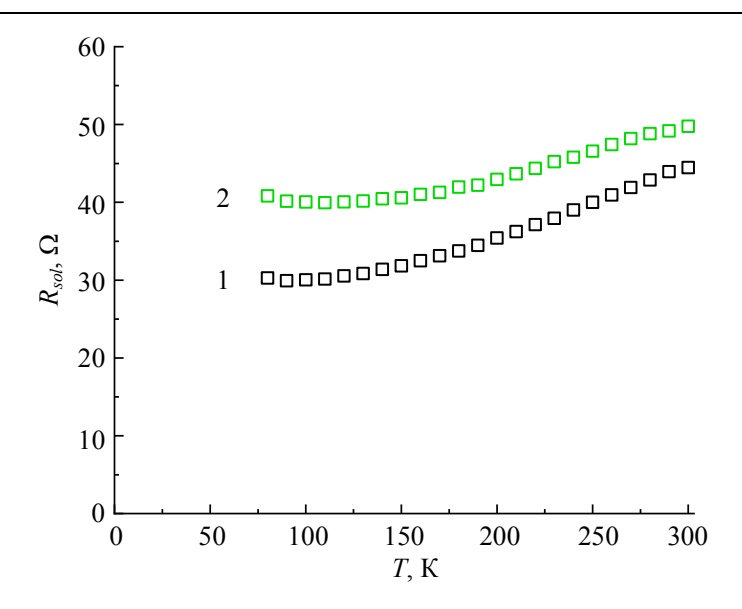


Fig. 4. Temperature dependence of the silica film resistance containing Pd nanoparticles: $1 - in \ a \ vacuum, \ 2 - in \ a \ hydrogen \ environment$

 R_{sol} increases from 40 to 50 Ω in the same temperature range in a hydrogen environment. The rise in R_{sol} may result from increased resistance of the silica matrix during interaction with hydrogen.

Fig. 5 shows the resistance temperature dependence of the structure R_0 potential barrier.

Its value is determined by the current-voltage characteristics slope at voltage values U = 10 mV. The R_0 resistance in the hydrogen environment decreases by approximately an order of magnitude compared to the vacuum

resistance. The resistance R_0 in vacuum and in hydrogen environment depends on 80 K-200 K temperature range. This is typical of the conduction tunneling mechanism. As the temperature increases above 200 K, the resistance R_0 in vacuum decreases exponentially, with an activation energy of $E_{a1} = 0.3$ eV. This parameter corresponds in magnitude to the height of the $U_{\text{cut-off}}$ barrier at 150 K. The indicated temperature may characterize the transition from the conduction tunneling mechanism to the thermal tunneling one.

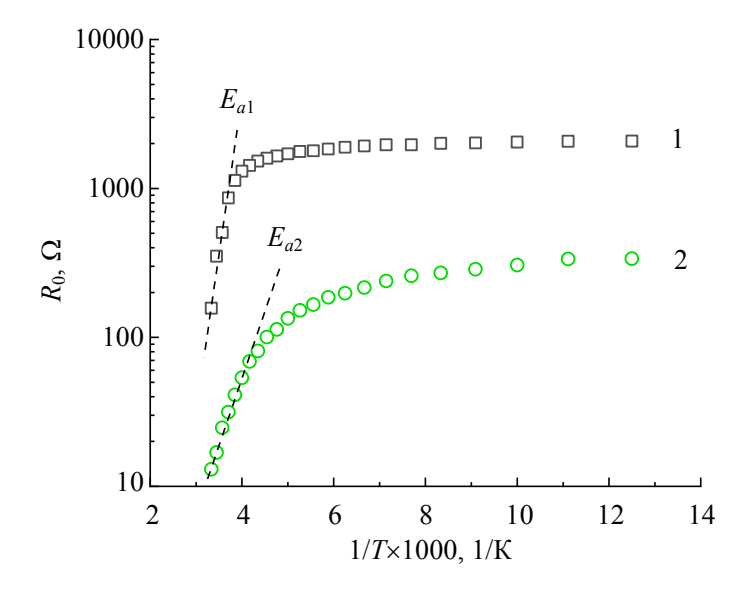


Fig. 5. The potential barrier resistance dependence of the $(Pd\text{-}SiO_2)/InP$ structure on temperature: 1 - in a vacuum, 2 - in the hydrogen environment

In the hydrogen environment, when the temperature rises above 200 K, the potential barrier resistance varies with an activation $E_{a2} = 0.23 \text{ eV}.$ energy of This corresponds to the barrier height at 200 K, as shown in Fig. 3. This change may also be used to define the temperature at which the mechanism transitions from conduction tunneling mechanism to thermal tunneling one. A sign that the tunneling component of the current is increasing is the expansion of the temperature range in which the tunneling mechanism predominates [18]. In the studied structures under vacuum conditions, temperature range is $\Delta T = (80-150) \text{ K},$ whereas in the hydrogen environment it is $\Delta T = (80-200)$ K. Therefore, in the hydrogen environment, the conductivity in the studied structures shifts towards the tunneling mechanism.

Conclusion

It was observed that when hydrogen is present (100% vol.), the I-U characteristic of the (Pd-SiO₂)/InP structure differs from its I-U characteristic in vacuum. It was observed that the cutoff voltage $U_{\rm cut-off}$ decreases by 0.03 V compared to vacuum $U_{\rm cut-off}$.

It was observed that the overall electrical resistance of the structure may be viewed as the sum of the series resistance from the silica matrix containing palladium nanoparticles and the resistance of the potential barrier in InP, which arises from the Pd nanoparticles in the silica film on the InP surface. The potential barrier resistance at U = 10 mV in a hydrogen environment decreases by an order of magnitude in the temperature range from 80 to 300 K.

It was determined that in the examined structures (Pd-SiO₂)/InP, tunneling and thermal tunneling conductivity mechanisms occur in the presence of hydrogen and in a vacuum at temperatures ranging from 80 to 300 K.

The R_{sol} resistance of the film made of a silica matrix with uniformly distributed

palladium nanoparticles (Pd-SiO₂) exhibits ohmic behavior. R_{sol} increases by 10–20 % in the hydrogen environment.

REFERENCES

- 1. Ndaya C. C., Javahiraly N. and Brioude A., Sensors **19** (4478), 1–34 (2019).
- 2. Ube T., Hasegawa S., Horie T. and Ishiguro T., J. Mater. Sci. **56**, 3336–3345 (2021).
- 3. Maier R. R. J., Jones B. J. S., Barton J. S., McCulloch S., Allsop T., Jones J. D. C. and Bennion I., J. Opt. A: Pure Appl. Opt., No. 9, 45 (2007).
- 4. Walter E. C., Favier F., Menke E. J. and Penner R. M., Fuel Chemistry Division Preprints 47 (2), 828–829 (2002).
- 5. Tovbin Yu. K. and Votyakov E. V., Physics of the Solid State **42**, 1192 (2000).
- 6. Kawasaki A., Itoh S., Shima K. and Yamazaki T., Mater. Sci. and Engin. A. No. 551, 231 (2012).
- 7. Shutaev V. A., Matveev V. A., Grebenshchikova E. A., Shchelokov V. G. and Yakovlev Yu. P., Opt. i. spectr. **129** (12), 1306 (2021).
- 8. Avila J. I., Matelon R. J., Trabol R., Favre M., Lederman D. et al., J. Appl. Phys. **107** (023504), 1–5 (2010).
- 9. Huey-Ing Chen, Yen-I Chou and Chin-Yi Chu, Sensors and Actuators B **85**, 10–18 (2002).
- 10. Šrobár F. and Procházková O., Phys. Status Solidi C **9** (7), 1687–1689 (2012). doi: 10.1002/pssc.201100578]
- 11. Wen-Chau Liu, His-Jen Pan, Huey-Ing Chen, Kun-Wei Lin, Shiou-Ying Cheng and Kuo-Hui Yu, IEEE Transactions on Electron Devices **48** (9), 1938–1944 (September 2001).
- 12. Shutaev V. A., Sidorov V. G., Grebenshchikova E. A., Vlasov L. K., Pivovarova A. A. and Yakovlev Yu. P., Semiconductors **53** (10), 1427 (2019).
- 13. Singh V., Dhall S., Kaushal A. and Mehta B. R., International journal of Hydrogen Energy, No. 43, 1025 (2018).
- 14. Gubanova N., Matveev V., Grebenshchikova E., Kirilenko D., Sazonova Y. and Shilova O., Physchem, No. 3, 259–269 (2023). https://doi.org/10.3390/physchem3020018].
- 15. Shabanova N. A. and Sarkisov P. D. Zol'-gel' tekhnologii. Nanodispersnyj kremnezem. Moscow, BINOM. Laboratoriya znanij, 2012 [in Russian].
- 16. Shilova O. A., Gubanova N. N., Matveev V. A., Bajramukov V. Yu. and Kobzev A. P., Glass Physics and Chemistry **42** (1), 78 (2016).

17. Grebenshchikova E. A., Shutaev V. A., Matveev V. A., Gubanova N. N., Shilova O. A. and Yakovlev Yu. P., Technical Physics Letters **48** (5), 54 (2022).

18. Grebenshchikova E. A., Evstropov V. V., Il'inskaya N. D., Melnikov Yu. S., Serebrennikova O. Yu., Sidorov V. G., Sherstnev V. V. and Yakovlev Yu. P., Semiconductors **49**, 364 (2015).

About authors

Elena Aleksandrovna Grebenshchikova, Candidate of Physical and Mathematical Sciences, senior research scientist, loffe Institute (194021, Russia, St. Petersburg, 26, Politekhnicheskaya st.). E-mail: lot160@mail.ru Author ID 116448

Vadim Arkadievich Shutaev, Candidate of Physical and Mathematical Sciences, research scientist, loffe Institute (194021, Russia, St. Petersburg, 26, Politekhnicheskaya st.). E-mail: vadimshutaev@mail.ru

Fedor Andreevich Dobrychev, student, laboratory assistant, loffe Institute (194021, Russia, St. Petersburg, 26, Politekhnicheskaya st.).

Nadezhda Nikolaevna Gubanova, Candidate of Chemical Sciences, Scientific Secretary, Head of the Laboratory, Petersburg Nuclear Physics Institute named by B. P. Konstantinov of NRC «Kurchatov Institute» (188300, Russia, Gatchina, Leningrad Region, 1, Orlova Roscha st.), Institute of Silicate Chemistry named by I. V. Grebenshchikov of PNPI of NRC «Kurchatov Institute» (199034, Russia, St. Petersburg, 2, Makarova Embankment). E-mail: gubanova_nn@pnpi.nrcki.ru SPIN code 2488-5747, Author ID 771184

Yuri Pavlovich Yakovlev, Doctor of Physics and Mathematics, Senior Research Assistant, Ioffe Institute (194021, Russia, St. Petersburg, 26, Politekhnicheskaya St.). E-mail: yakovlev.iropto@mail.ioffe.ru SPIN code 3394-1498, Author ID 20496.

ELECTRON, ION AND LASER BEAMS

UDC 535-3; 535-2; 539.3; 533.9 PACS: 79.20.Eb, 52.38.Mf

EDN: FKHVCE

Ablation of oxygen-free copper by bichromatic nanosecond laser pulses in air

© V. Yu. Zheleznov¹, V. V. Lychkouski², S. I. Mikolutskiy^{1,*}, V. E. Rogalin¹, Yu. V. Khomich¹ and A. N. Chumakov²

¹ Institute for Electrophysics and Electric Power RAS, St.-Petersburg, 191186 Russia

* E-mail: mikolserg@mail.ru

² B. I. Stepanov Institute of Physics NASB, Minsk, 220072 Belarus

Received 2.04.2025; revised 23.04.2025; accepted 11.08.2025

Scientific specialty code: 1.3.9

Features of plasma formation on the surface of oxygen-free copper under irradiation with double bichromatic (355 nm and 532 nm) nanosecond laser pulses with different time intervals and pulse sequences were revealed. Experiments were conducted with an increasing number of double bichromatic pulses and different pulse sequences at energy densities of about $200 \, \text{J/cm}^2$ each pulse. An increased crater depth was established with the laser pulse sequence of $532 \, \text{nm} + 355 \, \text{nm}$ compared to the reverse sequence of pulses with wavelengths of $355 \, \text{nm} + 532 \, \text{nm}$. The results of the work can be used to select the optimal mode of processing materials with double bichromatic pulses, as well as in further studying the features of laser plasma formation.

Keywords: nanosecond laser; bichromatic pulses; ablation; air medium; plasma spectra.

DOI: 10.51368/1996-0948-2025-4-87-93

Introduction

The study of materials laser ablation is of significant importance because of the ongoing advancements in laser technology and the growing range of its applications [1–3]. The laser ablation in air depends on the thermophysical and optical properties of the target materials, the wavelength and intensity of the laser radiation, as well as the laser pulse duration and their repetition frequency. It has been demonstrated that at high laser repetition rates (exceeding 5 kHz) and high laser radiation intensities, the ablation of

materials in air is primarily associated with the formation of erosive plasma, which significantly increases the pressure on the radiation surface [4]. In these ir radiation modes, the efficiency of material ablation increases significantly, thereby expanding the potential for laser processing [5–11].

Even when subjected to two nanosecond laser pulses with a time interval of units or tens of microseconds between them, an increase in the radiation material ablation and the resulting plasma heating was observed [12–15]. An increase in the heating of the near-surface plasma and an increase in ion

energy are also observed when subjected to two femtosecond laser pulses with time intervals ranging from units to thousands of picoseconds [16, 17]. Therefore, double-pulse laser action on materials is widely used in laser-induced spark emission spectroscopy [18].

Experiments have demonstrated that double-pulse bichromatic laser offers greater flexibility in managing the processes of laser modification and ablation of various materials, along with the heating of the near-surface plasma [19–23].

Copper and its alloys are basic materials in electrophysics and electrical engineering because of their excellent electrical and thermal conductivity [24]. However, the high thermal conductivity and reflectivity of copper may occasionally create challenges during its laser processing [25,To address this issue, neodymium Q-switched lasers are effectively used, producing laser radiation in the visible and ultraviolet (UV) ranges with acceptable efficiency [27–32]. advantages in laser plasma Additional formation and heating may be achieved through a two-pulse radiation mode using different wavelengths (bichromatic), which considers variations in the target's reflectivity radiation the plasma's absorption coefficient depending on the laser radiation wavelength [21, 32–34].

The purpose of this study is to investigate the plasma formation characteristics on the surface of oxygen-free copper when exposed to bichromatic pulses with varying time intervals between them, and to determine how the depth of ablation craters depends on the number of double pulses and their sequence.

Study object and experimental procedure

The study focused on polished samples of oxygen-free copper, measuring 40 mm in diameter and 8 mm in thickness, which

initially had a surface roughness of 25 nm and were subjected to radiation with bichromatic laser radiation in different modes. The experiment used a setup featuring two nanosecond Nd:YAG lasers (Lotis TII LH-2132 and Lotis TII LH-2137) with 532 nm and 355 nm wavelengths (λ), and 15 ns and 18 ns pulse durations, respectively. The synchronization system enabled the production of paired nanosecond pulses with a specific time interval and sequence, which is crucial due to the reflection coefficient for most metals significantly decreases as the wavelength shortens [34]. At $\lambda = 355$ nm, copper reflects approximately 10 %, and at $\lambda = 532 \text{ nm}$, it reflects 40 %, while $\lambda = 1064$ nm the reflection is 97 %.

The experiment investigated the formation of erosive plasma in air using different combinations of pulse sequences and interpulse time intervals. The ablation laser plume was recorded by a video camera based on the ICX415AL CCD matrix with an I-90U 4/75 lens (f=75 mm). The exposure of an individual frame was ~ 3 ms. A series of frames were recorded with synchronization from the second pulse of bichromatic laser radiation.

The peak power density (Wp) of the radiation was approximately 200 J/cm^2 with a $125 \, \mu \text{m}$ laser spot diameter created on the surface of the MB using a spectrum splitter and an achromatic objective. The number of double pulses and the delay time between them $\Delta \tau$ could be adjusted up to several microseconds. Following laser exposure, morphological alterations on the sample surface were examined using a NewView 7300 optical profilometer.

Results and discussion

The picture of near-surface plasma plume excited by bichromatic laser pulses with $\lambda = 355$ and 532 nm ($W \sim 200$ J/cm², $q_{355} = 12$ GW/cm², $q_{532} = 13.8$ GW/cm²) demonstrates distinctions for different pulse sequences (Fig. 1).

When the pulses with a wavelength of c $\lambda = 355$ nm acted first (Fig. 1*a*–*c*), the nearsurface plasma plume formed a vertically elongated shape. This most likely indicates the occurrence of plasma shielding and a shift of the plasma plume core away from the ir radiated surface. This elongated structure was formed under already laser radiation conditions $\Delta \tau = -1.4 \,\mu s$, initially appearing as a structure with a small protrusion (Fig. 1a), and rapidly reached its maximum size by $\Delta \tau = -4 \,\mu s$. A negative time delay indicates that the 355 nm pulses preceded the 532 nm pulses, while a positive time delay indicates that the 532 nm pulses preceded.

For case of $\lambda = 532$ nm pulses leading action (Fig. 1*g-i*), the plasma plume dynamics followed a similar pattern, but over a broader range. With a time delay of $\Delta \tau = +1.4 \,\mu s$, the near-surface plasma torch was hemispherical. At $\Delta \tau = +4 \,\mu s$, a protrusion appeared, similar to that observed at $\Delta \tau = -1.4 \,\mu s$, and by $\Delta \tau = +6 \,\mu s$, the elongated structure reached its maximum size.

At significantly lower bichromatic laser radiation (approximately GW/cm²), 1 previous work [33] reported that the nearsurface plasma was more heated when the 355 nm pulses led, with maximum heating observed at a time delay of $\Delta \tau = -1.4 \,\mu s$. This discrepancy may stem from differences in the absorption coefficients and mechanisms of the $\lambda = 355$ nm and 532 nm laser radiation by the near-surface plasma [35] and ablation products, as well as differences in the laser radiation energy parameters between this study and that reported in [33]. Thus, radiation $\lambda = 355$ nm penetrates deeper into the formed plasma and undergoes greater absorption near the irradiated surface, unlike 532 nm laser radiation, that also absorbed near the outer reach of plasma plume.

At high intensities, 355 nm laser radiation penetrates the target surface, significantly heating the resulting plasma along its entire path. This effect is amplified with bichromatic radiation because the first pulse (532 nm) affects the ablation products, which expand thermally during the inter-pulse interval, thereby influencing the subsequent pulse's interaction. However, further research into laser ablation dynamics is required to validate these assumptions.

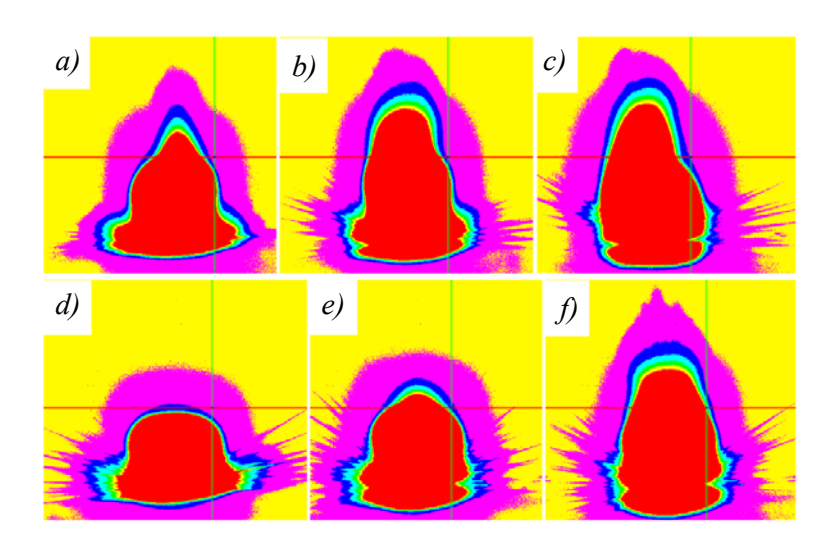


Fig. 1. Images show near-surface plasma generated by bichromatic laser pulses (355 nm at 12 GW/cm², 532 nm at 13.8 GW/cm²) with inter-pulse delays of: a) $-1.4 \mu s$; b) $-4 \mu s$; c) $-6 \mu s$; d) $+1.4 \mu s$; e) $+4 \mu s$; f) $+6 \mu s$.

Figure 2 shows crater profiles on a copper surface after single bichromatic pulse pair: one where the 355 nm pulse precedes 532 nm pulse $(\lambda = 355 + 532 \text{ nm})$ the $\Delta \tau = -1.4 \,\mu\text{s}$), and another one with 532 nm pulse leading action ($\lambda = 532 + 355$ nm, $\Delta \tau = +1.4 \,\mu s$). Despite the fact that the absorption coefficient of copper in the UV range is significantly higher than in the visible range, a significantly deeper crater (7 µm) is produced when the $\lambda = 532 \text{ nm}$ pulse precedes the 355 nm pulse in a combined exposure. The crater depth is \sim 4 μm with the reverse order of laser pulses. Single pulses at $\lambda = 355$ nm and $\lambda = 532$ nm produced crater depths of 4.4 μm and 2.3 μm , respectively.

Profilometry data clearly demonstrates this effect by showing crater depth variation with the number of double pulses, given a an interpulse time interval ($\Delta \tau = \pm 1.4~\mu s$) which also determines pulse sequence (Fig. 3). Significantly deeper craters result from a positive time delay, a factor to consider when optimizing material processing with double bichromatic pulses.

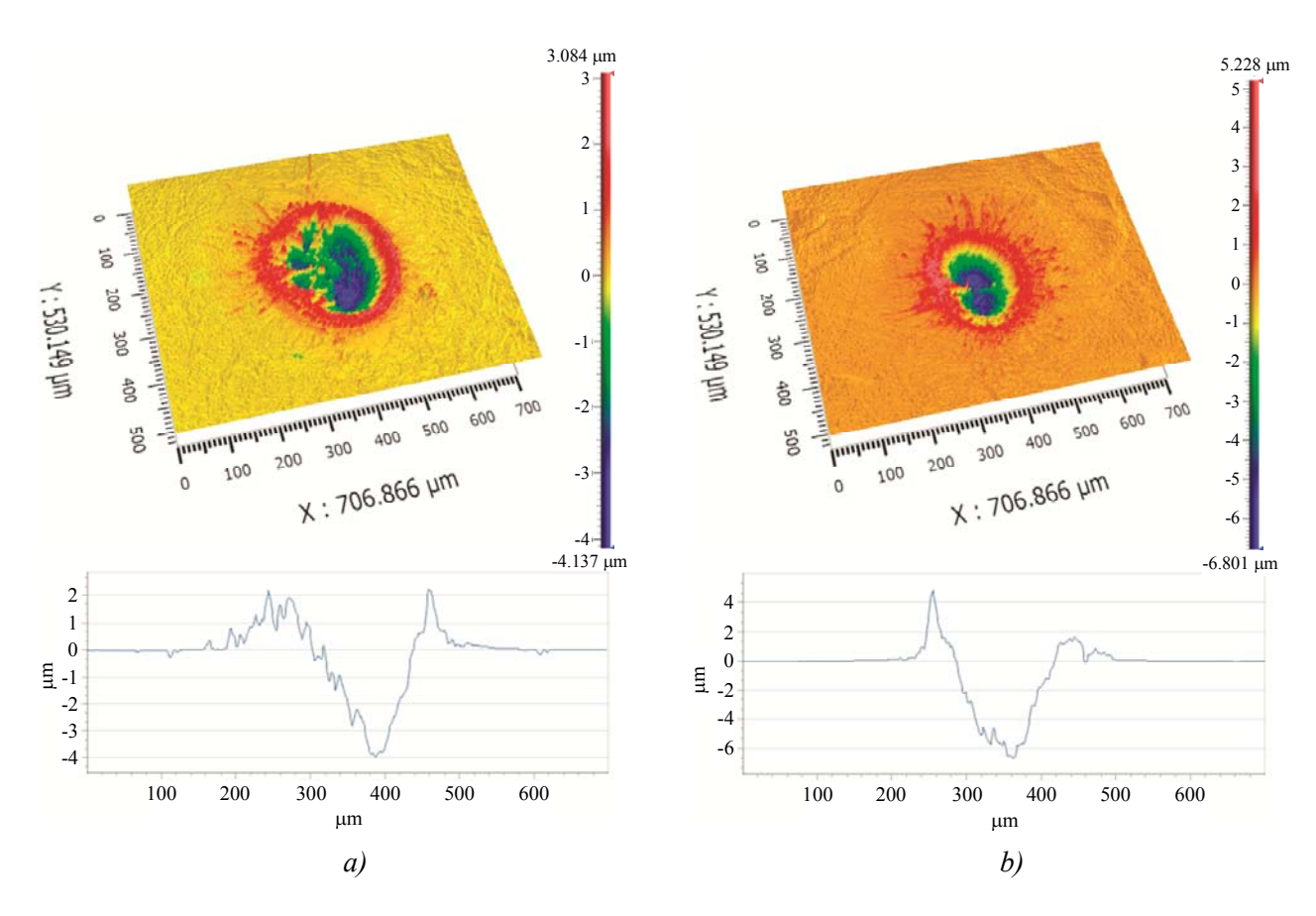


Fig. 2. Profilometry data (profilogram and central section) of oxygen-free copper, treated in air $W \sim 200 \text{ J/cm}^2$ bichromatic pulses: a) $\lambda = 355 + 532 \text{ nm}$; b) $\lambda = 532 + 355 \text{ nm}$

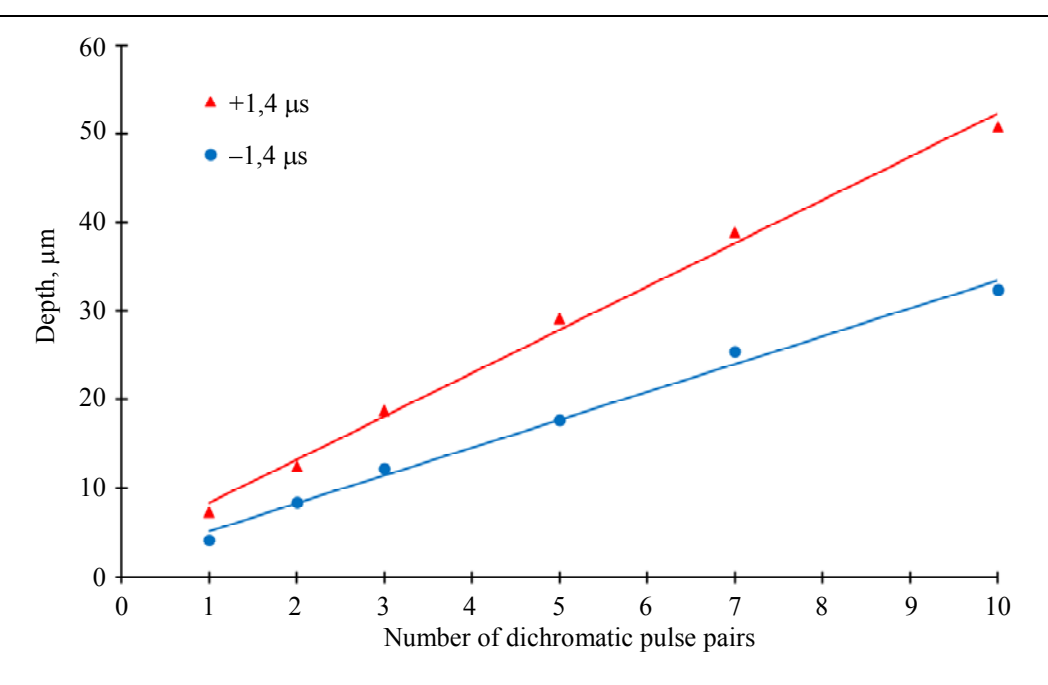


Fig. 3. Dependence graphs of the crater depth obtained after laser exposure on the laser pulses at different sequences of wavelengths and the delay time between them $(W \sim 200 \ J/cm^2)$. $\Delta \tau = -1.4 \ \mu s$ corresponds to the $\lambda = 355 + 532 \ nm$; $\Delta \tau = +1.4 \ \mu s$ corresponds to the $\lambda = 532 + 355 \ nm$

Conclusion

This paper examines how irradiation by pairs of nanosecond laser pulses with wavelengths of 355 nm and 532 nm, affect the polished surface of oxygen-free copper. Increased energy density ablation (around 200 J/cm^2) experiments using a CCD camera revealed differences in near-surface plasma plume formation: for the $\lambda = 355 \text{ nm}$ pulse leading action, the plasma plume was vertically elongated; however, the $\lambda = 532 \text{ nm}$ pulse leading resulted in more extensive plume dynamic changes.

Experiments using multiple pairs of nanosecond bichromatic pulses, with varied pulse order, showed that 532 nm pulses leading action caused production significantly deeper craters on oxygen-free copper samples compared to 355 nm pulses leading. Revealing of such effect contributes for optimization of material processing using double bichromatic pulses and enables fundamental advancements in laser plasma formation.

The paper has been prepared as part of the state assignment of the Ministry of Education and Science of Russia (FFGR-2025-0001), as well as the Government Scientific Research Program of the Republic of Belarus "Convergence-2025" (assignment 2.2.02).

REFERENCES

- 1. Prokhorov A. M., Konov V. I., Ursu I. and Mihailescu I. Interaction of Laser Radiation with Metals. Moscow, Nauka, 1988 [in Russian].
- 2. Anisimov S. I. and Luk'yanchuk B. S., Phys.-Usp. **45** (3), 293–324 (2002).
- 3. Grigoryants A. G. and Misyurov A. I. Technological Processes of Laser Processing. Moscow, Bauman MSTU, 2006 [in Russian].
- 4. Minko L. Ya., Chumakov A. N. and Bosak N. A. Sov. J. Quantum Electron. **20** (11), 1389–1393 (1990).
- 5. Sattmann R., Sturm V. and Noll R., J. Phys. D: Appl. Phys. **28**, 2181–2187 (1995).
- 6. Gorny S. G., Grigoriev A. M., Patrov M. I., Solovyev V. D. and Turichin G. A., Quantum Electron. **32** (10), 929–932 (2002).

- 7. Klimentov S. M., Pivovarov P. A., Konov V. I., Breitling D. and Dausinger F., Quantum Electron. **34** (6), 537–540 (2004).
- 8. Pershin S. M., Quantum Electron. **39** (1), 63–67 (2009).
- 9. Minko L. Ya., Chumakov A. N. and Bakanovich G. I., J. Appl. Spectrosc. **61** (5–6), 805–811 (1994).
- 10. Petukh M. L., Rozantsev V. A., Shirokanov A. D. and Yankovsky A. A., J. Appl. Spectrosc. **67** (6), 1097–1101 (2000).
- 11. Noll R. Laser-Induced Breakdown Spectroscopy. Fundamentals and Applications. Berlin, Springer, 2012, pp. 83–95.
- 12. Chumakov N., Avramenko V. B. and Bosak N. A., J. Appl. Spectrosc. **79** (2), 261–268 (2012).
- 13. Cristoforetti G., Legnaioli S., Palleschi V., Salvetti A. and Tognoni E., Appl. Phys. B. **80**, 559–568 (2005).
- 14. Ershov-Pavlov E. A., Katsalap K. Yu., Stepanov K. L. and Stankevich Yu. A., Spectrochim. Acta Part B. **63**, 1024–1037 (2008).
- 15. Khalil A. A. I., Laser Physics. **20** (1), 238–244 (2010).
- 16. Piñon V. and Anglos D., Spectrochim. Acta Part B. **64**, 950–960 (2009).
- 17. Amoruso S., Bruzzese R., Wang X., O'Connel G. and Lunney J. G., J. Appl. Phys. **108**, 113302 (2010).
- 18. Kremers D. and Radziemski L. Laser-Induced Breakdown Spectroscopy. Moscow, Tekhnosfera, 2009 [in Russian].
- 19. Chumakov A. N., Bosak N. A. and Panina A. V., J. Appl. Spectrosc. **84** (4), 620–626 (2017).
- 20. Chumakov N., Bosak N. A. and Verenich P. I., High Temp. Mater. Process. **18** (4), 269–272 (2014).
- 21. Chumakov A. N., Lychkovsky V. V., Nikonchuk I. S. and Matsukovich A. S., J. Tech. Phys. **67** (1), 16–24 (2022).

- 22. Höhm S., Herzlieb M., Rosenfeld A., Krüger J. and Bonse J., Appl. Surf. Sci. **374**, 331–338 (2016).
- 23. Bulgakov A. V., Sládek J., Hrabovský J., Mirza I., Marine W. and Bulgakova N. M., Appl. Surf. Sci. **643**, 158626 (2024).
- 24. Nikolaev A. K. and Kostin S. A. Copper and Heat-Resistant Copper Alloys. Moscow, DPK Press, 2012 [in Russian].
- 25. Rogalin V. E., Materialovedenie **9**, 34–42 (2013) [in Russian].
- 26. Rogalin V. E. and Krymskii K. M., J. Commun. Technol. Electron. **68**, 1464–1473 (2023).
- 27. Zheleznov V. Yu., Malinsky T. V., Mikolutskiy S. I. and Khomich Yu. V., Usp. Prikl. Fiz. (Advances in Applied Physics) **10** (6), 584–592 (2022) [in Russian].
- 28. Tunna L., Kearns A., O'Neill W. and Sutcliffe C. J., Opt. Laser Technol. **33**, 135–143 (2001).
- 29. Khomich Yu. V. and Mikolutskiy S. I., Acta Astronaut. **194**, 442–449 (2022).
- 30. Zheleznov V. Yu., Malinskiy T. V., Mikolutskiy S. I., Rogalin V. E. and Filin S. A., Applied Physics, No. 1, 38–42 (2024) [in Russian].
- 31. Tokarev V. N., Vasil'Yeva N. V., Cheshev E. A., Bezotosnyi V. V., Khomich V. Yu. and Mikolutskiy S. I., Laser Physics **25** (5), 056003 (2015).
- 32. Chumakov A., Lychkouski V., Nikonchuk I., Aniskevich V. and Kuznechik O., High Temp. Mater. Process. **29** (1), 9–14 (2025).
- 33. Luchkousky V. and Chumakov A. Proc. XV Belarusian-Serbian Symp. "Physics and Diagnostics of Laboratory and Astrophysical Plasmas". Minsk, Belarus, 2024, pp. 59–62.
- 34. Sokolov A. V. Optical Properties of Metals. Moscow, Fizmatlit, 1961 [in Russian].
- 35. Breitling D., Schittenhelm H., Berger P., Dausinger F. and Hügel H., Appl. Phys. A. **69**, S505–S508 (1999).

About authors

Viacheslav Yuryevich Zheleznov, Researcher, Institute for Electrophysics and Electric Power RAS (191186, Russia, St. Petersburg, 18, Palace Embankment). E-mail: vyuzheleznov@ieeras.ru SPIN code 9321-9395, Author ID 1091137

Viachaslau Valerievich Lychkouski, Researcher, B. I. Stepanov Institute of Physics NASB (220072, Belarus, Minsk, 68-2, Nezavisimosti Ave.). E-mail: v.luchkouski@dragon.bas-net.by SPIN code 5483-3905, Author ID 1124904

Sergey Ivanovich Mikolutsky, Candidate of Physical and Mathematical Sciences, Lead researcher, Institute for Electrophysics and Electric Power RAS (191186, Russia, St. Petersburg, 18, Palace Embankment). E-mail: mikolserg@mail.ru SPIN code 1699-7962, Author ID 631498

Vladimir Efimovich Rogalin, Doctor of Physical and Mathematical Sciences, Head of the Laboratory, Institute for Electrophysics and Electric Power RAS (191186, Russia, St. Petersburg, 18, Palace Embankment). E-mail: v-rogalin@mail.ru SPIN code 1644-1244, Author ID 177801

Yuriy Vladislavovich Khomich, Candidate of Technical Sciences, Lead researcher, Institute for Electrophysics and Electric Power RAS (191186, Russia, St. Petersburg, 18, Palace Embankment). E-mail: YKhomich@yandex.ru SPIN code 5923-9035, Author ID 762787

Alexander Nikitich Chumakov, Doctor of Physical and Mathematical Sciences, Chief researcher, B. I. Stepanov Institute of Physics NASB (220072, Belarus, Minsk, 68-2, Nezavisimosti Ave.). E-mail: a.chumakov@dragon.bas-net.by SPIN code 3991-6413, Author ID 743165

ELECTRON, ION AND LASER BEAMS

UDC 543.429.22:621.039.83 PACS: 87.80.Lg; 87.64.ks; 87.53.-j

EDN: FWUSBC

Quantitative EPR analysis of gamma-irradiated wheat seeds

© I. M. Medzhidov*, V. A. Kharlamov, D. I. Titova, D. V. Basyrova, T. V. Chizh and A. N. Pavlov

NRC «Kurchatov Institute» – RIRAE, Obninsk, Kaluga Region, 249035 Russia *E-mail: immedzhidov@mail.ru

Received 24.12.2024; revised 17.04.2025; accepted 11.08.2025 Scientific specialty code: 1.4.2; 1.5.1; 1.3.12

The applicability of electron paramagnetic resonance (EPR) spectrometry for identifying radiation treatment of seeds was investigated using spring wheat as a model. The seeds were irradiated with a "GUR-120" gamma facility at doses ranging from 100 to 1000 Gy. After irradiation, the seeds were stored under controlled conditions and analysed using EPR spectrometry. The dependence of EPR signal intensity on the radiation dose and the decay kinetics over time were analysed. An increase in EPR signal intensity was observed with higher radiation doses, indicating an increase in the concentration of paramagnetic centres. The signal decay kinetics showed a significant decrease in intensity during the first 14 days after irradiation, followed by a slower decay over several months. A quantitative analysis confirmed the correlation between radiation dose and the concentration of paramagnetic centres. The results indicate that EPR spectrometry is a sensitive method for identifying radiation treatment of wheat seeds.

Keywords: EPR spectrometry; quantitative analysis; gamma radiation; signal intensity; wheat seeds; free radicals.

DOI: 10/51368/1996-0948-2025-4-94-100

Introduction

Food safety and product quality control have become paramount concerns in the agroindustrial sector in recent decades. Grain losses during storage reach 10–30 % in the Russian Federation. The main reasons for these losses are damage by insect pests and phytopathogens. Based on a large body of research [1–3], the effectiveness of using radiation processing for disinfestation of grain and grain products has been demonstrated. Initial attempts to use this technology were

made in 1912, but insufficiently powerful sources prevented practical application [4]. Modern systems provide the power necessary for radiation disinsection. The introduction of GOST ISO 14470-2014 has spurred renewed interest in this field.

Zakladny G. A. and colleagues (1970, 1973) demonstrated that optimal radiation doses for wheat and barley ranged from 150 to 1000 Gy effectively control insects without compromising grain quality [5]. In addition, low-energy electron radiation is also being explored as a method for controlling

agricultural crop diseases [6]. After irradiation, the grain does not exhibit any induced radioactivity and retains its physical and chemical quality characteristics. IAEA requirements dictate the use of only gamma radiation sources (60Co or 137Cs), X-ray bremsstrahlung radiation (below 5 MeV), and accelerated electrons (below 10 MeV) for radiation [7]. Such products shall be marked with the "Radura-logo", as per international standards. However, if the product was not labeled accordingly, radiation treatment may still be experimentally confirmed. Electron paramagnetic resonance (EPR) spectrometry is among the most sensitive techniques for detecting evidence of radiation exposure. EPR spectrometry is an effective analytical method for investigating free radicals in various materials, such as organic and inorganic compounds, metals, and biological systems. Irradiation of food products generates paramagnetic centers (free radicals) that may be detected using EPR spectrometry. This method is non-destructive and highly making sensitive. it well-suited monitoring food irradiation.

This method is regulated by national (GOST R 52529-2006, GOST 31652-2012, etc.) and European (EN 1787:2000, EN 13708:2001, etc.) regulatory documents.

The purpose of this study is to explore the potential of using EPR spectrometry to detect irradiation in agricultural crop seeds, with spring wheat seeds serving as the example.

With this object in view the following tasks were solved:

- 1. Establishing the dependence between EPR signal intensity and the irradiation dose of wheat seeds.
- 2. Study of the EPR signal decay kinetics in irradiated seeds.
- 3. Conducting a quantitative analysis of paramagnetic centers in irradiated samples.
- 4. Assessment of the capabilities and limitations of EPR spectrometry for detecting irradiation in wheat seeds.

The results of this study may contribute to the development of new strategies for food quality and safety monitoring, as well as improve existing dosimetry methods.

Materials and methods

Irradiation and sample preparation

The study focused on spring wheat seeds of the Iren variety, harvested in 2023. The seeds were exposed to gamma radiation at doses ranging from 100 to 1000 Gy, in 100 Gy increments, using the unique scientific facility GUR-120 (UNU GUR-120 (No. 2795259)) at the Russian Institute of Radiology and Agroecology of National Research Centre «Kurchatov Institute». Nonirradiated seeds served as the control group. After irradiation, the samples were stored in plastic bags at room temperature and atmospheric pressure, away from direct sunlight.

The seeds were crushed using a coffee grinder (Kitfort) and a mortar and pestle, then sieved through a 0.5 mm mesh sieve. A 30 mg sample of each preparation was loaded into a quartz sample tube (\varnothing : 4 mm), designed for spectrometry. The sample tubes were positioned within the resonator's magnetic field, and the signal was recorded. All studies were conducted in three replications.

performed **EPR** spectrometry was immediately after irradiation, and then at 7, 14, and 28 days, and at 3 and 6 months to assess signal decay kinetics. Statistical data processing, using Student's t-test, performed with Microsoft Excel software. The data reliability relative to control is p < 0.05.

EPR spectrometry

EPR spectra of the gamma-irradiated samples were acquired immediately post-irradiation using an ESR70-03 XD/2

spectrometer (Minsk, Belarus) operating at X-band microwave frequency of 9.4 GHz.

The EPR spectrometer parameters during the measurements were as follows:

- middle of the field 3350 Oe;
- field range 1000 Oe;
- modulation frequency 100 kHz;
- modulation 4 Oe:
- microwave power 50 mW;
- gain factor 50;
- spectrum acquisition time 600 sec.

G-factor calculation

The G-factor was determined using the following formula [8]:

$$hv = g\mu_{\scriptscriptstyle R}B,\tag{1}$$

where h is Planck's constant; v is the microwave frequency of the X-band; μ_B is the Bohr magneton; B is the set point of the magnetic field (E).

The g-factor is a crucial parameter in EPR spectrometry, used to determine the electron spin and characterize the paramagnetic center under investigation.

Quantitative analysis of EPR spectra

Quantitative EPR spectral analysis involves determining the concentration, distribution, and interactions of paramagnetic centers within a sample. EPR spectra quantitative analysis may be divided into several stages:

- 1. Normalized intensity of a standard sample was determined by double integration of its peak area. The paramagnetic centers number in the standard sample is given by the manufacturer (All-Russian Scientific Research Institute for Physical-Engineering and Radiotechnical Metrology) and is 10¹⁵. Quantification of paramagnetic centers was performed using a standard sample of magnesium oxide doped with Mn²⁺ (Reg. No. 67380-17).
- 2. Normalized intensity of a tested sample was determined by double integration

of its peak area.

3. The concentration of paramagnetic centers in the samples was determined using the following formula [8]:

$$C_{u} = \frac{I_{n(u)} \times C_{st}}{I_{n(st)}}, \tag{2}$$

where C_u is the paramagnetic centers concentration in the test sample; $I_{n(u)}$ is the normalized intensity of the test sample; $I_{n(st)}$ is the normalized intensity of the standard sample; C_{st} is the paramagnetic centers concentration in the standard sample.

Results and their discussion

Registration of EPR spectra

The study was conducted by recording the EPR spectra for all samples immediately after irradiation. Figure 1 shows the recorded spectra of some samples.

The increasing EPR signal intensity with higher radiation doses demonstrates the potential of EPR spectrometry for detecting irradiation. The control sample exhibited a small, naturally occurring peak attributed to free radicals formed during plant's growth and exposure to sunlight. The control sample exhibited an amplitude of 495 relative units. Irradiation at 200 Gy increased the amplitude by 92 % relative to the control, reaching 950 relative units. The signal amplitudes were 1220, 1260, and 1150 relative units for irradiation doses of 400, 800, and 1000 Gy, respectively. The sample irradiated 1000 Gy showed a lower peak intensity compared to samples receiving lower doses. We assume that this is due to an error during irradiation. It's important to note that doses below 1 kGy are generally difficult to analyze using EPR spectrometry. The g-factor, measured where the derivative curve crosses the zero line, was 2.0048 for all samples. The data obtained indicate the presence of carbon containing radicals.

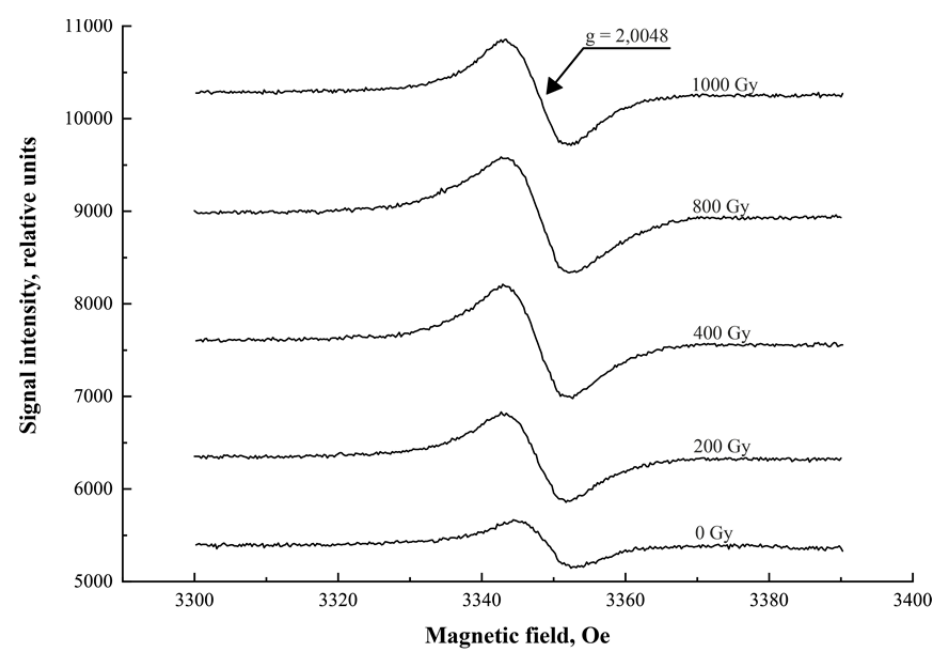


Fig. 1. EPR spectra of wheat seed samples recorded immediately after irradiation

EPR signal decay kinetics

EPR spectrometry was used to assess decay kinetics by measuring the samples at various time points after irradiation. The following time points were selected: 7, 14, 28 days, 3, 6 months after irradiation. Samples were stored in a quartz tubes protected from light for the duration of the study. Figure 2 shows the EPR signal decay kinetics in wheat seeds irradiated with a 1000 Gy dose.

The EPR signal shows attenuation over time. The observed attenuation is due to the

decay of free radicals formed by irradiation. The signal attenuation takes place within the first 14 days following radiation exposure process. This is caused by the fact that irradiation generates a large number of short-lived radicals, resulting in a significant reduction in EPR signal intensity during the first 14 days. A slight decrease in signal intensity is observed, as irradiation also produces more stable radicals with lifetimes of up to 1 year [9], and in some cases even longer [10].

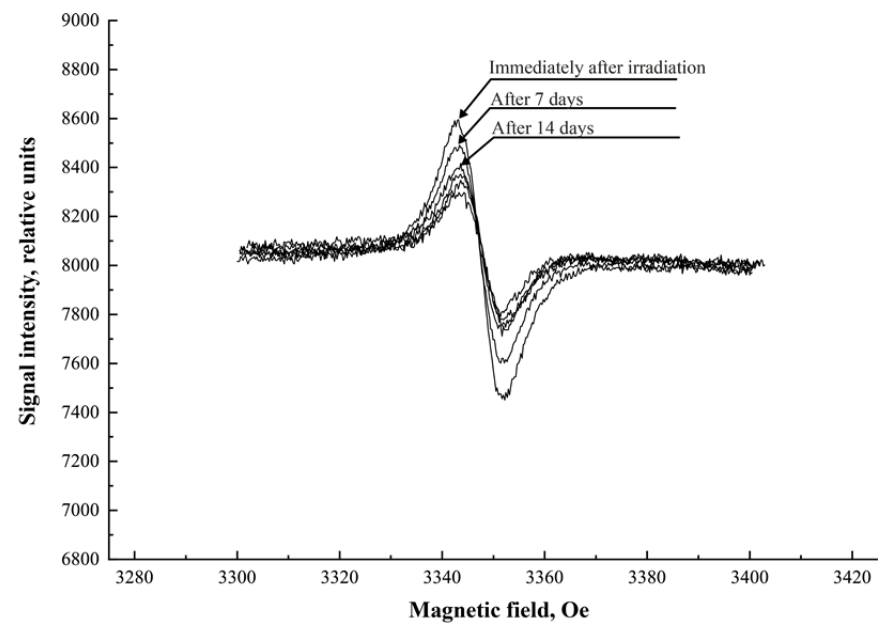


Fig. 2. EPR signal decay kinetics of a wheat seed sample irradiated with a 1000 Gy dose

Number determination of paramagnetic centers

To achieve a more accurate analysis, the spectra of all samples were double-integrated to determine the area under the peak values. The number of paramagnetic centers in each sample was calculated using formula 2. Spectra integration and plotting were performed using OriginPro 2018 software. The results are shown in the Fig. 3.

According to the graph, the decay of paramagnetic particles is observed over time. As previously noted, the most significant signal attenuation is observed within the first 14 days across the entire doses range. Further, a slight attenuation is observed. Storage

conditions play an important role in signal attenuation. In this study, the irradiated samples were stored at atmospheric pressure and room temperature inside a quartz tube. This could have affected the signal drop. A decrease in free radicals is also observed in the control sample, which is a natural occurrence since the control initially exhibited a small signal generated naturally during the growing season.

The data obtained in this study on the kinetics of EPR signal attenuation in irradiated wheat seeds, along with the quantitative analysis of paramagnetic centers, substantially enhance the understanding of previously studied effects [11, 12].

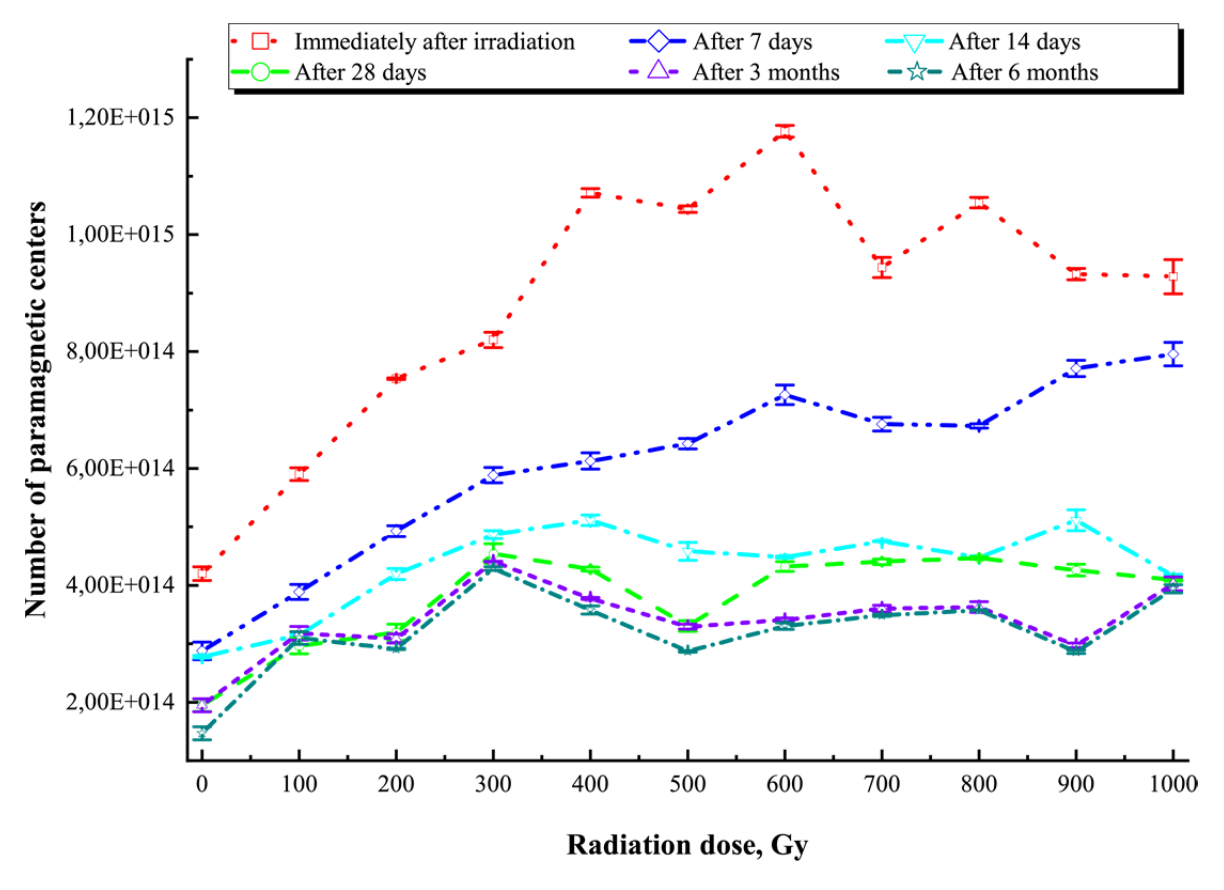


Fig. 3. Kinetics of free radical decay over time

Conclusion

This study explored the possibility of using EPR spectrometry to detect whether wheat seeds have undergone radiation treatment. The experiments confirmed that EPR spectrometry is an effective method for

detecting irradiation of wheat seeds within the dose range of 100 to 1000 Gy. The results demonstrated that the EPR signal intensity increases as the irradiation dose increases. However, this method is unsuitable for accurately determining the radiation dose in wheat samples within the studied range, as

the differences in signal are not sufficiently distinct. The g-factor, measured where the derivative curve crosses the zero line, was 2.0048 for all samples. The data obtained indicate the presence of carbon containing radicals.

A study of decay kinetics revealed that the EPR signal intensity weakens over time, with the most significant decrease occurring within the first 14 days after irradiation. This is due to the decay of short-lived radicals formed during the irradiation. Subsequent attenuation proceeds at a slower rate, attributed to the presence of more stable radicals.

The paramagnetic centers quantity was also determined, confirming the potential of EPR spectrometry for quantitative analysis of irradiated wheat samples.

Thus, EPR spectrometry has demonstrated its effectiveness as a method for detecting radiation treatment in wheat seeds and assessing the radiation dose. Further optimization of analytical methods is needed to improve the accuracy of dose determination within the 100–1000 Gy range.

REFERENCES

1. Kozmin G. V., Geras`kin S. A. and Sanzharova N. I. Radiation technologies in agriculture and food industry. Obninsk, VNIIRAE, (2015) [in Russian].

- 2. Zakladnoj G. A. Radiation disinfection of grain: Monography. Moscow, Centr podgotovki specialistov, (2020) [in Russian].
- 3. Loy N. N., Sanzharova N. I., Chizh T. V. and Shishko V. I. Trudy FGBNU VNIIRAE. Pod red. N. I. Sanzharovoj. Obninsk, pp. 107–123 (2023) [in Russian].
- 4. Aleksaxin R. M., Sanzharova N. I., Kozmin G. V., Pavlov A. N. and Geras'kin S. A., Bulletin of the Russian Academy of Sciences **14** (1), 78–85 (2014) [in Russian].
- 5. Mordkovich Ya. B. and Baranova L. I., Plant Health and Quarantine, No. 3, 60–64 (2023) [in Russian].
- 6. Loy N. N., Sanzharova N. I., Gulina S. N., Suslova O. V., Chizh T. V., Vorobyov M. S. and Doroshkevich S. Yu., J. Phys. Conf. Ser. **2064**, 012101 (2021).
- 7. Vazirov R. A., Sokovnin S. Yu. and Balezin M. E. Nuclear physics research and technologies in agriculture: collection of reports of the international scientific and practical conference. Obninsk, pp. 315–318 (2020) [in Russian].
- 8. Eaton G. R., Eaton S. S., Barr D. P. and Weber R. T. Quantitative EPR. New York, Springer (2010).
- 9. Medzhidov I., Vasileva N., Polyakova I. and Sanzharova N. IV International Conference on Geotechnology, Mining and Rational Use of Natural Resources (GEOTECH-2024), Navoi, Uzbekistan **525**. Les Ulis, 02025 (2024).
- 10. Karakirova Yordanka and Yordanov Nicola D., Radiation Physics and Chemistry **168**, 108569 (2020).
- 11. Wang Z. and You R., Environmental and Experimental Botany **43** (3), 219–225 (2000).
- 12. Hong M. J., Kim D. Y., Jo Y. D., Choi H.-I., Ahn J.-W., Kwon S.-J., Kim S. H., Seo Y. W. and Kim J.-B., Appl. Sci. **12**, 3208 (2022).

About authors

Ibragim Medzhidovich Medzhidov, Research Assistant, NRC «Kurchatov Institute» – RIRAE (249035, Russia, Kaluga region, Obninsk, 1, Kievskoye shosse, bldg. 1). E-mail: immedzhidov@mail.ru SPIN code 9420-5220, Author ID 1039588

Vladimir Aleksandrovich Kharlamov, Candidate of Biological Sciences, senior research scientist, NRC «Kurchatov Institute» – RIRAE (249035, Russia, Kaluga region, Obninsk, 1, Kievskoye shosse, bldg. 1). E-mail: kharlamof@gmail.com SPIN code 7948-0744, Author ID 695938

Daria Igorevna Titova, Candidate of Biological Sciences, senior research scientist, NRC «Kurchatov Institute» – RIRAE (249035, Russia, Kaluga Region, Obninsk, 1, Kievskoye Shosse, bldg. 1). E-mail: daria.petrukhina@outlook.com SPIN code 4199-3096, Author ID 961493

Daria Vladimirovna Basyrova, Research Assistant, NRC «Kurchatov Institute» — RIRAE (249035, Russia, Kaluga region, Obninsk, 1, Kievskoye shosse, bldg. 1). E-mail: reckunowa.dasha@yandex.ru SPIN code 8941-3630, Author ID 1127207

Taras Vasilyevich Chizh, Candidate of Biological Sciences, junior research scientist, NRC «Kurchatov Institute» – RIRAE (249035, Russia, Kaluga region, Obninsk, 1, Kievskoye shosse, building 1). E-mail: taras.chizh@rambler.ru SPIN code 8221-0068, Author ID 635150

Alexander Nikolaevich Pavlov, Candidate of Biological Sciences, senior research scientist, NRC «Kurchatov Institute» – RIRAE (249035, Russia, Kaluga Region, Obninsk, 1, Kievskoye Shosse, bldg. 1). E-mail: 49434@mail.ru SPIN code 1932-2409, Author ID 835431

PHYSICAL EQUIPMENT AND ITS ELEMENTS

UDC 621.56, 536.2, 621.383.4 PACS: 07.20.Mc, 44.10.+I, 85.60.Gz

EDN: KSMVRI

Development of a model for calculating heat flows for use in the design of a Dewar assembly for infrared modules

© D. D. Babenko*, M. V. Bannikov and G. I. Nekrasov

RD&P Center ORION, JSC, Moscow, 111538 Russia *E-mail: rainbowdm1802@gmail.com Received 5.06.2025; revised 24.06.2025; accepted 11.08.2025

Scientific specialty code: 2.4.8; 2.2.6

The article discussed a generalized and improved model for calculating heat inleaks when developing a Dewar assembly for infrared modules. In this work calculations and experimental data were compared. The main sources of heat inleaks were identified, and points that can be neglected were noted. Points for further development of the calculated model were defined.

Keywords: gas cryogenic machine; cryocooler; Stirling's cycle; microcryogenic machine; cold tip temperature.

DOI: 10.51368/1996-0948-2025-4-101-106

1. Introduction

While designing cooled matrix infrared modules, the Dewar assembly plays a crucial role, as its design and used materials affect the heat load the cryocooler. on Consequently, the proper Dewar design the overall module's power consumption, and in some cases, even the choice of cryocooler itself, which also affects the module's dimensions. While designing a input parameters Dewar assembly, considered, such as the dimensions of module, Focal Plane Assembly (FPA) with the Read-Out Integrated Circuit (ROIC) and the metal-ceramic unit. Subsequent design work focuses on optimizing thermodynamic and mechanical parameters of the Dewar and the final device as a whole.

The main source of heat inleaks is thermal conductivity along the coldfinger.

This part can be reduced only through the geometry and material of the coldfinger. The geometry of the coldfinger (in most cases) includes its length and cross-sectional area. Choosing the right geometry is a complex problem, as it involves many factors that depend on each other. First of all, increasing the length of coldfinger helps to reduce heat flow along it, and also allows to larger regenerative heat exchanger (regenerator), which will make a positive effect on the performance of the cryocooler. But the length of the regenerator is limited, firstly, by the overall dimensions of the final device, and secondly, by the mechanical properties of the construction. Mechanical properties also impose restrictions on the diameter of the coldfinger, and as a result on the surface area through which heat transfer is performed. An alternative way to reduce heat transfer through geometry is to reduce the

wall thickness, but previously RICOR specialists [1] identified optimal thickness values for several coldfinger materials.

The second largest heat load is the heat inleak through radiative heat transfer. In the vacuum gap between the outer wall of the Dewar and the coldfinger, heat is transfered by radiation from the more heated surface of the Dewar to the coldfinger, which has a different temperature in its area cryostating temperature (depending on the cryocooler, temperature can be in the range of 4.2–150 K) to the temperature of the Dewar close to the ambient temperature (up to 75 °C). make the Temperatures significant contribution to the value of heat flow, which is obvious from the Stefan-Boltzmann law, but the only way to reduce heat input by temperature is to increase the cryostating temperature or reduce operating temperature of the final product. Often, these parameters are set for the device before designing the Dewar and couldn't be adjusted. Therefore, at the design stage, it is possible to reduce heat flows through radiation only by changing the geometry, by changing the interacting areas and the material of the Dewar and coldfinger.

Heat inleaks from the ROIC and FPA is also taken into account. If the cooled device has already been manufactured and can be mounted in Dewar, then it is possible to obtain a heat flow experimentally measuring the difference in heat flows with the device turned off and on.

A lesser contribution is made by heat inleaks from the external environment through the outputs to the contact pads and heat influxes due to residual gases. Calculation of heat influxes due to residual gases showed that their values are several orders of magnitude lower (about $\sim 300~\mu W$) than the contribution from other sources of heat inleaks described above.

2. Coldfinger heat conductivity

As follows from paragraph 1, heat inleaks due to thermal conductivity make the

greatest contribution to the total amount of heat inleaks of the Dewar, which means that it is vital to start modifying the calculation model from them. Usually, heat flows due to thermal conductivity are calculated according to the dependence:

$$Q_{tc} = \lambda_{cf} \times (T_h - T_c) \times \frac{S_{cf}}{h_{cf}}, \qquad (1)$$

where λ_{cf} – thermal conductivity of the coldfinger material, T_h μ T_c – temperatures of the hot and cold ends of the coldfinger respectively, S_{cf} – cross–sectional area of the coldfinger, h_{cf} – length of the coldfinger. Commonly, values at normal climatic conditions (NCC) are taken for thermal conductivity, but in a reality, the temperature of the coldfinger along the length varies significantly, as does the value of thermal conductivity from temperature.

In the proposed model, integral value of the thermal conductivity function from the temperature of the material in the range from T_c to T_h is taken as thermal conductivity. The lack of thermal conductivity values at cryogenic temperatures for many materials adds difficulties to calculations. However, for some materials often used in cryogenic technologies, there is a library [2] of functions for thermal conductivity, heat capacity, Young's modulus and expansion coefficient. Also, for materials with known tabular values in the field of cryogenic temperatures, an approximation can be performed and the resulting function can be used as the initial one. For materials unexamined in the field of cryogenic temperatures, it is possible to approximate the available values in the first approximation, but it is worthwhile to carefully consider the possible abnormal behavior of the function, especially when approaching the temperatures of liquid helium.

Another value that needs to be adjusted is the temperature of the hot end of the coldfinger. It is usually assumed to be equal

to the ambient temperature. As a part of the work, an experiment was conducted to measure the housing temperature during running time. The cryocooler Cryo 1000, manufactured by RD&P Center Orion, was operation for 48 hours into environmental temperature of 22 °C, after which the temperature of the coldfinger at the junction with the cryocooler housing was measured. The temperature was measured with a pyrometer and a thermocouple, and as a result, a value of 32.5 °C was obtained, so a correction was made and the temperature of the hot end was considered to be equal to

$$T_{\rm e} = E_{\rm o.c.} + \tau; \ \tau = 10.5 \, ^{\circ}{\rm C}$$
 (2)

where $T_{\text{o.c.}}$ – ambient temperature, τ correction factor value. Cryocooler can operate in a wide temperature range from -50 °C to +65 °C, therefore, based on the results obtained, the housing was simulated at boundary operating temperatures. Simulation with the same operating mode showed that the correction factor differs by 0.1 °C at the boundary points, which is insignificant. In fact, when the operating mode is fixed, the heat flow from the compression volume is fixed, the material and geometry of the housing do not change and the temperature change depends only on the convective heat exchange of the walls with the external environment. In the future, it is planned to supplement the model with the dependence of the thermal load created in the compression depending ambient volume on the temperature, since as it increases, the rotation frequency of the electric motor increases and thus the heat flow transmitted from the compression volume to the cryocooler housing and the infrared module as a whole.

3. Radiation

Housing of the FPA is a Dewar of finite size, therefore, it is customary to calculate heat inleak due to radiative heat transfer according to the model of radiation heat transfer between the body and the shell (in some sources for a system consisting of two bodies, one of which is non-bent, and the other irradiates itself (bent)) [3]. To simplify further consideration, we denote all the values related to the outer wall of the housing of the "out" index, and the inner one, which is the outer wall of the holder with the "in" index. Obviously, in our system, the heat flow is directed from the outer wall to the inner wall and is calculated using equation:

$$Q_{\rm rad} = \sigma \times (T_{\rm out.}^4 - T_{\rm in}^4) \times \varepsilon_r \times F_{\rm in}, \tag{3}$$

where σ – Stefan-Boltzmann constant 5.7×10^{-8} W/(m²·K⁴), $T_{\rm out}$ – temperature of the outer wall, T_{in} – temperature of the inner wall, ε_r – reduced emissivity coefficient, F_{in} – area of the inner wall. The reduced emissivity coefficient in this model is calculated using equation:

$$\varepsilon_r = \frac{1}{\frac{1}{\varepsilon_{in}} + \left(\frac{1}{\varepsilon_{out}} - 1\right) \times \frac{F_{in}}{F_{out}}}$$
(4)

where $F_{\rm out}$ – area of the outer wall, $\varepsilon_{\it in}$ – emissivity coefficient of the inner wall, ε_{out} – emissivity coefficient of the outer wall. Obviously, in this model, as in radiation heat transfer in general, temperature makes the greatest contribution to the value of the heat flow. In this case, the temperature of the coldfinger along its length varies from the cryostating temperature (depending on the $4.2-150 \,\mathrm{K}$) to the ambient cryocooler temperature. Therefore, in order to obtain the correct values of heat flows, it is necessary to know temperature distribution along the length of the coldfinger, which is a difficult experimental issue, since coldfinger simultaneously acts as the wall of the Dewar and the wall of the expansion volume of cryocooler. But since the temperature at the cold end corresponds to the cryostating

temperature, and the values at the hot end are obtained paragraph 2, in then approximation, the temperature distribution over the holder can be obtained by solving the equation of stationary thermal conductivity. Using the Ansys package, importing a 3D model of the coldfinger, we set the boundary conditions: temperature of the cold end, temperature of the hot end, thermal conductivity dependance from temperature for coldfinge material, and we obtain a solution using the finite element method (FEM), then integral temperature of coldfinger is calculated, i.e. the inner surface of the T_{in} (Fig. 1a). Temperature of the outer wall is taken as the ambient temperature, taking into account the correction described in paragraph 2.

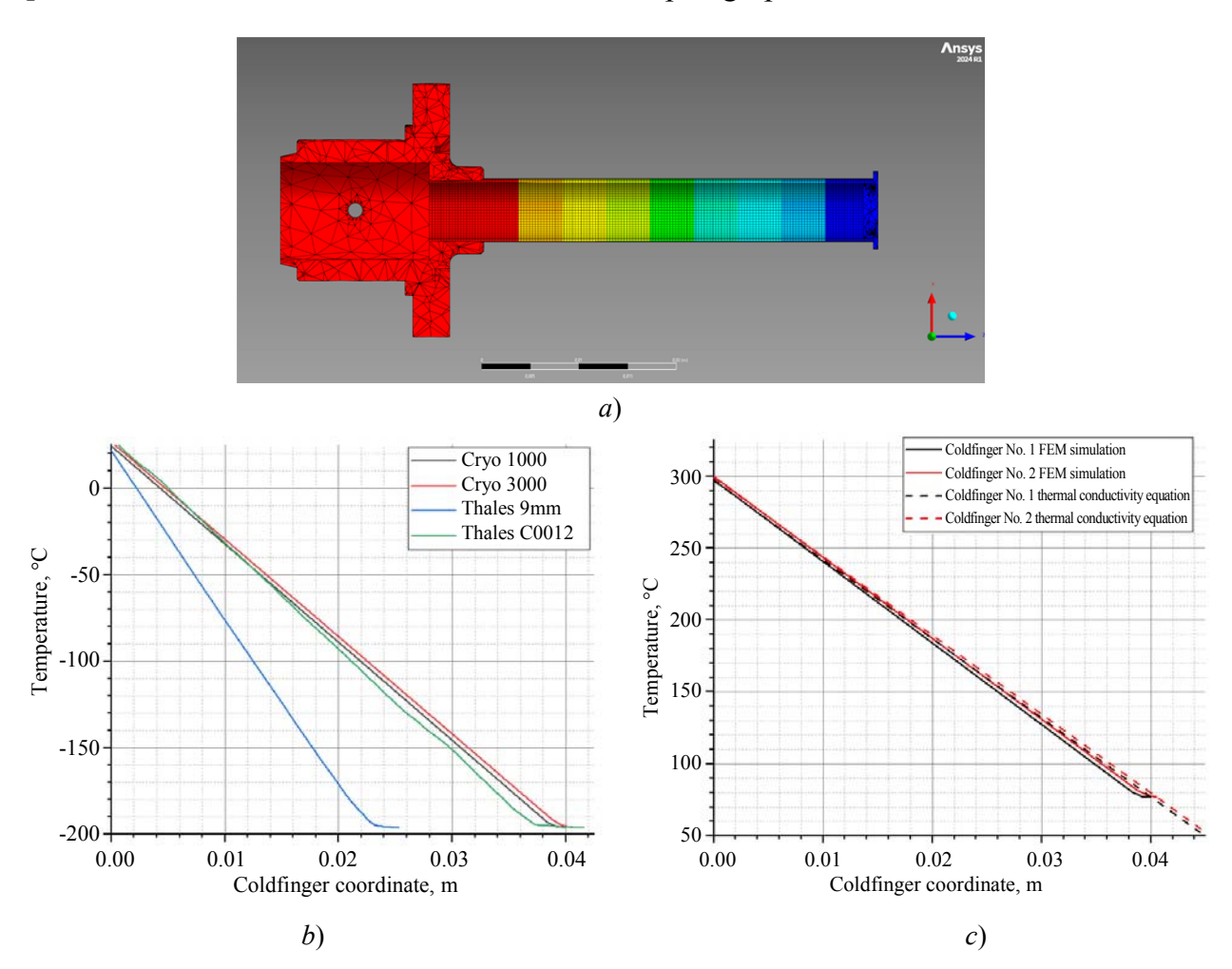


Figure 1. Temperature distributions along the coldfinger: a) temperature distribution obtained in the Ansys package by FEM; b) temperature dependence on the coordinate for different coldfingers; c) comparison of the distributions obtained from thermal conductivity equation and FEM on coldfingers without hybrid rings

For comparison, several coldfinger designs were taken (two manufactured by RD&P Center Orion and two manufactured by Thales, France) and the temperature dependence along the coldfinger was acquired for various materials (AISI 316, 321, L605). According to the results obtained, the main difference in temperature distributions was revealed. This difference is related to the

features of production technologies, namely, method of attaching disk to the tube. In the case of Thales coldfingers, hybrid soldering rings are used, which cause tube to thicken and, as a result, the temperature profile differs, namely, a plateau appears at the site of the thickening (Fig. 1b). Respectively, such coldfingers cannot be calculated within the framework of the thermal conductivity

equation of the tube due to its more complex shape and inhomogeneous materials. If hybrid rings are not used, then it is allowed to use the solution of the thermal conductivity equation for the tube. In this case, the temperature distributions differ slightly (Fig. 1c), by 0.6 % (170 μ W at normal climatic conditions), while greatly simplifying the implementation of the computational model.

4. ROIC and outputs

ROIC interacts with the environment through metal outputs, therefore part of heat flows to ROIC from outside through metal outputs, due to the temperature difference at their ends. Calculations are carried out according to formula (1). Practicability of calculating with the corrections described in paragraph 2, concerning the use of integral quantities, should be considered relative to the resulting value of heat flows without these corrections, depending on the design of the Dewar. In modern infrared modules, the difference between the heat inleak from the coldfinger and outputs is at least an order of magnitude, so the contribution of thermal conductivity corrections may not be crucial. As part of the work, an assessment was made to evaluate the correction influence on the thermal conductivity dependence on the temperature for materials commonly used in soldering outputs (gold, platinum). The following initial parameters were selected:

- Diameter $30 \mu m$;
- Totallength of outputs 15 cm;
- Outputs quantity 50;
- Temperature of cold end 77 K;
- Temperature of hot end 300 K;

As a result, for these initial parameters when using gold, a difference of 400 µW was obtained, i.e. 2.45 % of the value of heat due to the conclusions inleaks and 0.13–0.26 % of the total value of heat inleaks at FPA. And for platinum, 4 µW, i.e. 1.08 % of the value of heat inleaks due to the terminals and less than 0.003 % of the total value of heat inleaks at FPA. Accordingly, for such initial parameters, the use of correction is not necessary, especially when using platinum, because based on the available data [4–6], conductivity varies thermal slowly from a temperature in the range of 200–400 K, and the approximation of the data allows us to judge the same nature of the change in thermal conductivity up to 77 K. But when considering large diameters, lengths, and the number of pins, it is worth noting that the correction contribution will increase in proportion to the number of pins and the square of the diameter, while the dependence on the length of the pins is inversely proportional. Accordingly, for most modern infrared modules, correction for thermal conductivity of the output material can be ignored, and when calculating other structures, it can be evaluated relative to the initial data.

5. Model approbation

According to the results of calculations based on classical model and modified, Dewar of the FEM16-03 mass-production item, a decrease in heat inleaks due to thermal conductivity in the modified model by 17.6 % and by 5.6 % due to radiation was obtained. The calculated value was 243.5 mW, which brought it closer to the values measured on serial products.

	Classical model	Modified
Heat inleak from FPA and ROIC	40 mW	40 mW (did not change)
Heat inleak from outputs	14.1 mW	13.8 mW
Heat inleak from coldfinger thermal conductivity	176 mW	145 mW
Heat inleak from radiation heat transfer	47.4 mW	44.7 mW
Total heat inleak	277.5 mW	243.5 mW

6. Conclusions

Work has been carried out to adapt the classical model for calculating heat inleaks for Dewar assemblies of infrared modules. As a result of the adjustments, the values obtained have become closer to those measured on mass-produced devices, which is sufficient for evaluation during design development and material selection. It is revealed that when using hybrid rings when welding the coldfinger, in order to predict heat inleaks, it is worthwhile to calculate using the finite element method due to the heterogeneity of the cold end of the coldfinger. Also, the choice of the complexity of the model for accounting for heat flows from the outputs depends on the device (the number of outputs, their length and crosssection area). For a more accurate assessment and prediction of heat inleaks, certain improvements are required. namely, accounting for the operation of the reverse Stirling cycle in the regenerator and changes

in the temperature of the coldfinger tube, as well as more accurate accounting for the contribution of heat inleaks from compression volume and stator to coldfinger.

REFERENCES

- 1. Katz A., Segal V., Filis A., Haim Z., Nachman I., Krimnuz E. and Gover D., Proc. of SPIE. Infrared Technology and Applications XL **9070**, 90702N (2014). doi: 10.1117/12.2050317
- 2. https://trc.nist.gov/cryogenics/materials/materialproperties.htm
- 3. Solodov A. P., Otkrytoe obrazovanie, No. 1(96), 8–16 (2013).

https://doi.org/10.21686/1818-4243-2013-1(96)-8-16

- 4. Zinov'ev V. E. Teplofizicheskie svoistva metallov pri vysokikh temperaturakh: spravochnik. Moscow, Metallurgiya, 1989.
- 5. Vasil'eva E. V., Volkova R. M., Zakharova M. I. i dr. Platina, ee splavy i kompozitsionnye materialy / Pod red. Vasil'evoi E. V. Moscow, Metallurgiya, 1980.
- 6. Novitskii L. A. and Kozhevnikov I. G. Teplofizicheskie svoistva materialov pri nizkikh temperaturakh: spravochnik. Moscow, Mashinostroenie, 1975.

About authors

Dmitrii Dmitrievich Babenko, Candidate of Technical Sciences, senior research scientist of the department of vacuum structures and cryosystems, RD&P Center ORION, JSC (111538, Russia, Moscow, Kosinskaya st., 9). E-mail: rainbowdm1802@gmail.com SPIN code 9634-1880, Author ID 1172254

Maksim Viktorovich Bannikov, Acting Head of the department of vacuum structures and cryosystems, Deputy Head of the STS MFE, RD&P Center ORION, JSC (111538, Russia, Moscow, Kosinskaya st., 9). E-mail: maxnutnet@yandex.ru

Gleb Igorevich Nekrasov, Candidate of Technical Sciences, senior research scientist of the department of vacuum structures and cryosystems, RD&P Center ORION, JSC (111538, Russia, Moscow, Kosinskaya st., 9). E-mail: gleb.nekrasov.18@mail.ru SPIN code 6957-1320, Author ID 976504

=PHYSICAL EQUIPMENT AND ITS ELEMENTS =

UDC 53.06; 53.09 PACS: 42.55.Px

EDN: NMPYFE

Production of GeO₂-SiO₂ by ion sputtering for studying the generation of a laser diode with an external planar waveguide reflector

© M. A. Kononov*, V. V. Svetikov and V. I. Pustovoy

Prokhorov General Physics Institute, Russian Academy of Sciences, Moscow, 119991 Russia * E-mail: mike@kapella.gpi.ru

Received 25.03.2025; revised 16.04.2025; accepted 11.08.2025 Scientific specialty code: 1.3.19

The paper presents experimental studies of lasing of a broadband (100 µm) semiconductor laser in an external resonator based on a planar waveguide structure with a Bragg grating. The planar waveguide structure was fabricated on Si substrates with a SiO₂:GeO₂ waveguide layer with a contrast of 2.4 %. The waveguide layer film obtained by sputtering germanosilicate glasses GeO(0.5): $SiO_2(0.5)$ and GeO(0.5): SiO(0.5) with argon ions on cold Si(100) and fused quartz substrates in high vacuum. The operating modes of the ion source required for the formation of germanium nanocrystals in GeO:SiO and GeO:SiO₂ films were found. Then the films were annealed at temperatures up to 900 °C. The presence and phase composition of germanium nanoclusters in the films satisfied the necessary conditions for laser generation and the distribution of radiation in the far zone depending on the relative position of the planes of the LD waveguide and the waveguide of the external planar structure. It is shown that the high-order transverse mode predominates in laser generation, with a significant decrease in the spectral width of the radiation and stabilization of the spectrum in the entire range of operating currents. Laser generation on the nonradiative and leaky waveguide modes of the external planar structure is demonstrated.

Keywords: ion sputtering; laser generation; planar waveguide; waveguide mode; leaky mode.

DOI: 10.51368/1996-0948-2025-4-107-112

Introduction

Semiconductor lasers due to their high efficiency, small size and high manufacturability have become the most widespread among the coherent light sources.

Semiconductor lasers have proven to be in demand in such branches of science as materials processing, biomedicine, navigation, telecommunication, protection of facilities, as well as in many related sectors. According to the output power,

semiconductor lasers can be divided into low-power and high-power lasers. The former are mostly used in telecommunication applications, the latter are widely used in sensorics, biomedicine, navigation and materials processing.

The high-power lasers include lasers with an output power from several dozens milliwatts or higher. The simplest high-power lasers are lasers with wide contact. Due to the simplicity of design, such lasers are widely used, however, they have a significant drawback that severely limits their use. Due to the large length and wide contact due to which makes it possible to obtain high laser power, wide spectra of longitudinal and transverse modes are actuated, moreover, uncontrolled filamentation of the active area occurs [1–3]. Together, these factors greatly reduce brightness of the semiconductor laser. This condition is an obstacle to the use of such lasers in a wide range of applications in which there are no other competitors

by remaining criteria. In this regard, the selection of longitudinal and transverse modes is relevant for such lasers. To solve such problems along with special designs laser diode. different designs Two-arm external resonators are used. resonators (or V-resonators) [4–8] are quite effective geometries of external resonators, in each O-factor of one of the transverse achieve modes increases. To high effectiveness of such resonators, it is not enough to ensure only return angle of the feedback rays [8], it is also necessary to ensure spatiospectral filtration of the feedback radiation [4]. The method of spraying waveguiding layer, in contrast to the previously used methods [9–11], also applies to the solution of this problem. Method of ionic sputtering of target with the required composition with an ion source was applied earlier and described in previous works [12–14]. Figure 1 shows a scheme for producing GeO₂:SiO₂ films.

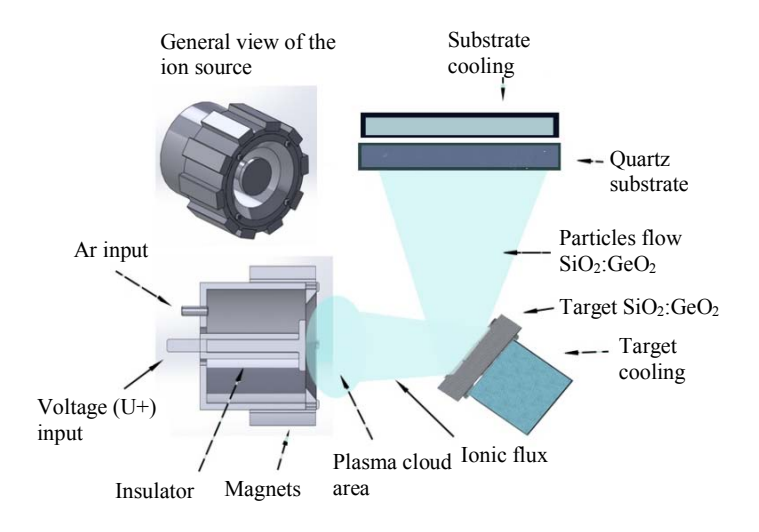


Fig. 1. Diagram of SiO₂: GeO₂ target spraying device

Sputtered waveguiding layer features

The designs of external resonators consist of number of external elements which require accurate adjustment with each other which often leads to the dependence of radiation parameters on external mechanical impact. In this regard, structures with one external elements performing functions of spectral, phase and spatial selector are of interest. This approach was implemented, for example, in the following works [15, 16].

The proposed designs used a planar digital hologram. The simplest hologram variant is Bragg grating. For high-power lasers such structures are implemented in the form of volumetric Bragg structures [17-20], which demonstrated high efficiency. To implement the design of the above structure thin films GeO; SiO and GeO:SiO₂ were obtained by simultaneous sputtering of a composite target of GeO₂ and SiO₂ using an Ar ion beam, energy of which varied from 2 to 4 KeV depending on the required film properties. The power of the ion beam that sprayed the target was chosen in a way that deposition of both components was It is known that when sputtering GeO₂ target

substrate, GeO_x layer deposits to the with stoichiometric parameter $x \sim 1$. Films deposited at a temperature of 100 °C to the substrates made of fused silica and Si (100). Thickness of films was \sim 750 nm. Then the films were cover with SiO₂ protective layer with a thickness of 10 nm to avoid evaporation of germanium monoxide during the anneal process [21]. After the satisfactory results have been obtained for spraying SiO₂:GeO₂ films with a suitable composition to study LD laser generation with a feedback mirror based on waveguide Bragg grating, a planar waveguide structure on a Si-substrate was manufactured (fig. 2).

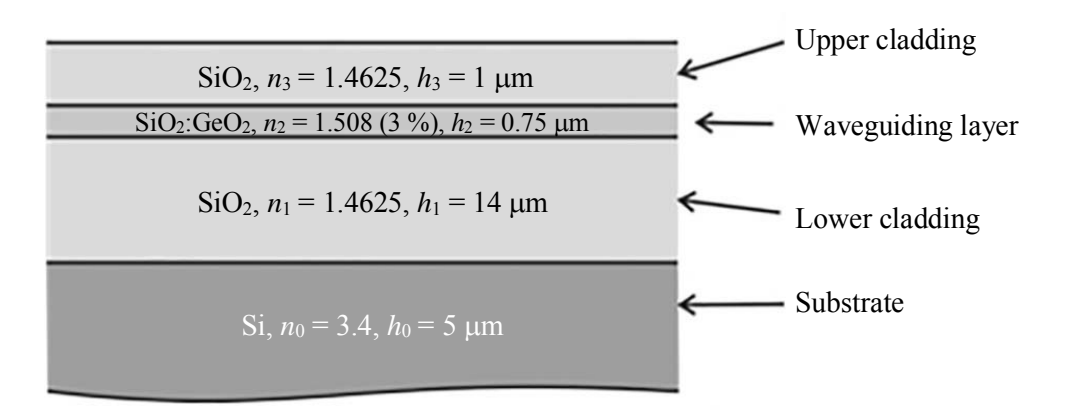


Fig. 2. Structure of the planar waveguide was used in the experiments

The structure was calculated to actuate one waveguide mode and consisted of two SiO_2 cladding layers and one SiO_2 :GeO₂ waveguiding layer. The bottom cladding layer with a thickness of $h = 14~\mu m$ isolated a waveguide mode from Si-substrate, upper layer with a thickness of $h = 1~\mu m$ protected the waveguide from environmental influence. Waveguiding layer was manufactured from SiO_2 :GeO₂ with index of refraction n = 1.492 which made up a 2.4% contrast to the index of reflection of the bottom cladding. The waveguiding layer thickness was equal to $h = 0.75~\mu m$. It follows from the calculation that the length of the main mode by field

amplitude at the 1/e is approximately 1.8 μ m. In terms of field intensity, the field width is approximately 1.3 um. This structure supports only one waveguide mode, other modes, actuated in the structure, are leaking modes to Si-substrate. The attenuation of cladding modes is by 9-10 orders of magnitude greater than the attenuation of the propagating main mode through waveguiding layer. Bragg grating with a period of $\lambda = 360$ nm was manufactured in waveguiding the structure by etching periodically arranged grooves on the surface of the waveguiding layer (layer SiO₂:GeO₂). Etching depth was 40 nm. The Bragg grating

was at a distance of 1 mm from the receiving ring of the planar waveguide, grating length – 1.6 mm.

Laser generation

A study of the laser generation of the diode laser with Bragg grating showed the possibility of stable generation with currents up to nominal $I_{rat} = 2$ A on two spectral lines: 1059.4 nm and 1067.1 nm (fig. 3).

Generation at wavelength $\lambda = 1067.1$ nm is possible in the entire operating wavelength range. At wavelength $\lambda = 1059.4$ nm, the generation is conducted only at continuous pumping currents of 400-500 mA, half the rated current $I < I_{rat}/2$ ($I_{rat} = 2$ A). At high pumping current, the generation spectrum consists either of one

line $\lambda = 1067.1$ nm or simultaneously of twoline 1067.1 nm and 1059.4 nm. In this case, the appearance of wavelength $\lambda = 1059.4$ nm in the generation spectrum occurs only when the planar waveguiding structure is shifted along the direction perpendicular to the planar waveguides plane by $\Delta z = 1.2-3.3$ µm upward relative to the position in which generation occurs on the spectral line $\lambda = 1067.1$ nm.

As indicated, agitation of two spectral bands happens only at pumping currents exceeding $I > 0.5I_{rat}$ (I > 1 A). In these cases the mode intensity at a wavelength of 1067.1 nm is approximately 3–5% of the mode intensity at $\lambda = 1059.4$ nm. This is fair for all cases, except for the case of vertical adjustment at $\Delta z = 3.3$ µm. In the last case the intensities of both spectral bands are approximately the same (fig. 4.).

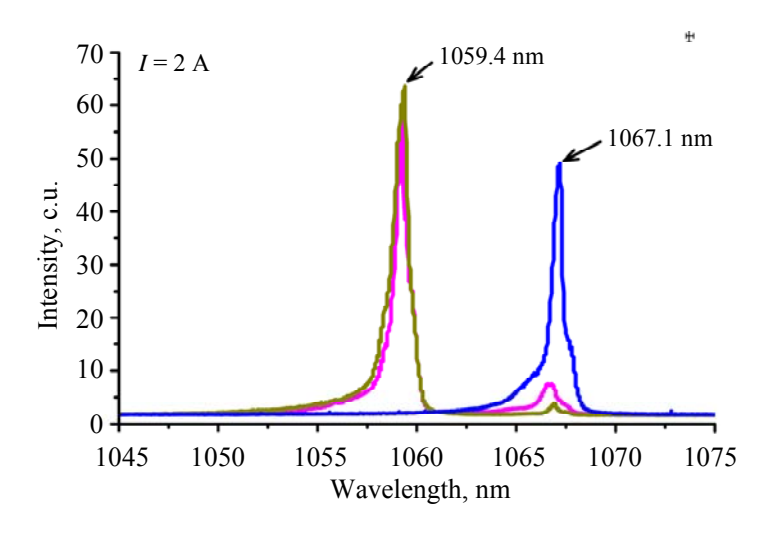


Fig. 3. Laser generation spectra of the diode laser with planar waveguiding Bragg grating at nominal control current I = 2 A with different mutual arrangement of LD waveguide planes and external structure (blue curve: alignment of the LD planes and external structure waveguide plane; purple curve: disalignment of planes by 1.2 µm; gray curve: disalignment of planes by 3.3 µm)

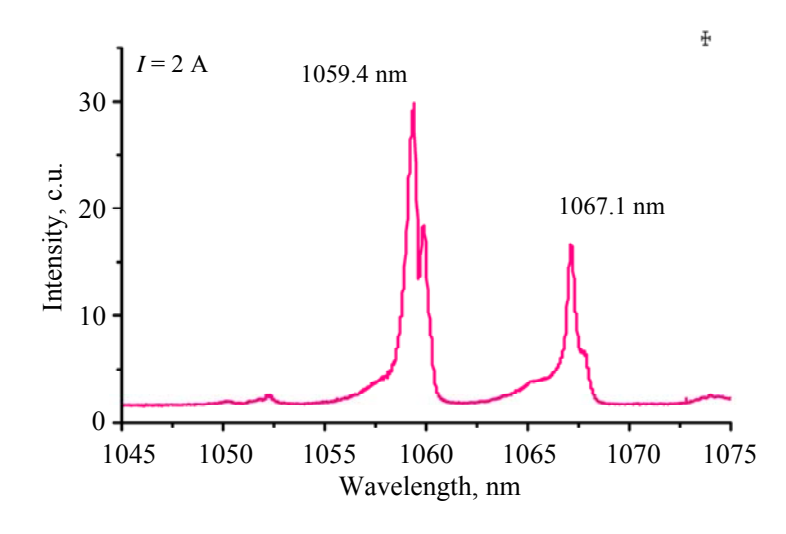


Fig. 4. Laser diode generation spectrum at vertical disalignment of LD waveguide and external structure waveguide planes by $\Delta z = 3.3 \ \mu m$

The presence of two spectral bands of laser generation appears to be associated with actuation of the main and first cladding modes of the planar waveguide. Within the framework of this mode, the generation wavelength of 1067.1 nm corresponds to the main mode of the planar waveguide, at the same time, the wavelength of 1059.4 nm corresponds to the cladding mode. By the difference in generation wavelengths, it is possible to determine the difference in effective reflection indicants actuated in the planar modes waveguide:

$$\Delta n_{0-1}^* = \frac{\lambda_0 - \lambda_1}{2\Lambda}$$

where λ_0 and λ_1 – generation wavelengths (Bragg wavelength: $\lambda_1 = 2\Lambda n_1^*$, $\lambda_2 = 2\Lambda n_2^*$), n_1^* and n_2^* – effective reflection indices of the planar waveguide modes.

In our case $\lambda_1 - \lambda_2 = 7.7$ nm, which according to the equation (1) corresponds to the difference in effective reflection indices $\Delta n^* = 0.0107$.

Conclusion

It was shown that using the method of ionic sputtering of composite GeO₂ and SiO₂ target you can obtain waveguide layers suitable for research. Based on the proposed technology, the laser generation of a wideband semiconductor laser diode with a planar waveguide Bragg mirror in the external resonator was studied. When using waveguides with a contrast range of 3 % and a lensless connection between the LD and planar waveguide, it was shown that the laser generation is stable up to the nominal pumping currents of LD. Laser generation was observed, the intensity distribution in the far filed which corresponds the predominance of a high-order transverse

mode with a transverse period of about 12 μm.

REFERENCES

- 1. Thompson G. H. B., Opto-electronics **4**, 257 (1972).
- 2. Bachert H.-U., Bogatov A. P. and Eliseev P. G., Quantum Electronics **5** (3), 603 (1978).
- 3. Goldberg L., Surette M. R. and Mehuys D., Appl. Phys. Lett. **62**, 2304 (1993).
- 4. Raab V. and Menzel R., Optics Letters **27** (3), 167 (2002).
- 5. Thestrup B., Chi M. and Petersen P. M., Proc. SPIE **5336**, 39 (2004).
- 6. Jechow A., Raab V., Menzel R., Cenkier M., Stry S. and Sacher J., Optics Communications **277**, 161 (2007).
- 7. Svetikov V. V. and Nurligareev D. H., Quantum Electronics **44** (9), 810 (2014).
- 8. Svetikov V. V. and Kononov M. A., Quantum Electronics **48** (8), 706–710 (2018).
- 9. Astankova K. N., Gorokhov E. B., Volodin V. A., Marin D. V., Azarov I. A. and Latyshev A. V., Russian nanotechnologies **11** (5–6), 59 (2016).
- 10. Gorshkov O. N., Dudin Yu. A., Kamin V. A. et al., Letters to the Journal of Technical Physics **31** (12), 39–47 (2005).
- 11. Hansperger R. Integral Optics: Theory and Technology: Trans. from English. Moscow: Mir, 1985.
- 12. Burkhanov G. S., Lachenkov S. A., Bashlakov A. U., Kirillova V. M., Sdobyrev V. V. and Kononov M. A.,

Inorganic Materials: Applied Research 13 (2), 466–472 (2022).

- 13. Burkhanov G. S., Lachenkov S. A., Kononov M. A., Bashlakov A. U., Kirillova V. M. and Sdobyrev V. V., Advanced materials, № 10, 37–46 (2021).
- 14. Burkhanov G. S., Lachenkov S. A. and Kononov M. A., Journal of Physics: Conference Series 012033 (2018).
- 15. Svetikov V., Ivonin I., Koshelev A.; Velikov L., Vorobiev Yu., Goltsov A. and Yankov V., Proceedings of SPIE **7918**, 79180P (2011).
- 16. Svetikov V., Peroz C., Ivonin I., Dhuey S., Cabrini S., Babin S., Goltsov A. and Yankov V., J. Opt. Soc. Am. B **30** (3), 610–614 (2013).
- 17. Helan Mikel R., Cip O. and Jedlicka P., Proc. of SPIE **7155**, 71552T (2008).

- 18. Stolpner L., Lee S., Li S., Mehnert A., Mols P., Siala S. and Bush J., Proc. of SPIE **7004**, 700457 (2008).
- 19. Alalusi M., Brasil P., Lee S., Mols P., Stolpner L., Mehnert A. and Li Steve, Proc. of SPIE **7316**, 73160X (2009).
- 20. Venus G. B., Sevian A., Smirnov V. I. and Glebov L. B., Proc. of SPIE **5711**, 166–176 (2005).
- 21. Vinogradov S. V., Kononov M. A., Savranskii V. V. and Valyanskii S. I., Bulletin of the Lebedev Physics Institute **2**, 3 (2003).

About authors

Mikhail Anatolevich Kononov, Candidate of Physical and Mathematical Sciences, senior research scientist Prokhorov General Physics Institute, Russian Academy of Sciences (119991, Russia, Moscow, Vavilova 38 st.) E-mail: mike@kapella.gpi.ru SPIN code 8607-2597, Author ID 30241

Vladimir Vasilievich Svetikov, Candidate of Physical and Mathematical Sciences, research scientist Prokhorov General Physics Institute, Russian Academy of Sciences (119991, Russia, Moscow, Vavilova 38 st.) E-mail: vl.svetikov@gmail.com SPIN code 7500-2560, Author ID 30329

Vladimir Ivanovich Pustovoi, Head of the Laser Physics Department, Prokhorov General Physics Institute, Russian Academy of Sciences (119991, Russia, Moscow, Vavilova 38 st.) Author ID 18514

PHYSICAL EQUIPMENT AND ITS ELEMENTS

UDK 536.331 PACS: 44.40.+a

EDN: GELGTW

Silicon wafer switching dynamics from low temperature to high temperature state in bistable mode of radiation heat exchange with elements of a lamp reactor

© V. V. Ovcharov^{1,2,*}, F. L. Kurenya¹ and V. P. Prigara¹

¹ Yaroslavl Department of Valiev Institute of Physics and Technology "NRC "Kurchatov Institute", Yaroslavl, 150007 Russia

* E-mail: ovcharov.vlad@gmail.com ² Yaroslavl State Agrarian University, Yaroslavl, 150042 Russia

Received 9.01.2025; revised 14.02.2025; accepted 11.08.2025 Scientific specialty code: 1.3.11; 1.3.14

The switching dynamics of a silicon wafer from low temperature to high temperature states in the thermal reactor of the thermogradient treatment setup has been experimentally and theoretically carried out under conditions far from thermodynamic equilibrium. The simulation of the switching process in the silicon wafer has been considered with regard to radiative absorber temperature versus temperature of heater. The comparison of the experimental data and the calculated results has been made. It is shown that when the control switching signal values on the lamp block of the reactor exceed the critical value, the effect of critical delay (slowing down) has been observed, significantly increasing the switching time of the wafer.

Keywords: radiation heat exchange; optical and temperature bistability; the effect of critical delay (slowing down); a thermal reactor; a silicon wafer; an effective heat exchange coefficient; a radiative absorber.

DOI: 10.51368/1996-0948-2025-4-113-118

Introduction

In recent decades, the phenomenon of bistability has been extensively optical its relevance studied due to the development of optical logic devices [1]. Theoretical work in [2] demonstrated the potential for temperature bistability to occur during natural radiative heat exchange in a material whose emissivity sharply increases with temperature. The initial experimental observation of temperature and optical bistability during radiative heat exchange was reported in [3] for a silicon wafer within the thermal reactor of a rapid thermal processing setup, where a comprehensive theoretical analysis of this phenomenon under steadystate heat exchange conditions was also performed. The time required to achieve a steady-state heat exchange mode between the wafer and the thermal reactor components, depending on the heater temperature, ranges from 5 to 10 minutes. However, the duration processes of rapid thermal in

microtechnology, for which this effect is intended, currently ranges from 10⁻⁴ to 10² s [4, 5]. These processes take place under non-stationary conditions, making it essential to understand how the bistability effect behaves during such brief thermal process durations.

The objective of this study is to experimentally and theoretically investigate the dynamics of switching a silicon wafer from a low-temperature to a high-temperature state in a bistable heat exchange mode between the wafer and the components of the thermal reactor in a rapid thermal processing setup.

Thermal reactor model

An experimental study of the switching dynamics of a silicon wafer was conducted using a thermal gradient wafer processing system, which is described in detail in [6]. The block diagram of the installation's working chamber is provided in [6], while a schematic of its reactor is shown in Fig. 1. steady-state mode, the wafer temperature was measured with a cromelalumel thermocouple, while its optical properties were monitored using an M680 pyrometer equipped with a silicon sensor, following the method outlined in [3]. In the non-stationary mode. temperature measurement with the thermocouple proved ineffective due to its response lag, and only the optical properties of the wafer were directly monitored using the pyrometer. The correspondence between the pyrometer readings and the wafer temperature was determined through calculations based on the method developed in [3].

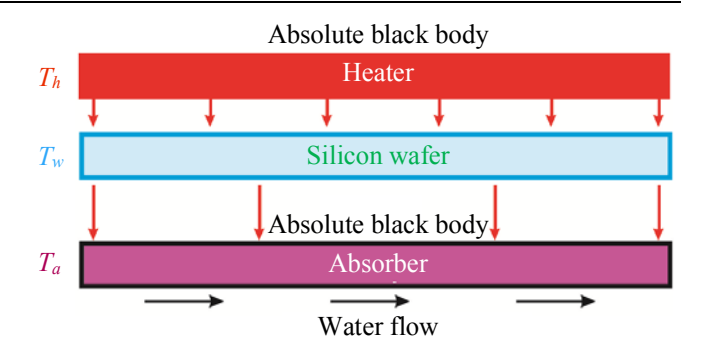


Fig. 1. Model of a thermal reactor for a thermal-gradient wafer processing setup

Experimental results

The experimental procedure is shown in Fig. 2. Figure 2b displays a steady-state thermal hysteresis loop representing the heating process (red solid line curve) and cooling process (blue dotted line curve) of a silicon wafer inside a thermal reactor (refer to [3]). The figure 2a shows the pyrometric curve corresponding to the temperature hysteresis loop. Following the preheating of the wafer (point 0 on the temperature and pyrometric transfer characteristics), a series of staircase waveform voltage signals with progressively increasing amplitude is applied to the lamp unit. It is assumed that at low amplitudes, the silicon wafer stays in a lowtemperature state until reaching a specific critical amplitude ΔU_{cr} , after which it shifts to a high-temperature state (point F). This transition corresponds to the critical delaying (or slowing down) effect described in [7–9]. When the switching signal amplitudes approach critical values, the time required for the wafer to transition from a lowtemperature state to a high-temperature state can become significantly prolonged.

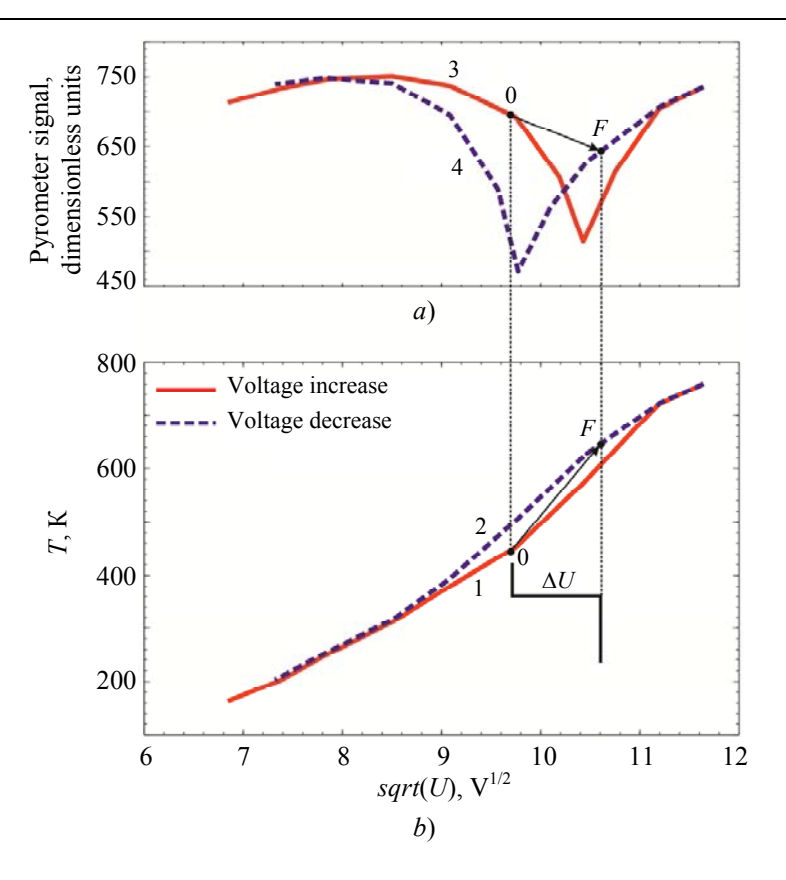


Fig. 2. The representative point shift from the low-temperature branch (position 0) to the high-temperature branch (position F) of the silicon wafers transfer characteristic occurs when a step voltage is applied to the lamp unit of the rapid thermal processing setup.

(a) pyrometric characteristic; (b) temperature transfer characteristics

Fig. 3 shows how the readings of two different pyrometric sensors vary over time when the wafer is subjected to a sudden change in the flux density of incoherent radiation. The first sensor measured lamps radiation, while the second sensor, positioned beneath the silicon wafer, detected combined radiation transmitted and the wafer's own radiation. The readings from the first sensor are represented by the staircase curves in the upper part of the figure. The amplitudes of the switching signals are shown in the figure legend and correspond the different colors of the curves. The pyrometric curves recorded by the second sensor positioned beneath the wafer are displayed at the bottom of the figure. The curves recorded by the first and second share the same colors for sensors ΔU . corresponding amplitude values

The interpretation of the second pyrometer's readings is described in [10]. Four distinct sections may be identified on the pyrometric curves recorded by the second sensor. In the first section, a sharp peak is observed, corresponding to a voltage surge in the lamp unit. During the second section, the pyrometric signal decreases from its peak to its lowest point, indicating that the silicon wafer's absorptivity increases while its decreases with transmittance rising temperature. In this area the flux density of the transmitted radiation exceeds that of the wafer's own radiation. The third section represents the increase of the pyrometric signal from its minimum level to the value corresponding to the wafer's steadystate temperature. In this section, the flux density of the wafer's own radiation surpasses that of the radiation transmitted through it.

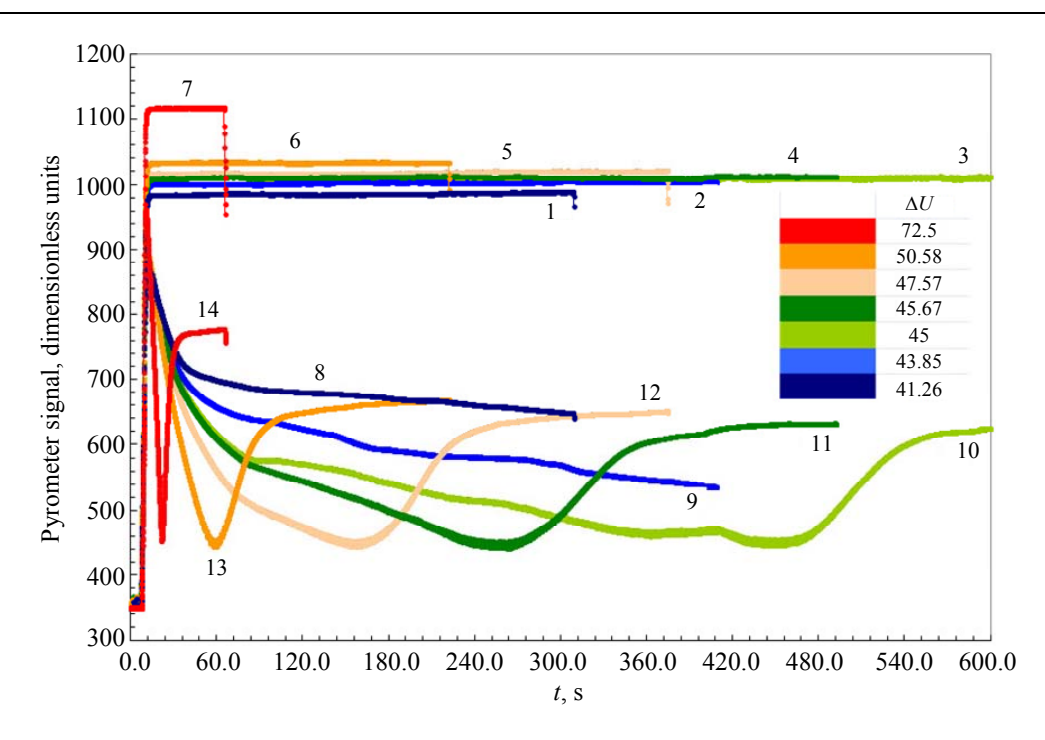


Fig. 3. Pyrometric curves taken by the radiation sensors of the M680 pyrometer.

The upper curves represent the radiation from the lamps, while the lower curves correspond to the combined radiation: the portion that passed through the silicon wafer along with the wafer's radiation

Simulation of the switching process of a silicon wafer and discussion of the results

Figure 4 presents set of curves illustrating how the temperatures of the silicon wafer and the absorber (assuming the absorber's temperature varies during heat exchange with the silicon wafer and the heater), as well as the signal from the pyrometer positioned beneath the silicon wafer, change over time following a sudden rise in the heater temperature from 300 K to the maximum value $T_{h\text{max}}$. The value of $T_{h\text{max}}$ varies from 1220 K, where the wafer stays in a lowtemperature state, to 1255 K, at which point the wafer quickly transitions to a high-temperature state. The temperature variations of the silicon wafer and absorber over time were determined by solving a system of transient heat balance equations for the wafer and absorber, which were derived in [11] using the gray body approximation. In the calculations, the silicon wafer thickness was assumed to be 450 μm. The remaining parameters were chosen to maximize the similarity between the theoretical and experimental pyrometric

curves.
$$h_{\text{eff}} = 50 \text{ W/(m}^2 \cdot \text{K}), h_1 = 80 \text{ W/(m}^2 \text{K}),$$

 $c_a \rho_a d_a = 5 \times 10^3 \text{ J/(m}^2 \cdot \text{K}), T_0 = 300 \text{ K}.$

The analysis of Fig. 4b indicates that the critical maximum heater temperature $T_{h\text{max}}$ falls between 1220 and 1221 K. At $T_{h\text{max}} = 1220 \text{ K}$, the silicon wafer remains in a low-temperature state (black curves), while at $T_{h\text{max}} = 1221 \text{ K}$, it shifts to a hightemperature state, although with a significant delay of ~ 3000 seconds. In Fig. 4a, the lowtemperature state is represented by the highest (black) pyrometric curve, indicating the wafer's translucent state. The switching of the plate in Figure 4a corresponds to the purple curve, and the jump in the plate temperature during its switching corresponds to a sharp minimum on the pyrometric curve. An additional increase in temperature, up to $T_{h\text{max}} = 1228 \text{ K}$, does not alter the shape of the temperature and pyrometric curves. It only shifts the temperature jump associated with the wafer's transition to the high-temperature state to the left along the time axis. Simultaneously, the maximum temperature of the silicon wafer, around 1200 K, remains

practically unchanged. Further increasing $T_{h\text{max}}$ not only shortens the wafer switching time but also results in a rapid increase in its maximum temperature. Thus, a rise in $T_{h\text{max}}$

by 17 K, from 1228 to 1255 K, results in an increase of 200 K in the maximum temperature (as shown by the red curves in Figures 4a and 4b).

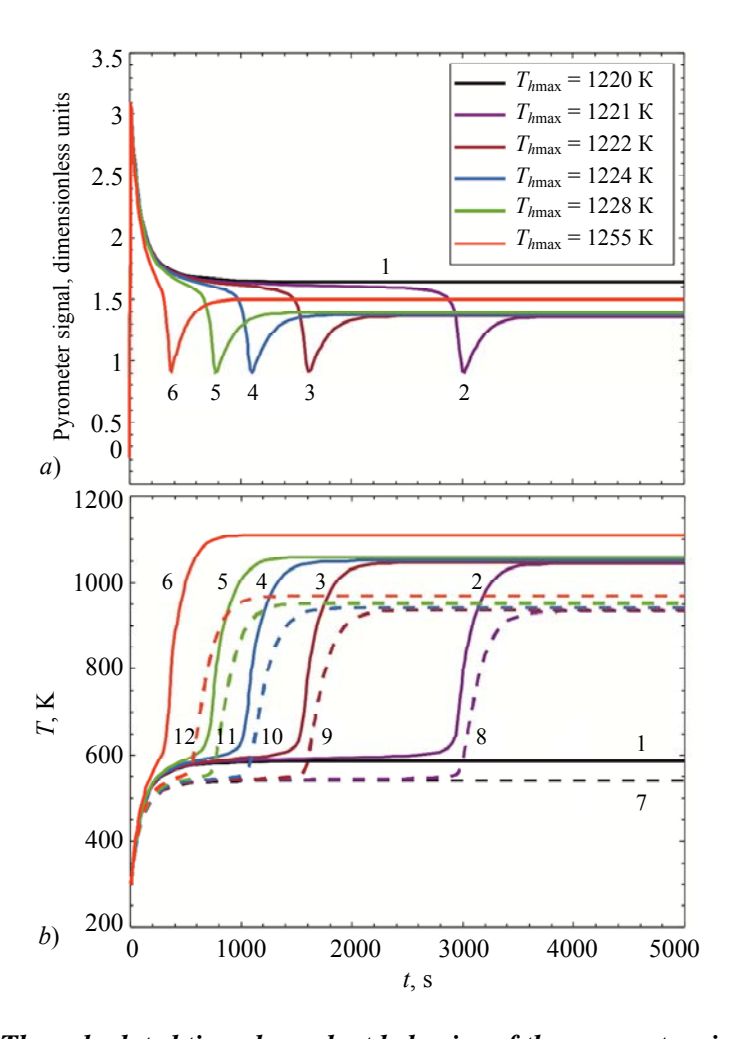


Fig. 4. The calculated time-dependent behavior of the pyrometer signal (a), along with the temperature of the silicon wafer (solid lines) and the absorber (dashed lines) (b), is shown during a stepwise increase of the heater temperature from 300 K up to T_{hmax}

A comparison between the experimental pyrometric curves (Fig. 3) and the calculated ones (Fig. 4a) indicates that the critical voltage surge amplitude on the ΔU_{cr} lamp unit lies between 41.26 and 43.85 V. The shift minimum of the experimental pyrometric curve as the switching voltage amplitudes range from 43.85 to 47.57 V without any change in the value of the pyrometric curve in the final section suggests the presence of a critical delay in the transition of the silicon wafer a low-temperature to a high-temperature state.

A further increase ΔU results in a significant decrease in switching time and an elevation in wafer temperature, aligning with the behavior of the theoretical curves.

Conclusion

The paper explores the dynamics of switching a silicon wafer from a low-temperature to a high-temperature state as it relates to the magnitude of the voltage surge on the lamp unit of a thermal gradient wafer processing system. A comparison between the

experimental data and the results of numerical simulations was conducted. It is demonstrated that a critical value ΔU_{cr} exists at which the wafer switching takes place. Experimental evidence has confirmed the presence of the phenomenon of critical delaying (slowing down) during plate switching in a thermal reactor when amplitude values ΔU exceed the critical threshold.

The paper has been prepared as part of the state assignment of the K.A. Valiev Physics and Technology Institute of the National Research Center "Kurchatov Institute" named after. K. A. Valiev on topic No. FFNN-2022-0018.

The authors declare that they have no conflict of interests.

REFERENCES

- 1. Gibbs H. M., Optical bistability: controlling Light with lighte. NY, Academi Press, Inc., 1985.
- 2. Rudakov V. I., Ovcharov V. V. and Prigara V. P., Technical Physics Letters **34**, 718–721 (2008). doi: 10.1134/S1063785008080282.

- 3. Rudakov V. I., Ovcharov V. V., Kurenya A. L. and Prigara V. P., Microelectronic engineering **93**, 67–73 (2012). doi: 10.1016/j.mee.2011.11.018.
- 4. Kennel H. W., Giles M. D., Diebel M., Keys P. H., Hwang J., Govindaraju S., Liu M. and Budrevich A., 14th IEEE International Conference on Advanced Thermal Processing of Semiconductors RTP. Kyoto, 2006, pp. 85–91. doi: 10.1109/RTP.2006.367986.
- 5. Alptekin E., Ozturk M. C. and Misra V., IEEE Electron Device Lett. **30** (4), 331–333 (2009). doi: 10.1109/LED.2009.2014182.
- 6. Mochalov B. V. and Rudakov V. I., Instruments and Experimental Techniques **39** (2), 302–304 (1996).
- 7. Tredicce J. R., Lippi G. L., Mandel P., Charasse B., Chevalier A. and Picqué B., American Journal of Physics **72** (6), 799–809 (2004). doi: 10.1119/1.1688783.
- 8. Garmire E., Marburger J. H., Allen S. D. and Winful H. G., Applied Physics Letters **34** (6), 374–376 (1979). doi: 10.1063/1.90794.
- 9. Lyubin V. M. and Tikhomirov V. K., JETP letters **55** (1), 23–26 (1992).
- 10. Ovcharov V. V., Kurenya A. L., Rudakov V. I. and Prigara V. P., International Conference on Micro-and Nano-Electronics 2016. SPIE **10224**, 510–521 (2016).

doi: 10.1117/12.2266553.

11. Rudakov V. I., Kurenya A. L., Ovcharov V. V. and Prigara V. P., International Conference Micro-and Nano-Electronics 2012. SPIE **8700**, 59–69 (2013). doi: 10.1117/12.2018016.

About authors

Vladimir Viktorovich Ovcharov, Candidate of Physical and Mathematical Sciences, senior research scientist, Yaroslavl Department of Valiev Institute of Physics and Technology "NRC "Kurchatov Institute" (150007, Russia, Yaroslavl, 21, Universitetskaya); Yaroslavl State Agrarian University (150042, Russia, Yaroslavl, 58, Tutaevskoe highway). E-mail: ovcharov.vlad@gmail.com SPIN code 6897-2529, Author ID 9065

Alexey Leonidovich Kurenya, leading electronics engineer, Yaroslavl Department of Valiev Institute of Physics and Technology "NRC "Kurchatov Institute" (150007, Russia, Yaroslavl, 21, Universitetskaya). E-mail: ftian.alex@mail.ru

Valeria Pavlovna Prigara, Candidate of Physical and Mathematical Sciences, research scientist, Yaroslavl Department of Valiev Institute of Physics and Technology "NRC "Kurchatov Institute" (150007, Russia, Yaroslavl, 21, Universitetskaya). E-mail: prigalera@yandex.ru SPIN code 4903-1219, Author ID 138758

= INFORMATION =

Rules for submission, reviewing and publishing of scientific papers (as revised in 2025)

1. The "Applied Physics" journal is mainly intended for urgent publication of short papers concerning recent achievements in physics that have a potential of applied (technical and scientific) use. The journal is included in the new List of the Higher Attestation Commission, which came into effect on December 1, 2015.

By sending the article manuscript to the journal's editorial board, the authors grant the editorial board, founder and publisher of the journal a free, non-exclusive right to publish it in Russian as an article in the printed version of the journal, in the electronic version of the journal in the Internet and on laser disks. At the same time the authors retain their intellectual rights to the article manuscript (including "copyright"). In this regard and considering Part Four (Section VII) of the Civil Code of the Russian Federation, the authors shall submit a letter to the editor in the following form:

License agreement for transfer of the publish right (publishing license agreement)

We,	the undersigned, the manuscript authors,	
grant the ed	ditorial board, founder and publisher of "Applied Physics" journal a free, simple (non-exclusive)	license to
publish the	article manuscript in both printed and electronic journal versions.	
We o	confirm that this publication does not violate the intellectual rights of other persons or organizations.	Signatures
of authors: _	(full name, academic degree, date)	

The article shall be signed by all authors. If there are several authors, the name of the author responsible for message exchange with the editorial board shall be indicated. The article manuscript shall be sent to the address of the journal's editorial board: 111538, Moscow, Kosinskaya st, 9, AO NPO Orion, editorial board of "Applied Physics" journal or by e-mail: advance@orion-ir.ru

- 2. The article manuscript shall be submitted to the editor only in Russian.
- 3. The article manuscript shall be accompanied by an expert opinion whether its publication in the open media is allowed, which shall be drawn up in accordance with the established procedure.
- 4. The article size (including figures, bibliography and the English-language part) shall not exceed **7 pages** of A4 format with single line spacing. (A larger article is proposed to be sent to the affiliated "Applied Physics Advances" journal intended for publication of detailed articles and reviews). The article material shall be submitted in printed form (on paper) and in electronic form on a CD/DVD disk with the text in Word format (font type Times New Roman, font size 12), and the text shall already include figures with captions under them in the proper places. However, overly detailed and cumbersome mathematical transformations and expressions should be avoided in the text. The article styling shall be as follows:
 - title of the journal section;
 - UDK index;
 - PACS classification code (https://publishing.aip.org/wp-content/uploads/2019/01/PACS 2010 Alpha.pdf);
 - article title;
 - initials and surnames of authors;
 - abstract of the article (10–15 lines describing the purpose of the paper and its main findings);
 - keywords;
 - scientific specialty code.
- 5. The main text of the article shall begin with the "Introduction" section clearly stating the purpose and objectives of the paper along with arguments in favor of its preparation against the background of the existing state of the problem addressed in the article. The further text of the article shall also have meaningful headings (sections and subsections) without being numbered. The article shall end with a separate section, "Conclusion," listing the main findings, conclusions that follow from them, and, if possible, proposals for the research advance and use of its findings.

The bottom of the first page of the text shall accommodate a separate paragraph (in bold) containing contact information about the author (or authors) (mandatory section): surname, first name, patronymic (in full), e-mail (of all authors), profiles and registration numbers in scientometric databases (SPIN code, RINTS Author ID, ArXiv Author ID, Orcid ID, Scopus Author ID), academic degree, title, position, postal address of the enterprise).

Also a person responsible for message exchange with the editorial board shall be specified.

Authors can suggest potential reviewers (2–3 people by indicating their full name, place of work, and email address). The proposed candidates shall not work in the institutions where the authors do.

120 Information

The main text shall be followed by the list of references called "Bibliography".

Examples of designations of references used in the "Bibliography" section.

Articles shall be referred to as follows: Surname, initials, journal title, year, volume, issue, page numbers.

Ivanov I. I. / Applied Physics. 2022. No. 1. P. 12–18.

Lang D. V. / J. Appl. Phys. 1974. Vol. 45. No. 7. R. 3023-3034.

Reference to **books**: Surname, initials, book title, city, publisher, year. (When a specific chapter or page in a book is referred to, the page number is placed after the year.)

Korn G., Korn E. Mathematical Handbook. - Moscow: Nauka, 1974.

Biberman L. M., Vorobiev V. S., Yakubov I. T. Kinetics of non-equilibrium low-temperature plasma. – Moscow: Nauka, 1982. P. 371.

Ultraviolet technologies in the modern world / edited by Karmazinov F.V. Kostyuchenko S.V., Kudryavtsev N.N. – Dolgoprudny: Intellekt, 2012.

Reference to **conference proceedings:** Surname, initials, title of publication, place and date of publication, page numbers.

Romanov A. V., Stepovich M. A., Filippov M. N. / Proceedings of the XVII International Conference "Radiation Physics of Solids". – Sevastopol, 2007. P. 592–599.

Reference to patents: Surname, initials, title, type, number, year.

Davydov S. G., Dolgov A. N., Yakubov R. H. Vacuum spark gap. Patent of invention No. 2654494 (RF). 2018.

Reference to **dissertations and Abstracts**: Surname, initials, title of paper (abstract), diss. ... Candidate (Doctor) of Physics and Mathematics, city, organization, year.

Grechikhin V. A. Development and analysis of computer algorithms for processing single-particle signals of laser Doppler anemometers: Abstract from diss. by Candidate of technical sciences. – Moscow: MPEI, 1996.

Further, detailed English-language information about the article required for indexing the entire journal, the given article and its authors in international scientometric databases shall follow, namely: PACS, article title, authors' surname and initials (English transliteration), enterprise, its postal address, author(s) e-mail, abstract, keywords, references; since the journal is also distributed abroad, the editorial board reserve the right to correct the English part of the text without changing its meaning.

Styling of the References in the English part of the article has its own peculiarities. In particular, if the cited book or monograph is a translation into Russian from a foreign publication, the original data of this publication (authors, book title, publisher, city or country, year of publication) shall be given, as well as the Russian publisher and the year of publication in Russian. Given below are the main examples of designation of used references in the References section:

Article from the journal:

Ivanov I. I., Applied Physics, No. 1, 12–18 (2022) [in Russian].

Lang D. V., J. Appl. Phys. 45 (7), 3023–3034 (1974).

Note: if a Russian journal has a printed English analogue, the English title of the analogue shall be used and page numbers shall be taken therefrom. If there is no English analogue, the English transliteration of the Russian name shall be used.

Book:

Korn G. and Korn E., Mathematical Handbook. New York-London, Mcgraw-Hill Book Company, 1968; Moscow, Nauka, 1974.

Ultraviolet technologies in the modern world / ed. Karmazinov F. V., Kostyuchenko S. V., Kudryavtsev N. N. Dolgoprudny, Intellect, 2012 [in Russian].

Conference proceedings:

Romanov A. V., Stepovich M. A., and Filippov M. N. Proc. XVII Intern. Meeting on Radiation Physics of Solid State. Sevastopol, 2007, pp. 592–599.

Patents:

Davydov S. G., Dolgov A. N., Yakubov R. H. Vacuum spark gap. Patent for invention No. 2654494 (RF). 2018. **Dissertations and Abstracts**:

Grechikhin V. A. Development and analysis of computer algorithms for processing single-particle signals of laser Doppler anemometers: Abstract. Diss. Candidate of Technical Sciences. M., MEI, 1996.

6. The list of references ("References") shall correspond to all references to external sources used in the text of the article. These references shall be enclosed in square brackets, for example, [1–3], [7, 8]. Internal references, i.e. references to formulas, figures and tables of the article shall be enclosed in round brackets, for example, formula (3), equation (1), (Fig. 2), (Table 3). Any references in figure captions or in the figures are not recommended.

Information 121

7. The number of figures and photos for a typical article shall not exceed 4. If one figure contains two, three or more variants of graphic (or photo) images of the type "Fig. 2a", "Fig. 2b", etc., each individual variant is considered as a separate figure. If the above limit number of figures (photos) is exceeded, the article is sent back to the authors for revision. Graphics (black and white and color) shall be put directly in the proper place in the article and in the proper scale. Next to the graph axes, the displayed physical quantities shall be indicated only (strictly!) using symbols (letters), and after a comma - the quantity dimension in Russian (in direct font). It is recommended to number different curves on graphs, even if they are identified by a different color or line type. Graphs shall be submitted only (strictly!) against the white background. Auxiliary grids are not allowed in the graph area.

- 8. Captions under the corresponding figures shall be out in the proper places in the text. Each caption shall be as short as possible, but meaningful in terms of its content. Any physical (technical) symbol included in the caption shall have its verbal explanation there.
- 9. Simple formulas shall be included in the text in the format of the text editor used; more complex formulas shall included using MathType formula editor. Standard mathematical notations (e.g. max, log, sin, exp, etc.) shall be typed directly. The same is true about figures and numbers. Formula numbers shall written in parentheses on the right. To indicate non-vector physical (technical) quantities using symbols, use only the Latin and Greek alphabets, while using a straight font for Greek letters, and an oblique font (italics) for Latin letters in the text. Vectors and matrices shall be marked by a bold, upright font (preferred) or an arrow above the italic vector symbol (less preferred). For subscripts and superscripts, use Arabic numerals, Latin or Greek letters, but if the index, usually a subscript, is a short (abbreviated) form of the Russian characteristic word, it is allowed to use Russian letters in its designation (uppercase font), for example $U_{\rm in}$, $I_{\rm out}$, $v_{\rm gr}$, etc. The dimension of physical quantities shall be always given only in Russian, using an uppercase font.
- 10. Tables shall be made in accordance with the following requirements: the top line contains the data name and dimensions; the following lines contain the data itself.
- 11. Formulas, tables and figures shall have their own separate continuous numbering system. If there are no additional (return) references to a specific formula in the text or it is used only once, it shall not be numbered. A table and/or a figure used only once do not require numbering either.
 - 12. Manuscripts and CD/DVD will not be sent back by the editorial board.
- 13. Authors (or an author) of each article after it is published in a journal issue have a right to receive an electronic version of the article in PDF format (Adobe Acrobat editor) from the editorial board.
- 14. When published in the journal, each article is accompanied by a footnote with the copyright symbol © placed before the author's name (authors' names). The article shall also specify the date the article was received by the editorial board.

